UNIVERSITÀ DEGLI STUDI DELL'INSUBRIA

DOTTORATO DI RICERCA IN BIOTECNOLOGIE,

BIOSCIENZE E TECNOLOGIE CHIRURGICHE

Curriculum BIOLOGIA CELLULARE E MOLECOLARE

XXX CICLO

Boring bacteria: a morphological research on bone diagenesis

Docente guida: **Prof. Mario Raspanti**

Tesi di dottorato di:
Petra R. Basso
Matr. 250417

Dip. Biotecnologie e Scienze della Vita - Università degli Studi dell'Insubria
Anno accademico 2016-2017

TABLE OF CONTENTS

ABSTRACT

Post mortem interval (PMI) estimation is a crucial issue in forensic medicine. To date, little is known about factors affecting post-mortem changes in hard tissues and it is still unclear who between exogenous bacteria from the environment and endogenous microbiota is the cause of microscopical alterations observed in human bone after death. Recent research highlighted an important role of endogenous bacteria in the earlier stages of the process. The aim of this study was to probe a potential endogenous model of human bone biodeterioration, based on the action of oral cavity endogenous microorganisms.

A total of seventy-four fragments of human bone samples were incubated with six bacterial strains, isolated from human tartar specimens. In a forty-eight months long prospective study, the onset and development of bone tissue alterations were serially analysed by scanning electron microscope.

The research furnished evidence that endogenous bacteria are able to bore into human dead bone, giving rise to microstructural changes morphologically indistinguishable from those observed in archaeological and forensic bones.

INTRODUCTION

Post Mortem Interval (the time elapsed since a person has died) estimation is a critical step in forensic practice and, as Longato et al. wrote, it is "*a very important, but still unsatisfactorily defined problem*" (Longato et al. 2015).
Qualitative parameters have been traditionally used in thanatocronology to describe the post-mortem changes in corpses, in order to help defining the time of death.
As discussed in detail later, soft tissues are the primary and most well-characterised targets in early post-mortem changes' investigation, but when it comes to long-term estimation, hard tissues become the focus of the analysis along with a loss of qualitative data.

Cadaveric phenomena are divided into:

- postmortal consecutive phenomena (Clark et al. 1997; Sledzik 1998; Puccini 2009,):
    1. algor mortis (as a result of loss of thermogenesis, the corpse temperature changes, until the ambient temperature is matched. Body cooling below 22-24°C is a certain sign of death);
    2. dehydration of cadaver (it is due to percutaneous evaporation. Skin dehydration occurs in a few hours, while ocular signs of dehydration take 12-24 hours to appear);
    3. acidification (it is due to the accumulation of acid metabolites which follows the arrest of organic oxidation processes, in absence of circulation. This process starts soon after death and is ended by putrefaction onset) (Donaldson et al. 2013);
    4. livor mortis (when there is no more circulation, the blood settles in the dependent portion of the body, causing purplish stains called "hypostasis". Livor mortis arises in 30 minutes- 1 hour after death and reaches maximum extension within 12-18 hours. Hypostasis can migrate completely throughout the first 6-8 hours and becomes fixed after 15-20 hours);
    5. rigor mortis (it is due to the fusion of actin and myosin filaments which occurs when oxygen is no longer present, the body's glycogen is depleted and ATP cannot be resynthesized. Body stiffening starts in approximately 3 hours and extends to whole body within 12-24 hours, with an ostensible cranio-caudal progression, as for Nysten's law. 48-72 hours after the onset, the resolution of rigor mortis is completed);
    6. loss of neuromuscular excitability (neuromuscular excitability disappears in 4-8 hours in skeletal muscles and in 2-3 days in smooth muscles).

- destructive transformative phenomena (Rodriguez and Bass 1985, Rodriguez 1997, Rhine and Dawson 1998, Sledzik 1998):
    1. autolysis (demolitive process caused by the rupture of lysosomal membrane);
    2. autodigestion (after death both pancreatic and gastric juices are released, affecting pancreas and stomach first and then the surrounding organs);
    3. putrefaction: decomposition of organic matter by anaerobic and aerobic bacteria, which causes the release of gases that infiltrate the body's tissues and leads to the deterioration of the tissues and organs. Even though a large number of environmental and individual conditions impacts on putrefaction timing (for example: ambient temperature, ventilation and air humidity, clothing, and animal predators as extrinsic conditions, while intrinsic factors include age, constitution, cause of death, the corpse integrity…), nevertheless putrefactive body changes usually follow a standard sequence and the whole putrefactive process can be schematically divided into four phases:
        - chromatic stage: the first external, macroscopic evidence of putrefaction is a greenish skin discoloration, usually in the right iliac fossa, which is typically seen between 18 and 36 hours after death and it is due to the bacterially induced breaking down of haemoglobin into sulfhaemoglobin. The putrefactive bacteria, following the venous system, gradually spread over the whole body, causing the so called “venous marbling”;
        - swelling stage: within 3-6 days after death in summertime or some weeks during winter, bacterial gas formation becomes marked, leading to putrefactive epidermolysis and massive corpse bloating.
        - colliquative stage: it is the progressive disintegration of body tissues and viscera and largely depends on local environmental conditions.
        - skeletonization: it is the ending stage of putrefaction, when ligaments, cartilage and periosteal tags are destroyed. It usually occurs within 3 to 5 years (Mueller 1953).
- special transformative phenomena:
    1. maceration (it is defined as the softening and breaking down of tissues due to prolonged soaking into a liquid);
    2. mummification (in a hot, dry, well aired setting, the corpse dehydrates very quickly, bacterial growth and putrefaction are inhibited and the skin dries to a dark coriaceous appearance. This process takes 2-3 months to one year to get completed and lasts for centuries);
    3. saponification (this process occurs best in an environment that has high levels of moisture and a low temperature, such as in a wet ground or when the cadaver is enclosed in zinc case. It starts soon after death, when enzyme mediated

hydrolysis of the triglycerides produces a mix of saturated and unsaturated fatty acids. Free fatty acids can combine with calcium, sodium and magnesium ions forming soaps. Saponification process usually completes within 6 to 12 months) (Forbes et al. 2004);

4. corification (it takes place in corpses closed in a hermetically sealed zinc or lead coffin: in these conditions, putrefaction is inhibited, the skin shrivels and gets a "tan leather" appearance).

Apart from the peculiar alterations previously mentioned, due to deterioration processes, only hard tissues can be available in the long period. Although these tissues provide useful information regarding sex, ancestry, age at death, cause of death, medical history, nutritional conditions, etc., their usefulness for thanatochronological evaluations is limited. Therefore, an efficient and punctual characterisation of processes in bone diagenesis is highly required to define the post-mortem changes in bones for both endogenous and exogenous factors.

Various techniques have been developed through the decades, most of them aim to apply more objectives parameters and use quantitative techniques and scoring systems, for example:

- radiometric methods: in addition to ^{14}C (which, with its half-life of 5730 years, is of limited help for forensic investigations (Ubelaker et al. 2006; Alkass et al. 2011) but is useful for dating organic materials up to 50000 years ago), over the years a number of papers suggest using a radionuclide with a physical half-life in the same range as the PMI of forensic interest, such as ^{210}Pb (physical half-life of 22.5 years, (Salmon et al. 1999, Schrag et al. 2012, Schrag et al. 2014,Swift 1998)), ^{90}Sr (physical half-life of 29.5 years, (Maclaughlin-Black et al. 1992)), ^{228}Th (physical half-life of 1.92 years (Cook et al. 2014)) and ^{210}Po (physical half-life 138 days, Swift 1998; Cook et al. 2014);
- histological methods. The Oxford Histological Index (OHI), as described by Hedges et al (Hedges et al. 1995), is the standard method to summarize the degree of diagenetic changes in bone: this scoring system assigns values from 0 (when less than 5% of the bone specimen is structurally intact) to 5 (when more than 95% of the bone specimen features is well preserved). In 2012 Hollund et al. developed the General Histological Index, which is analogous to the OHI, but introduces the evaluation of no microbially mediated destruction alterations (Hollund et al. 2012);
- chemoluminescence tests, such as the luminol reaction (Creamer and Buck 2009, Ramsthaler et al. 2009);
- spectroscopical analysis (Nagy et al. 2008; McLauglin and Lednev 2011; Howes et al. 2012; Buckley et al. 2014; Creagh and Cameron 2017);

- analytical methods, based on the evaluation of the chemical characteristics of skeletal remains (for example nitrogen and amino acid content in bone (Knight 1969)). According to a previous research by Schwarcz et al. (Schwarcz, Agur and Jantz, 2010), the citrate content of bone decreases linearly as a function of time with an increase of PMI. As recently confirmed by Wilson et al (Wilson and Christensen 2017), the bone citrate content, which appears to be independent of post-mortem environment, may provide a reliable parameter for PMI estimation;
- imaging techniques, such as mid infrared reflection and attenuate total infrared microscopic imaging (Woess et al. 2017).

To date, as the time elapsed since death increases, PMI evaluation becomes more and more problematic (in the words of Goff: "the longer a body has been deceased, the wider the PMI estimate" (Goff 1993)) and, since still little is known about factors affecting post-mortem changes in hard tissues, it is even harder to define the PMI when we are dealing with skeletal remains.

In fact, even though, historically, the first observation of post-mortem microscopic changes in bone and teeth were made in the second half of the nineteenth century (Wedl 1864, Roux 1887 and Schaffer 1889, 1890, 1894), however, currently there is still no general consent to establish either the initial time or the duration or the speed of post-mortem degenerative changes in hard tissues (Hedges 2002).
As a confirmation, a review of the literature offers controversial data: Wedl reported an alteration of dentin in samples immerse in water after 13-17 days; Marchiafava et al. (Marchiafava, Bonucci and Ascenzi 1974) provided the evidence of tunneling on the 45th day after the burial of fragments of human vertebrae; using backscattered electron imaging, Bell et al. (Bell, Skinner and Jones 1996) demonstrated the presence of microstructural changes on a human tibial fragment 3 months after death; Ascenzi and Silvestrini (1984) observed canaliculi in specimens of bovine metatarsal deposited in water for at least 12 months; Hackett (1981) described microscopical focal destruction in human bone fragments exhumed after one year burial; using microradiography and electron microscopy, Yoshino et al. (1991) identified postmortem changes in human compact bone respectively about 5 years after buried in soil and 4-5 years after immersed in sea.

In some studies, environmental conditions, such as oxygen rate, humidity, temperature, pH, presence of microorganisms, flora and fauna activities (Hedges and Millard 1995, Hedges et al 1995; Hedges 2002; Turner-Walker and Jans 2008), have been pointed out as the main cause of microscopical structural changes in skeletal remains.

This model can be referred as an “exogenous model” of bioerosion, where the hard tissues remain both morphologically and biomolecularly intact till skeletonized, time when they are exposed to biodeterioration due to the above-mentioned environmental factors and to bioerosion due to environment-associated microorganisms (Turner-Walker and Jans 2008; Fernandez-Jalvo et al. 2010; Muller et al. 2011).

While the studies conducted to verify the “exogenous model” of hard tissue bioerosion-biodeterioration reliability have presented conflicting findings (Hackett 1981; Child et al. 1993; Balzer et al. 1997; Jackes et al. 2001), recent researches have hypothesised a correlation between bone microstructural deterioration and endogenous microbes, which act in earlier post-mortem stages (Jans et al. 2004; Guarino et al. 2006; Nielsen-Marsh et al. 2007; Hollund et al. 2012; White and Booth 2014).

This dissertation aims to investigate an experimental endogenous model of human bone biodeterioration, based on the action of oral cavity endogenous microorganisms. This hypothesis comes from the nearly complete equivalence of the morphological pattern of the micro-tunnelling observed in human post-mortem bone samples (both archaeological samples and forensic specimens), in human tartar specimens and in bone tissue samples, collected in proximity of fully osseointegrated dental endoosseous implants removed due to long-term complications.
For this reason, the study here presented develops and discusses experimental protocols for the determination of microbial invasion in human bone and related alterations. The experiments have been carried out in controlled conditions, isolating the effect of each parameter singularly, and omitting non-controllable exogenous and environmental factors.

MATERIALS AND METHODS

Microorganism collection:

The oral cavity microorganisms were collected from the tartar of twelve volunteer donors, chosen completely at random, during routine dental debridement, carried out at a private dentist office in year 2015.
The donors, aged between 25 and 66 years, belonged to both sexes, were not affected by known organic diseases and did not take antibiotics during the month prior to the procedure. Other details are specified in Table 1.
All the donors gave their consent for the use of the collected specimens in the context of this study.

Table 1:

Donor	Donor gender	Donor year of birth	Note
1	female	1990	non-smoker
2	female	1976	non-smoker
3	male	1961	non-smoker
4	female	1950	non-smoker
5	male	1976	smoker
6	male	1981	non-smoker
7	female	1983	non-smoker
8	female	1976	non-smoker
9	female	1958	non-smoker
10	female	1990	non-smoker
11	male	1975	non-smoker
12	male	1973	non-smoker

First of all, to avoid salival contamination, the region of incisors was isolated using cotton rolls and a saliva ejector, then supra-gingival tartar samples were collected from lingual surfaces of mandibular and maxillary incisors (Jin and Yip, 2002), using sterile hand tools, including periodontal scaler and curettes. Immediately after collection, each tartar sample was put into a thioglycollate tube (BDTM Fluid Thioglycollate Medium – FTM), then each tube containing the tartar specimen was brought to the microbiology laboratory, where it was incubated at 37°C for 72 hours.

Every 24 hours subcultures were made on:

- Columbia Blood Agar (AS),
- Chocolate Agar (AC),
- MacConkey Agar II (MC),
- Sabouraud Dextrose Agar (SDA),
- Schaedler KV Agar (KV).

Agar plates were provided by Becton Dickinson Gmbh (Heidelberg, Germany).

The inoculated plates were incubated for 72 hours as follows:

AS and AC	37°C, aerobic atmosphere + CO^2 5%
MC and SDA	37°C, aerobic atmosphere
KV	37°C, anaerobic atmosphere

Every 24 hours each plate was observed in order to evaluate the bacterial growth and colonies (if there were) were reisolated onto a specific growth medium, under appropriate conditions.

MALDI-TOF Mass Spectrometry (MS) bacterial identification:

The isolated colonies were identified by MALDI-TOF Mass Spectrometry (MS, Bruker Daltonics): under laminar flow cabinet, a little amount of each colony was taken, using a sterile toothpick, and was spotted onto a target plate. After air-drying, each spot was overlaid with 1 µl of HCCA matrix solution (Sigma-Aldrich). The isolated bacteria were frozen and stored at −80 °C with 20 % (volume per volume) glycerol for further analysis.
Measurements were performed on a Microflex LTTM (Bruker Daltonics, Bremen, Germany) instrument and data were automatically acquired using FlexControlTM 3.4 software (Bruker Daltonics).
Bacterial test standard (BTS, Bruker Daltonics) was used for mass calibration TM instrument parameter optimization. Spectra were acquired in linear positive mode within a mass range from 2000 to 20,000 m/z (mass-to-charge ratio), according to the manufacturer's settings suggestion, using automated collecting spectra mode. Then, the obtained spectra were analysed by standard pattern-matching algorithm using the MALDI BiotyperTM 3.1 software (Bruker Daltonics), which compared the raw spectra with the reference spectra of the Bruker library (database version 3.3.1, 5627 reference spectra) by using the default settings.

Identification (ID) criteria were used as manufacturer's recommendation: a score ≥ 2.000 indicated species level ID, a score between 1.700 and 1.999 indicated ID to the genus level and a score < 1.700 was interpreted as no ID.
For MainSpectra (MSP) and dendrogram construction, flat-liners and bad quality spectra were removed and additional measurements were carried out to obtain 20 spectra from each isolate/strain. Spectra were then loaded into BiotyperTM 3.1 software (Bruker Daltonics) for MSP creation and dendrogram clustering construction with the default settings (distance measure: correlation; linkage: average; score oriented).

Identification by direct sequencing:

Bacterial DNA was obtained by extraction with the kit QiAmp DNA Blood Mini Kit (Qiagen), starting from pure colonies isolated on Mueller-Hinton Agar.
We performed a PCR assay using a mix with final volume of 50uL, according to manufacturer's recommendation:

Component	Volume per reaction (uL)	Concentration in Master Mix
10X PCR Gold Buffer 25 mM $MgCl_2$	5	1X
dATP, dCTP, dGTP, dTTP 10 mM each	1	200 µM
User-provided Primer 1	1-5	0.2-1.0 µM
User-provided Primer 2	1-5	0.2-1.0 µM
User-provided experimental template	Δ	< 1 µg/reaction *
AmpliTaq Gold	0,25	1.25 Units/reaction
Water	Δ	
Total volume	50	

*Preferably > 10^4 copies of template but < 1 µg DNA/reaction

The primers used were the universal ones which amplified the region of the 16S ribosomal RNA, used as "gold standard" for identification of eubacteria:

Primers ID	Sequence	Product Size (bp)	Reference
16S King Fw	5'-GAGAGTTTGATCCTGGCTCAG	1000 bp	Eden PA et al, 1991
16S King Rv	5'-TACGGCTACCTTGTTACGACTT		

Amplification was carried out with the following thermal cycling conditions: 10 min at 95°C ; 35 cycles of amplification consisting of 30s at 95°C, 30s at 58°C, and 30s at 72°C, with 7min at 72°C for the final extension. DNA fragments were analysed by electrophoresis in a 1,5% agarose gel in 1× TBE (89 mM Tris-borate and 2 mM EDTA, pH 8.3) containing GelRed™ Nucleic Acid Stain (10000x in water, Biotium).
PCR positive products were treated with ExoSAP-IT® (Affymetrix), which occurs with a single-step enzymatic clean-up that eliminates unincorporated primers and dNTPs. At this point is prepared the master mix for sequence reaction, using the BigDye® Terminator Cycle Sequencing Kit (Applied Biosystems, Foster City, California).
Sequencing products were loaded on ABIPrism310 sequencer (Applied Biosystem, Foster City, California). Sequences were compared with those from GenBank (www.ncbi.nlm.nih.gov/blast/).

Bone samples collection:

Small fragments of human bone samples were collected from the cranial vault of thirty-seven donors during neurosurgical procedures (craniectomy) carried out during 2015 and 2016 at the Ospedale di Circolo-Fondazione Macchi in Varese; at least three fragments were collected from each donor. The cranial vault was chosen as a source simply because of its easy accessibility and its uniformity. Each sample consisted of a small, irregularly shaped full-thickness bone fragment, with a major axis of approximately 10-12 mm. All donors were potential candidates for bone flap replacement, and they all gave informed consent to surgery.

Donor's characteristics were (Table 2):

- age between 20 and 65 years old,
- both sexes,
- no known bone or metabolic diseases.

Table 2:

Sample number	**Donor gender**	**Donor year of birth**
1	female	1995
2	male	1967
3	female	1955
4	male	1990
5	male	1963
6	female	1973
7	female	1958
8	female	1965
9	male	1967

10	male	1978
11	female	1966
12	male	1978
13	female	1963
14	male	1977
15	female	1949
16	female	1975
17	male	1977
18	female	1956
19	male	1967
20	female	1952
21	female	1960
22	male	1956
23	male	1963
24	male	1995
25	male	1970
26	female	1973
27	female	1959
28	male	1962
29	male	1956
30	male	1990
31	female	1967
32	male	1959
33	male	1978
34	female	1969
35	male	1967
36	female	1949
37	male	1971

Each bone sample underwent microbiological tests, in order to evaluate its sterility (see below); all the samples enrolled in the study were sterile.

Of the three samples of each donor, one part was prepared and examined by scanning electron microscope (SEM), in order to evaluate its morphology at time zero; the other two parts were brought into contact with the bacteria isolated from the plaque. 100 µl of 0.5 McFarland solution of each bacterial culture was placed into a tube containing one bone sample and 10 ml of thioglycollate and incubated at 30 °C and at 37 °C, and the specimens were analysed at different time intervals by scanning electron microscopy in order to study the possible occurrence of diagenetic alterations.

Sterility test protocol (Aho et al. 1998; CDC 2002; CDC 2003; Vastel et al. 1999; Von Versen 1992):

After incubation, every day the vials were observed to evaluate the presence of macroscopic turbidity. Whenever the medium seemed to be turbid or when flocculation occurred, the procedure was as follows:

1. vortex for ten seconds the tube containing the culture broth suspected of positivity;
2. open the tube, under laminar flow cabinet;
3. prepare a slide from the broth (Gram staining);
4. under laminar flow cabinet, take a little amount of broth from each tube containing turbid medium, using an inoculating sterile loop (size 10 µl);
5. under laminar flow cabinet, make a subculture, using an inoculating sterile loop (size 10 µl) to inoculate a third of the surface of the plate of the following growth mediums, then streaking the plate to isolate a pure culture:
   - for fungi: inoculate a plate of Sabouraud dextrose agar, then incubate at 30° C in aerobic atmosphere or at room temperature for 7 days;
   - for anaerobic bacteria: inoculate a plate of Schaedler agar, then incubate at 35° C in anaerobic atmosphere for 7 days;
   - for aerobic bacteria:
   a) inoculate a blood agar plate, then incubate at 35° C in aerobic atmosphere for 72 hours,
   b) inoculate a chocolate agar plate, then incubate in a 5% CO^2 atmosphere at 35° for 72 hours.
6. Store the tubes at room temperature until the end of culturing examination.

Bone samples experimental bacterial inoculation:

Bacterial species isolated from tartar (*Lachnoanaerobaculum orale*, *Actinomyces odontolyticus*, *Streptococcus constellatus*, *Lactobacillus paracasei*, *Lactobacillus delbrueckii* and *Actinomyces turicensis*) and previously frozen and stored at −80 °C with 20% (volume per volume) glycerol were processed as follows: after about 10 minutes at room temperature, bacteria have been recovered from the glycerol stock, using a 10 µl inoculating loop to scrape some of the frozen material from the top, and seeded to Chocolate Agar. Then the plates were incubated at 37° C in atmosphere enriched with 10% CO^2, except for the *Lachnoanaerobaculum orale* plate, which was incubated at 37 °C in anaerobic conditions.

After 48 hours, the growth colonies were identified using MALDI-TOF MS (for a detailed description refer to the procedure above-mentioned)
A 0.5 McFarland solution (Approximate Bacterial Suspension / mL = 1.5 x 10^8) of each bacterium was prepared. A fresh, pure bacterial culture was diluted with a suitable broth, and the test suspension was checked using a spectrophotometer.
Bone samples were transferred in sterile condition to culture tubes containing 8 ml of Thioglycollate medium. Within 15 minutes after adjusting the turbidity of the inoculum suspension, 100 µl of the prepared bacterial solution were added to each tube. After gentle agitation, the tubes were incubated at room temperature. The samples were daily monitored for bacterial growth.
After 5 days, the bacterial strains were prepared, once again, from frozen specimens. At the same time, 100 µl of broth were sampled from each tube (which holds one bone fragment and the bacteria) to check the bacterial vitality (viability control). These samples were seeded on Chocolate Agar and incubated at adequate conditions. Colonies were then analysed to verify the absence of specimen contamination as well as to confirm the presence of the initial bacterial strains with MALDI-TOF instrument (Bruker, Germany).
After 2 days and verified the vitality of all the bacteria, bone specimens were transferred in new sterile tubes, filled with a compound of 8 ml of Thioglycollate medium and a new freshly prepared bacterial suspension (100 µl of 0.5 McFarland solution as previously described).
The whole procedure had been repeated weekly for 10 months.

SEM analysis:

The specimens were fixed in 1% glutaraldehyde plus 1% paraformaldehyde in 0.1 M cacodylate buffer for 12 hours at room temperature, then washed with fresh buffer and dehydrated in graded ethanol and hexamethyldisilazane (EMS, Hatfield, PA).
All specimens were then mounted on appropriate stubs with conductive glue, gold coated with an Emitech K550 sputter-coater (Quorum Emitech, Ashford, UK) and observed with a FEI XL-30 FEG high resolution Scanning Electron Microscope (FEI, Eindhoven, The Netherland) operated in secondary electron imaging (SE). Pictures were directly obtained in digital format as 1424x968, 8bpp TIFF grayscale files.

Results

Six bacterial species were isolated and identified from tartar samples using MALDI-TOF MS:

- *Actinomyces odontolyticus* (score ≥ 2.000);
- *Actinomyces turicensis* (score between 1.700 and 1.999);
- *Lactobacillus delbrueckii* (score ≥ 2.000);
- *Lactobacillus paracasei* (score ≥ 2.000);
- *Lachnoanaerobaculum orale* (score ≥ 2.000);
- *Streptococcus constellatus* (score ≥ 2.000).

As *Actinomyces spp* and *Lachnoanaerobaculum orale* are rare in human infection, 16S rRNA gene sequencing was performed to confirm the identification.

- *Actinomyces odontolyticus* (Fig. 1): Microaerobic, Gram-positive, non spore-forming cocco-bacillus. Optimum growth at 37°C. Catalase negative. Actinomyces are significatively represented in dental plaque of healthy individuals but they are also known to play a role in several dental and oral infections (for example caries, endodontic infections and dental implant- associated infections).

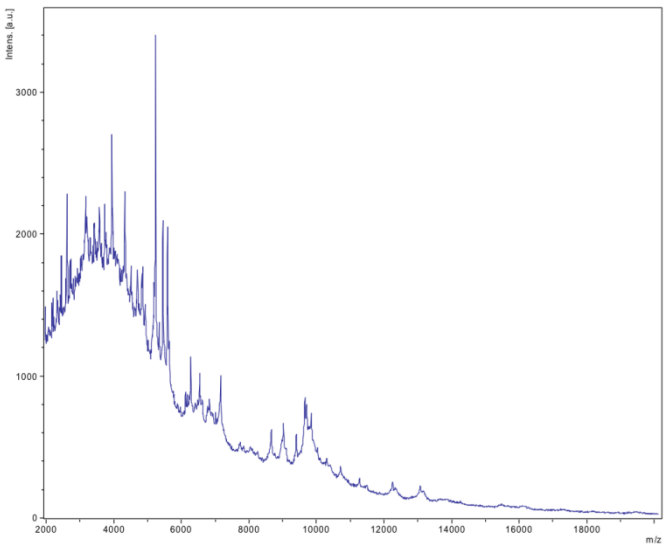

Fig. 1. MALDI-TOF-MS spectrum obtained from the analysis of *Actinomyces odontolyticus.*

- *Actinomyces turicensis* (Fig. 2): Microaerobic, Gram-positive, non spore-forming cocco-bacillus. Optimum growth at 37°C. Catalase negative. Actinomycetes are significatively

represented in dental plaque of healthy individuals but they are also known to play a role in several dental and oral infections (for example caries, endodontic infections and dental implant- associated infections).

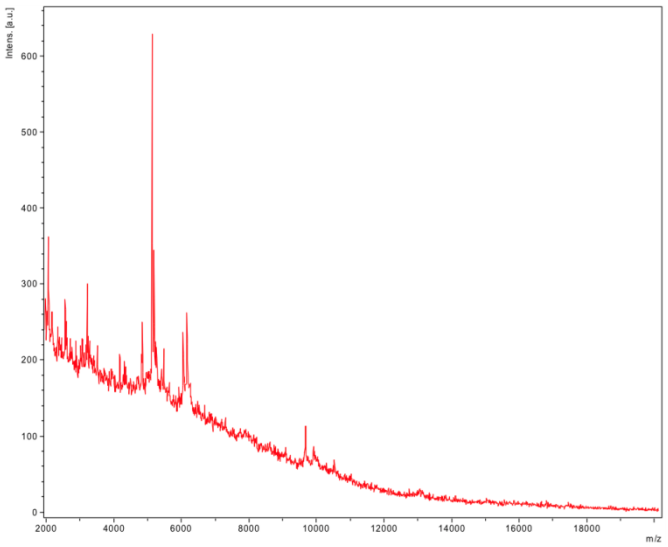

Fig. 2. MALDI-TOF-MS spectrum obtained from the analysis of *Actinomyces turicensis*.

- *Lactobacillus delbrueckii* (Fig. 3): Microaerobic, Gram-positive, non spore-forming bacillus. Optimum growth at 37°C. Produces mainly lactic acid from glucose fermentation. In advanced dental caries, lactobacilli are commonly considered as a secondary colonizer, but evidence exists of their role in exacerbate preexisting lesions.

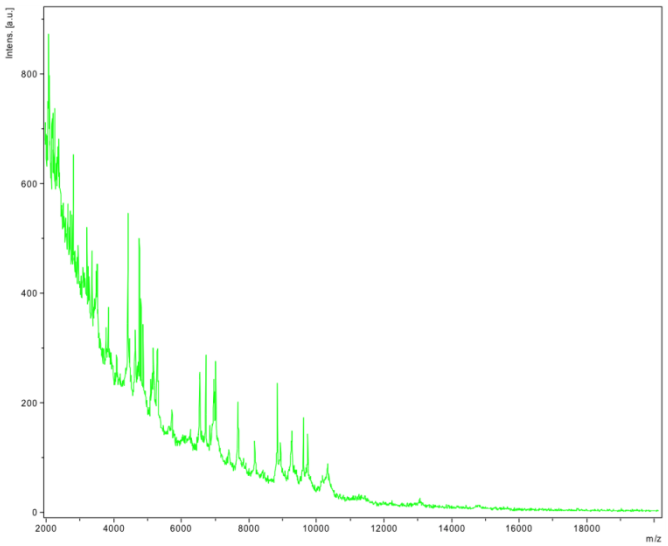

Fig. 3. MALDI-TOF-MS spectrum obtained from the analysis of *Lactobacillus delbrueckii*.

- *Lactobacillus paracasei* (Fig. 4): Microaerobic, Gram-positive, non spore-forming bacillus. Optimum growth at 37°C. Produces mainly lactic acid from glucose fermentation. In advanced dental caries, lactobacilli are commonly considered as a secondary colonizer, but evidence exists of their role in exacerbate preexisting lesions.

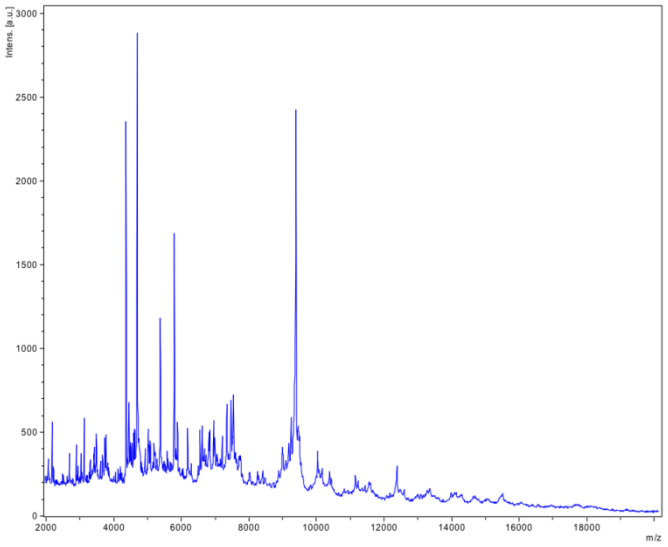

Fig. 4. MALDI-TOF-MS spectrum obtained from the analysis of *Lactobacillus paracasei*.

- *Lachnoanaerobaculum orale* (Fig. 5): Obligately anaerobic, Gram-positive, spore-forming bacillus. Optimum growth at 37°C. Colonies are non-haemolytic.

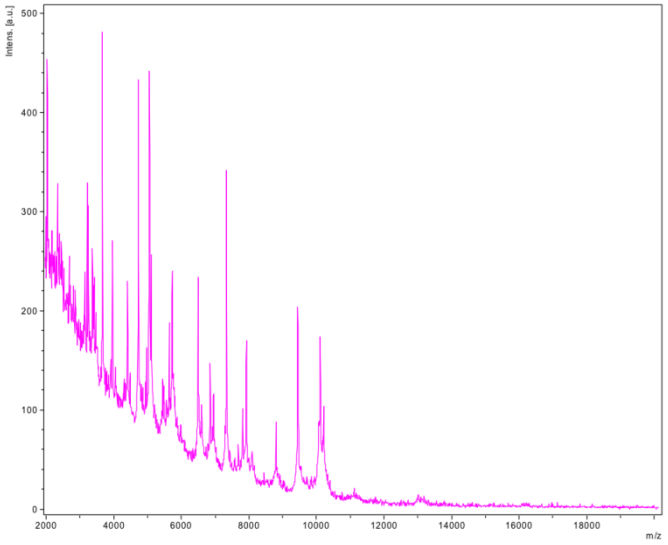

Fig. 5. MALDI-TOF-MS spectrum obtained from the analysis of *Lachnoanaerobaculum orale*.

- *Streptococcus constellatus* (Fig. 6): Facultative anaerobic, Gram-positive coccus. Optimum growth at 37°C. Catalase negative. It is commonly isolated from the respiratory tract and it is a well known commensal of the oropharyngeal, urogenital and gastrointestinal microbiota.

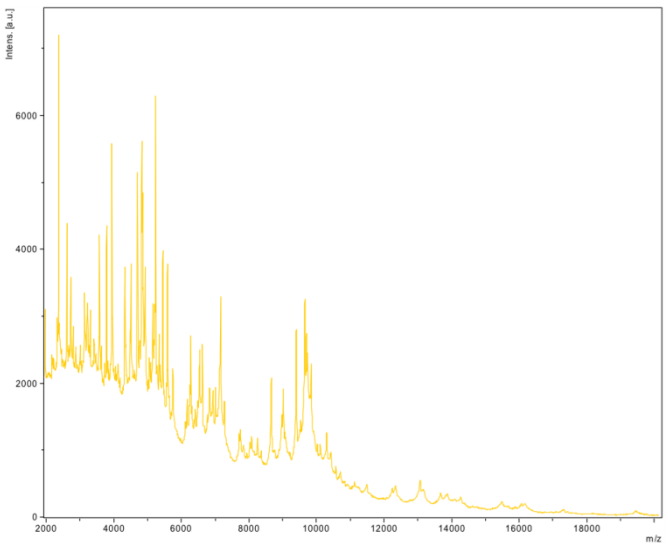

Fig. 6. MALDI-TOF-MS spectrum obtained from the analysis of *Streptococcus constellatus*.

Bone samples:

Control samples (time zero)

No bone alteration was observed in any of the untreated samples during the observations carried out in order to evaluate bone morphology at time zero (Fig.7, Fig. 8, Fig. 9).

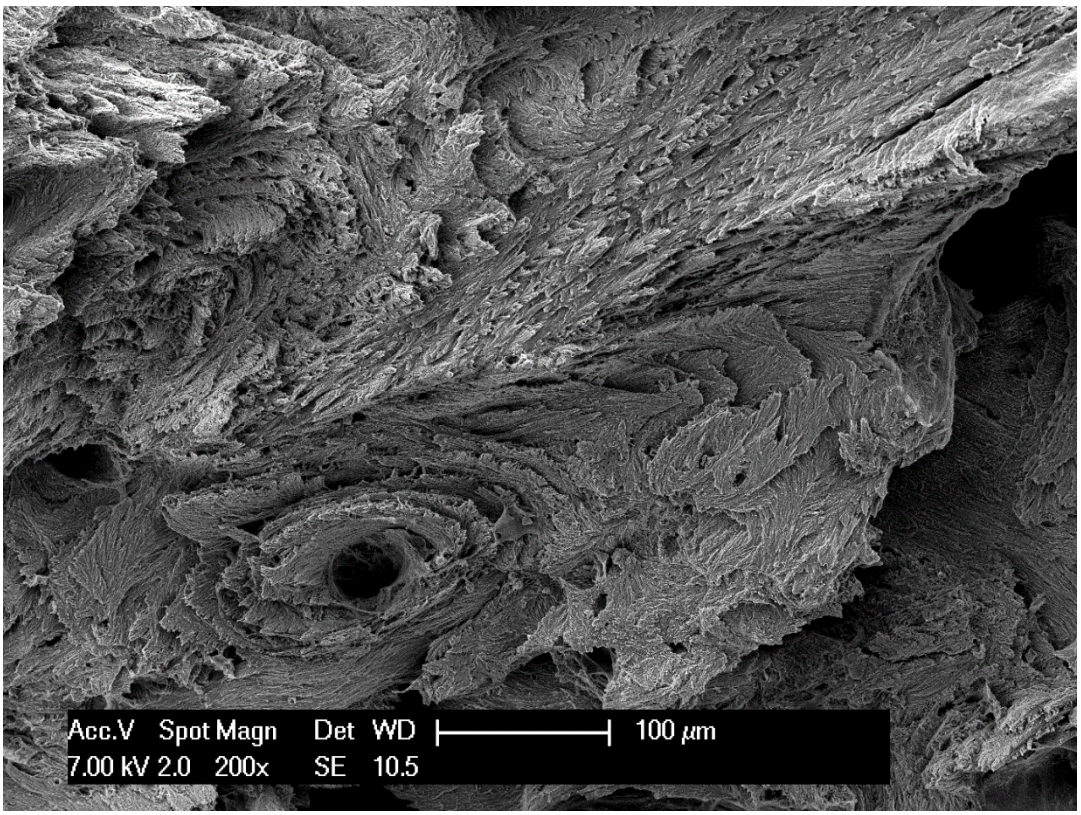

Fig. 7. Scanning electron micrograph of the obliquely fractured human cranial vault bone sample, (control sample, at time zero) showing several bone spicules, a lamellar pattern around the vascular canals.

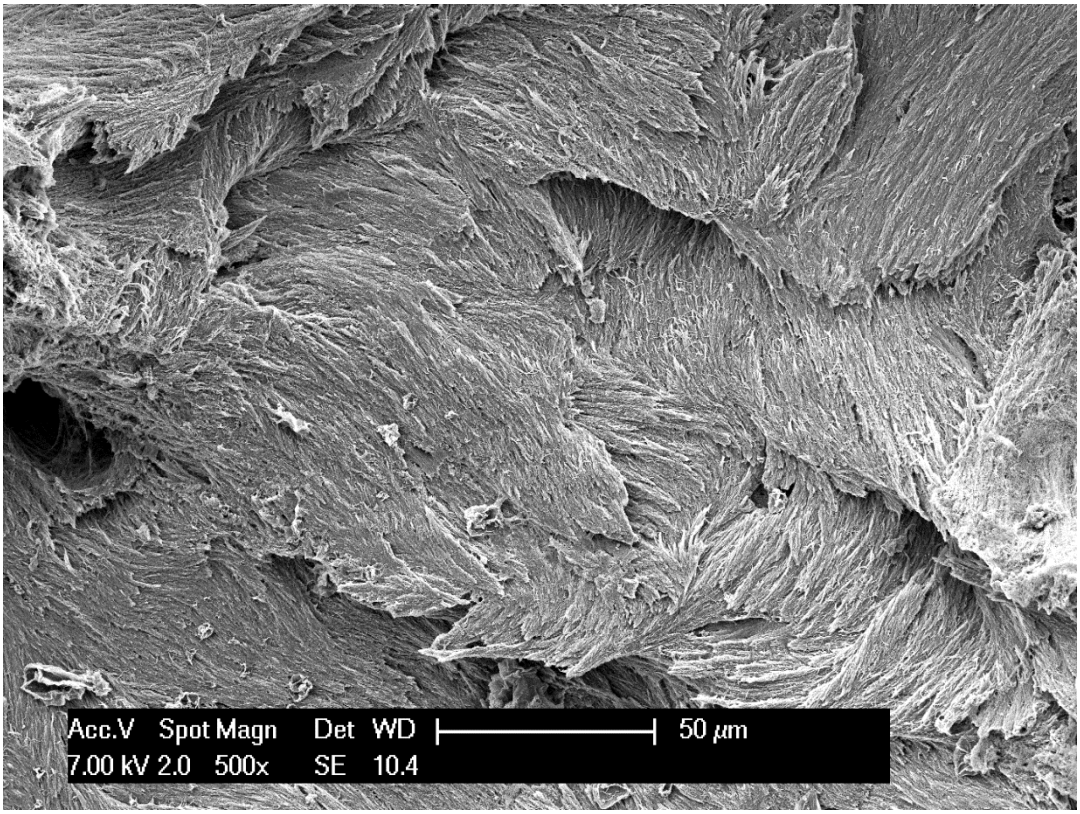

Fig. 8. Scanning electron micrograph of the obliquely fractured human cranial vault bone sample (control sample, at time zero): no morphological alterations are shown and the plywood-like structure is well recognizable.

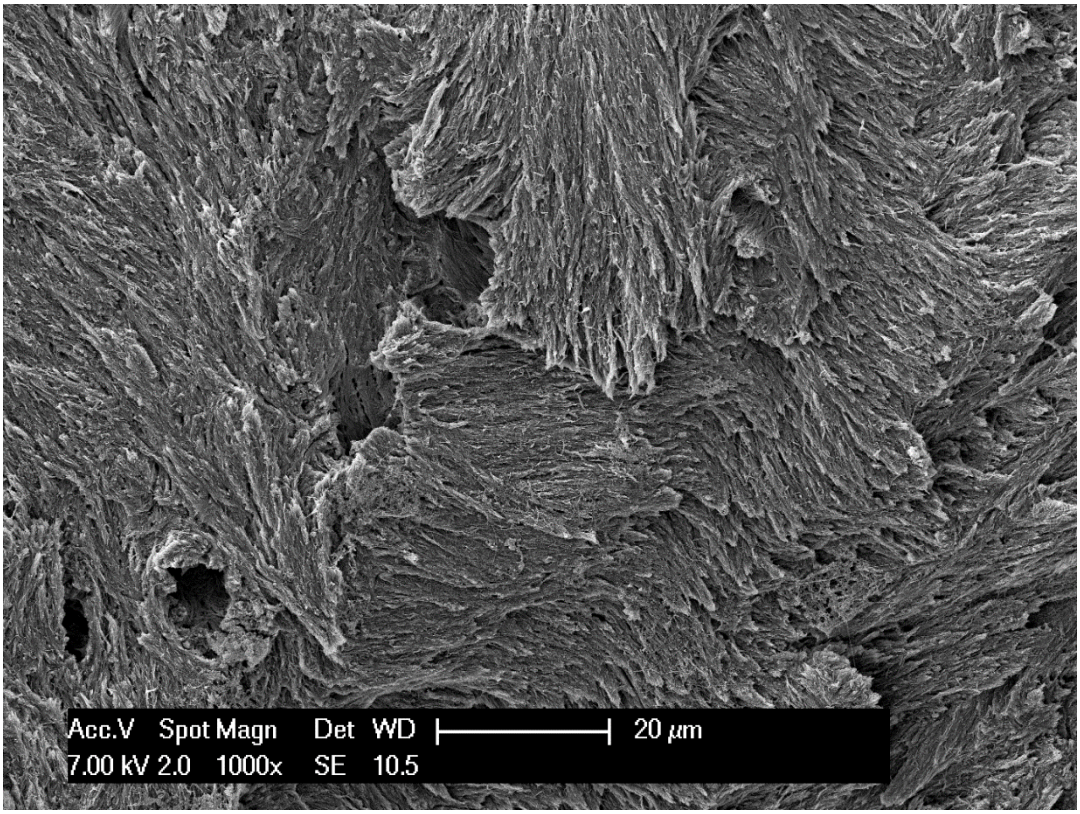

Fig. 9. Scanning electron micrograph of the obliquely fractured human cranial vault bone sample (control sample, at time zero): the lamellar bone structure is well preserved and calcified collagen fibrils are clearly visible.

Interval 1 (one week-long incubation period):

In the observations carried out after one week of bacterial incubation, the bone tissue morphology appeared to be generally preserved, whilst a minor, ubiquitous bone demineralization could be observed at relatively low magnification (Fig. 10). Higher magnification images clearly revealed the lamellar bone structure, as an effect of the initial demineralization (Fig. 11), and several bacteria firmly attached to the specimen surface (Fig. 12).

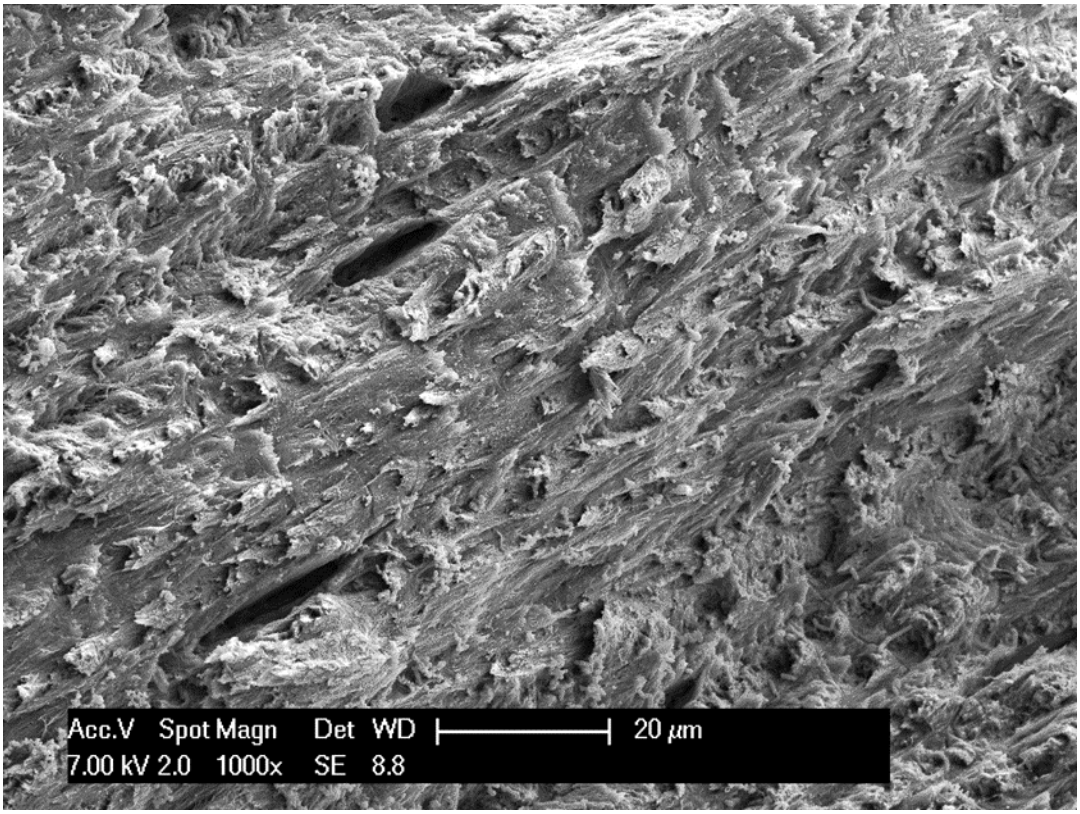

Fig. 10. Scanning electron micrograph of the obliquely fractured human cranial vault bone sample, after a week of bacterial incubation, showing initial signs of demineralization. Three empty osteocytic lacunae and some bacterial clusters are recognizable.

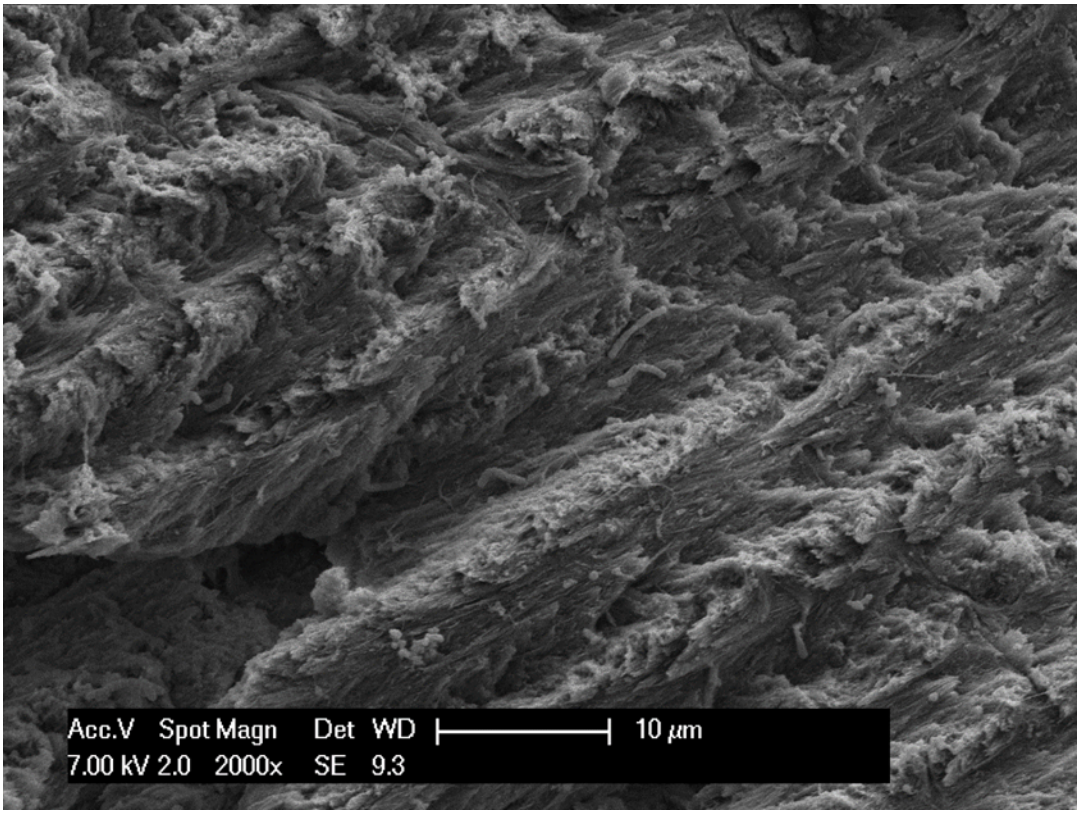

Fig. 11. Higher magnification detail of Fig. 10. Interlamellar lines have been evidenced by the demineralization and a number of differently shaped bacteria is shown.

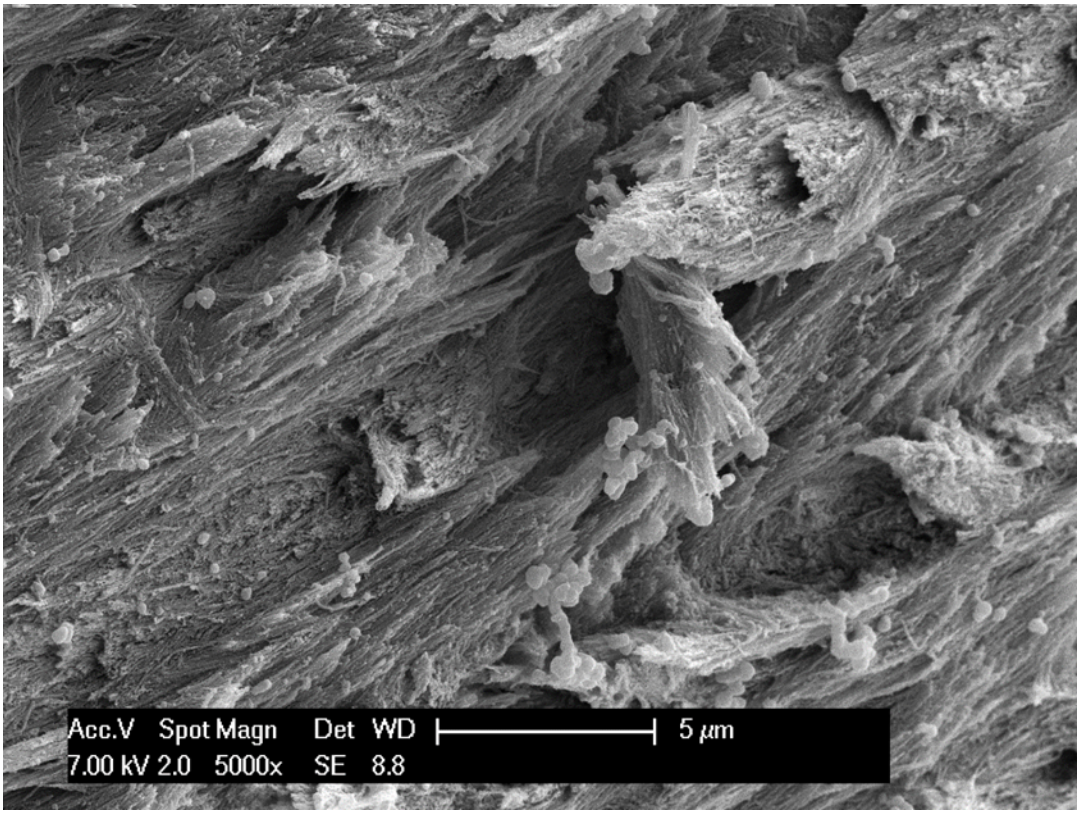

Fig. 12. Scanning electron micrograph of the fracture surface of human cranial vault bone sample, after one week of bacterial incubation: because of the demineralization process, the collagen fibrils are clearly visible. Several bone spicules and some bacterial clusters are also shown.

Interval 2 (two week-long incubation period):

The observations carried out after two weeks of bacterial incubation revealed that the inorganic component of the bone samples was significantly reduced (Fig. 13). The bone tissue was morphologically recognizable and generally well preserved, while the superficial collagen fibrils were clearer than previously observed (Fig. 14-16).

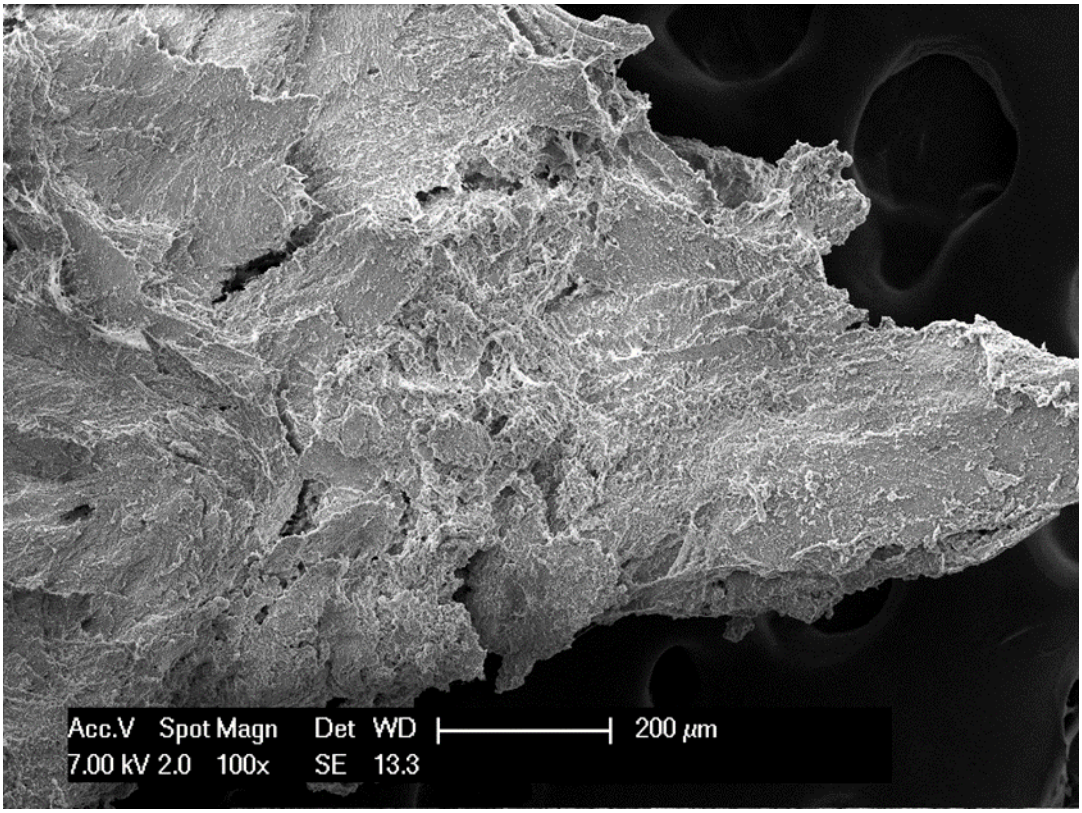

Fig. 13. Scanning electron micrograph of the fracture surface of human cranial vault bone sample, after two weeks of bacterial incubation. Even at low magnification, clear signs of demineralization are easily observed.

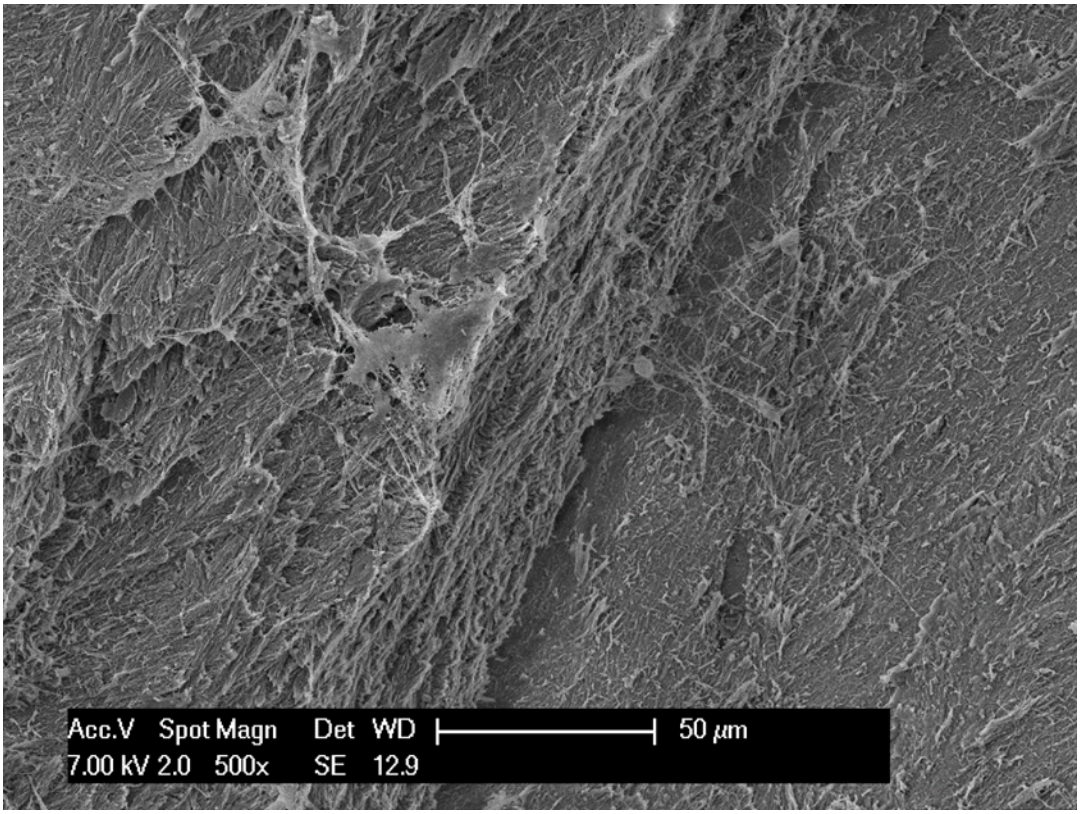

Fig. 14. Scanning electron micrograph of human cranial vault bone sample, after two weeks of bacterial incubation. Collagen fibrils on the bone surface are exposed, indicating an increasing demineralization process.

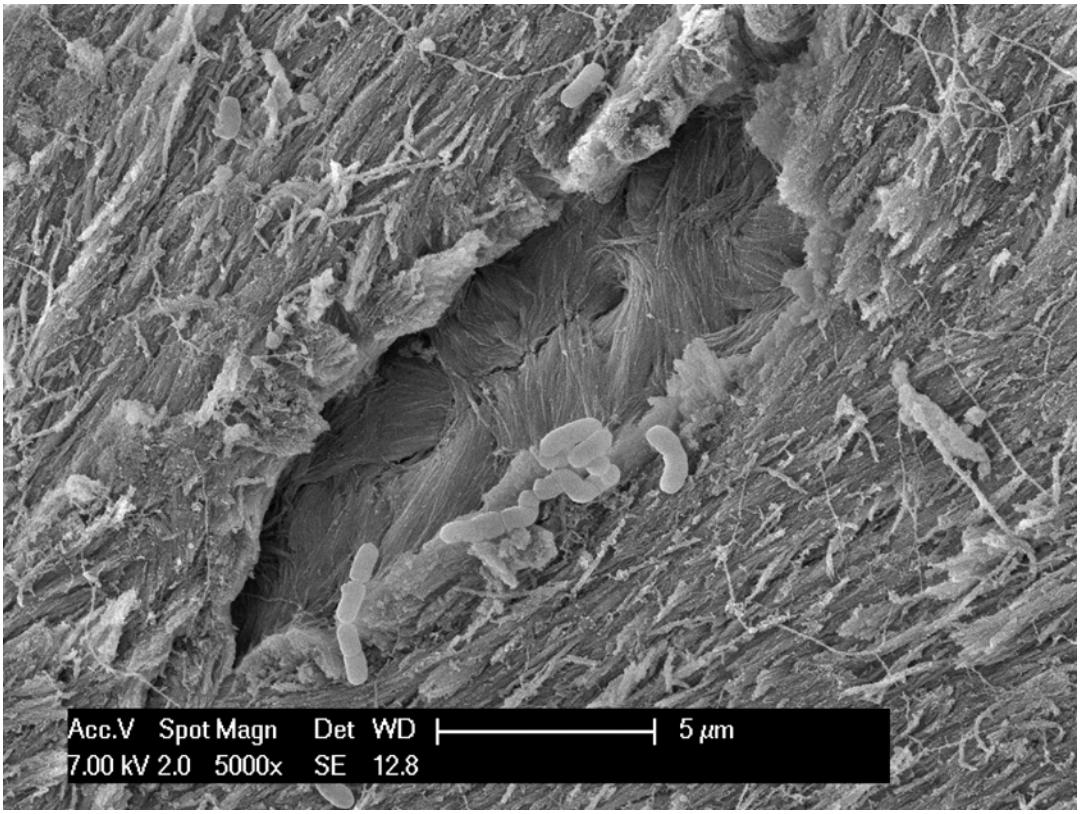

Fig. 15. Scanning electron micrograph of human cranial vault bone sample, after two weeks of bacterial incubation. As expected, within the osteocytic lacuna the collagen fibrils are calcified but visible; collagen fibrils are evident also in perilacunar tissue, suggesting bone demineralization. Some bacilli are also shown.

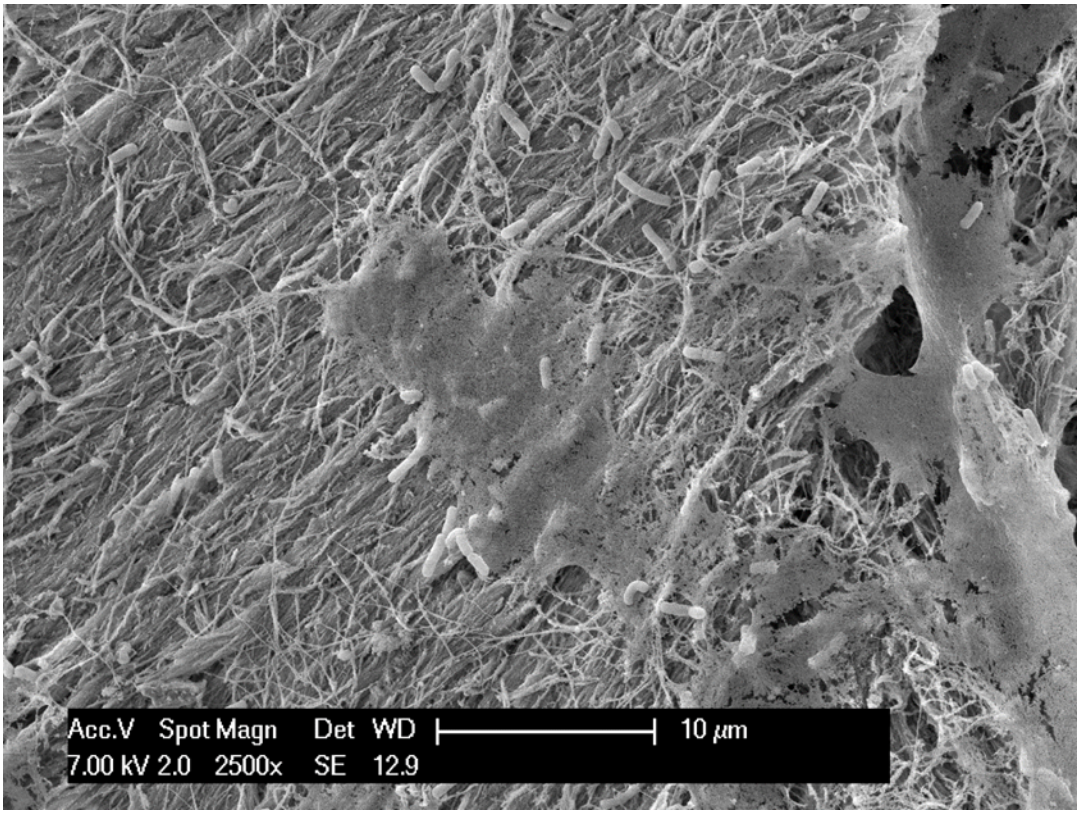

Fig. 16. Scanning electron micrograph of human cranial vault bone sample, after two weeks of bacterial incubation. As a result of the demineralization process, collagen fibrils on the bone surface are exposed and clearly visible. The remnant of an osteocyte and some bacteria, tightly adhered to the specimen surface, are also shown.

Interval 3 (four week-long incubation period):

The observations carried out after four weeks of bacterial incubation showed a further progression of the bone demineralization process, which was homogeneously spread, with no preferential areas of build-up. The bone tissue morphology still appeared to be generally well preserved, while the reduction of the bone mineral content made the lamellar structure clearly apparent, even at low magnification (Fig. 17-20). To this point, no evidence of bone remodelling emerged.

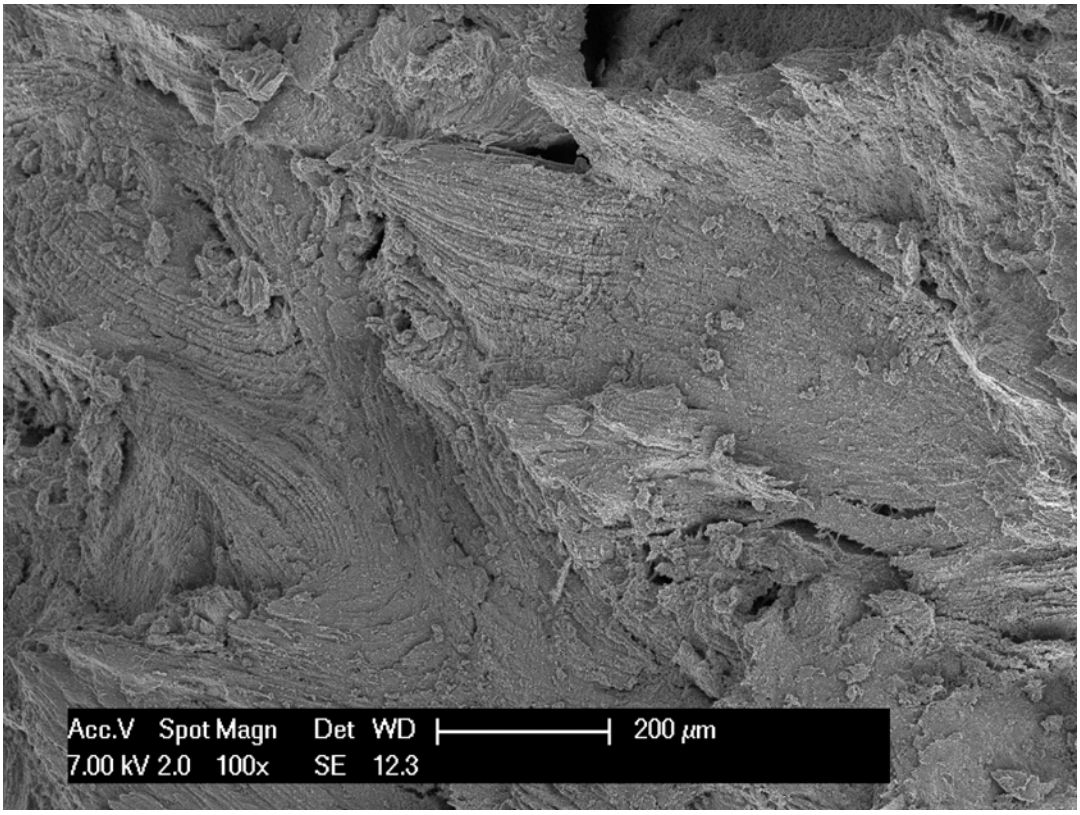

Fig. 17. Scanning electron micrograph of the obliquely fractured surface of human cranial vault bone sample, after four weeks of bacterial incubation. Even at a low magnification, clear signs of a widespread, increasing demineralization are easily observed. The lamellar structure is well preserved. No evidence of bone remodelling is observed.

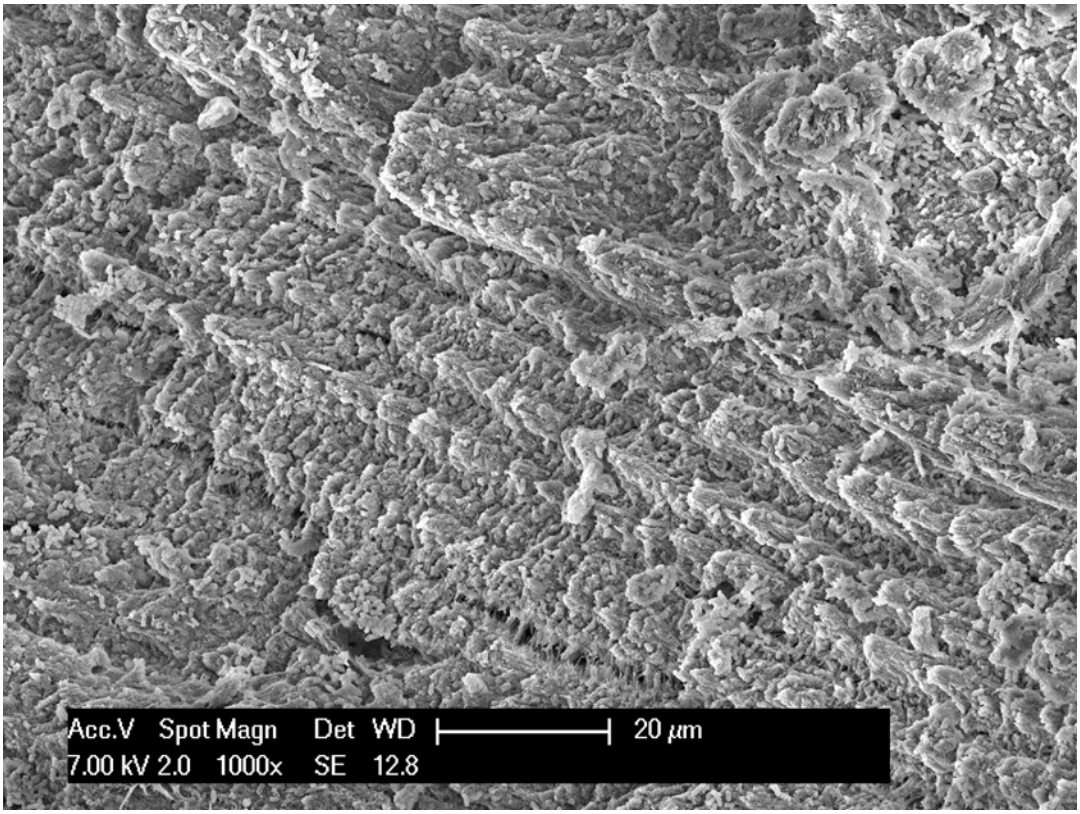

Fig. 18. Scanning electron micrograph of the obliquely fractured surface of human cranial vault bone sample, after four weeks of bacterial incubation. Higher magnification highlights the distinctive lamellar pattern of a Haversian system.

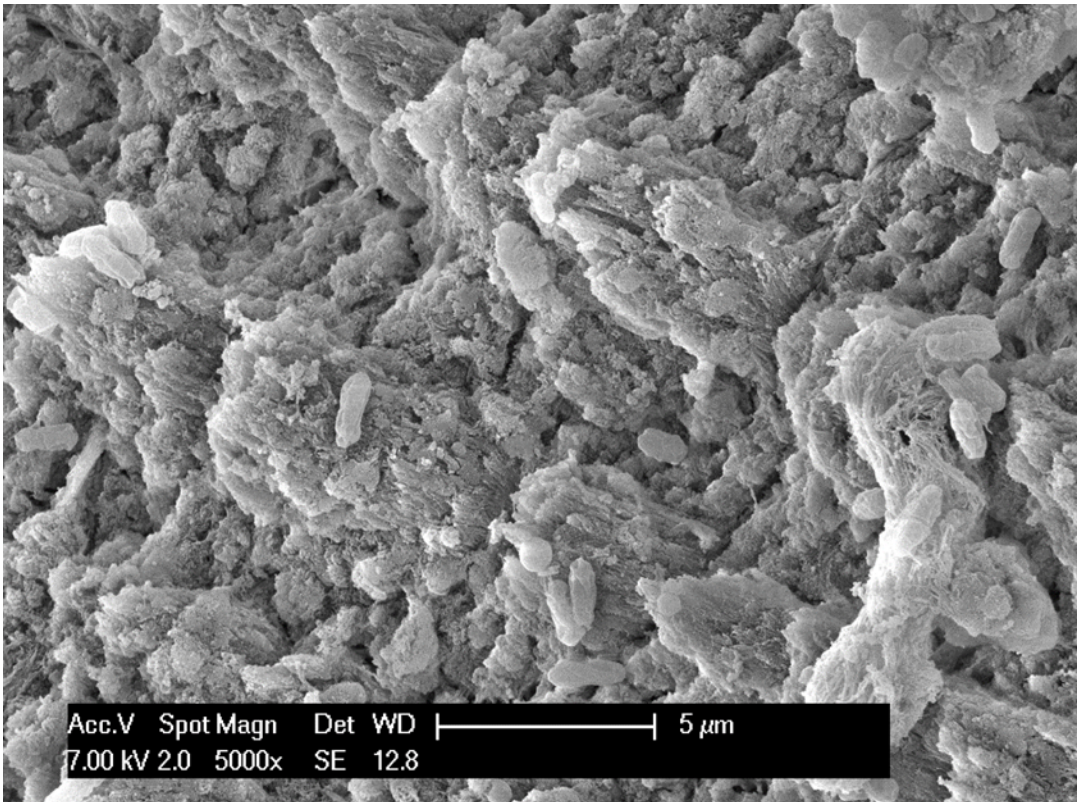

Fig. 19. Higher magnification detail of Fig. 18. Collagen bundles and some bacteria are clearly visible.

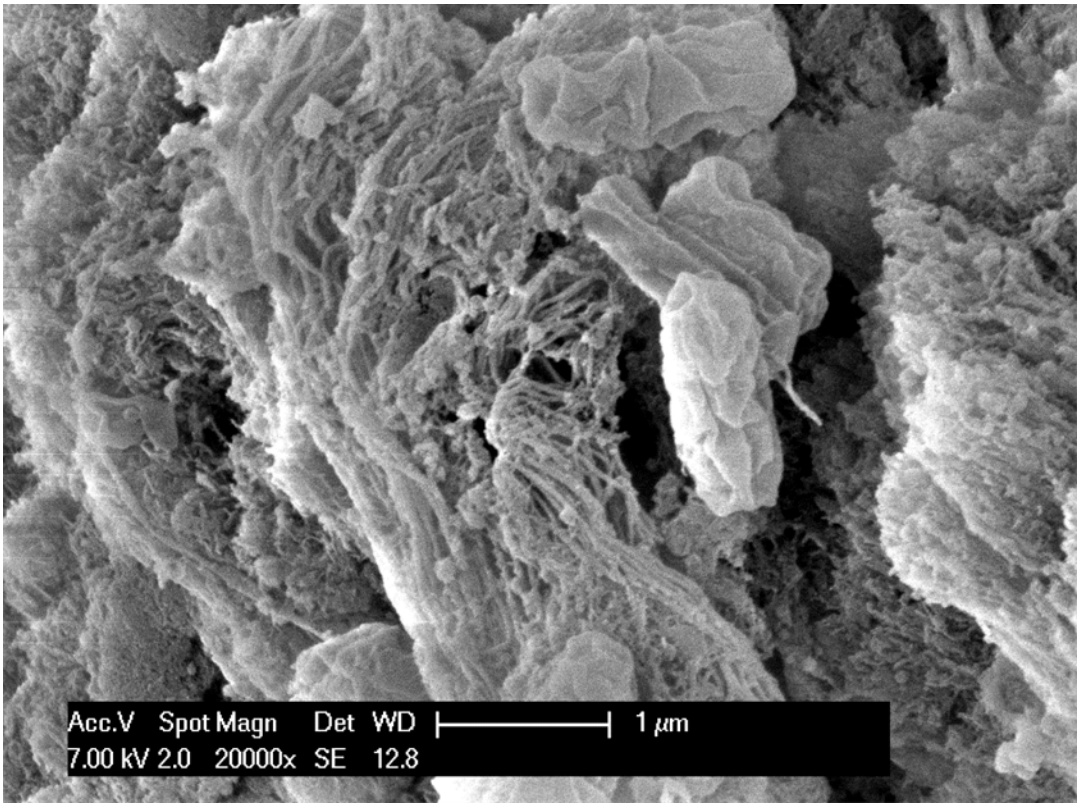

Fig. 20. Higher magnification detail of Fig. 19. Collagen fibrils are clearly visible. Some bacteria with signs of dehydration are also shown.

Interval 4 (5 to 20 week-long incubation period):

The examinations carried out during the interval from five to twenty weeks of bacterial incubation, in addition to a more pronounced demineralization, showed a progressive, substantial morphological alteration of large areas of the bone tissue: while vascular canals remained virtually intact at the ultrastructural level, the lamellate bone structure was still well recognisable only in some areas and large cribriform cavities, not attributable to any physiological human bone structure, appeared on the fragments (Fig. 21-26).

The collagen component seemed not to be affected by any destructive alteration (Fig. 24, 25).

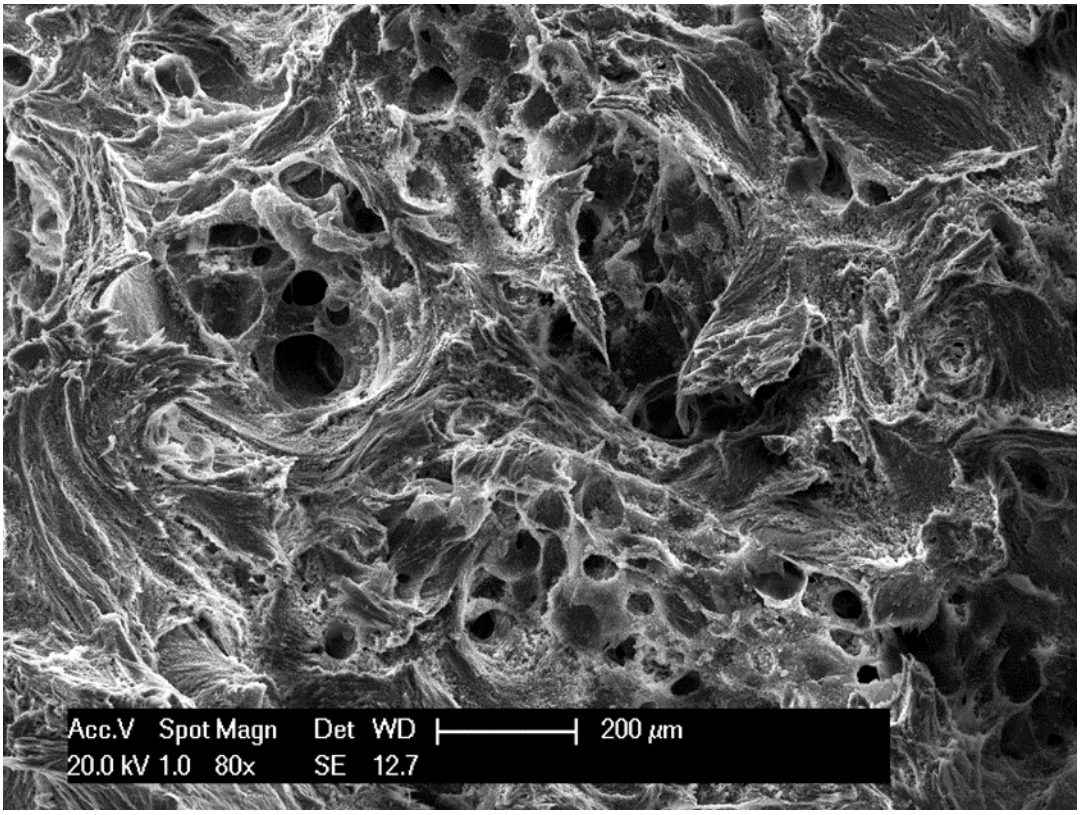

Fig. 21. Scanning electron micrograph of human cranial vault bone sample, after twenty weeks of bacterial incubation, showing severe bone remodelling: a great number of cribriform cavities can be observed. Clear signs of demineralization are observed.

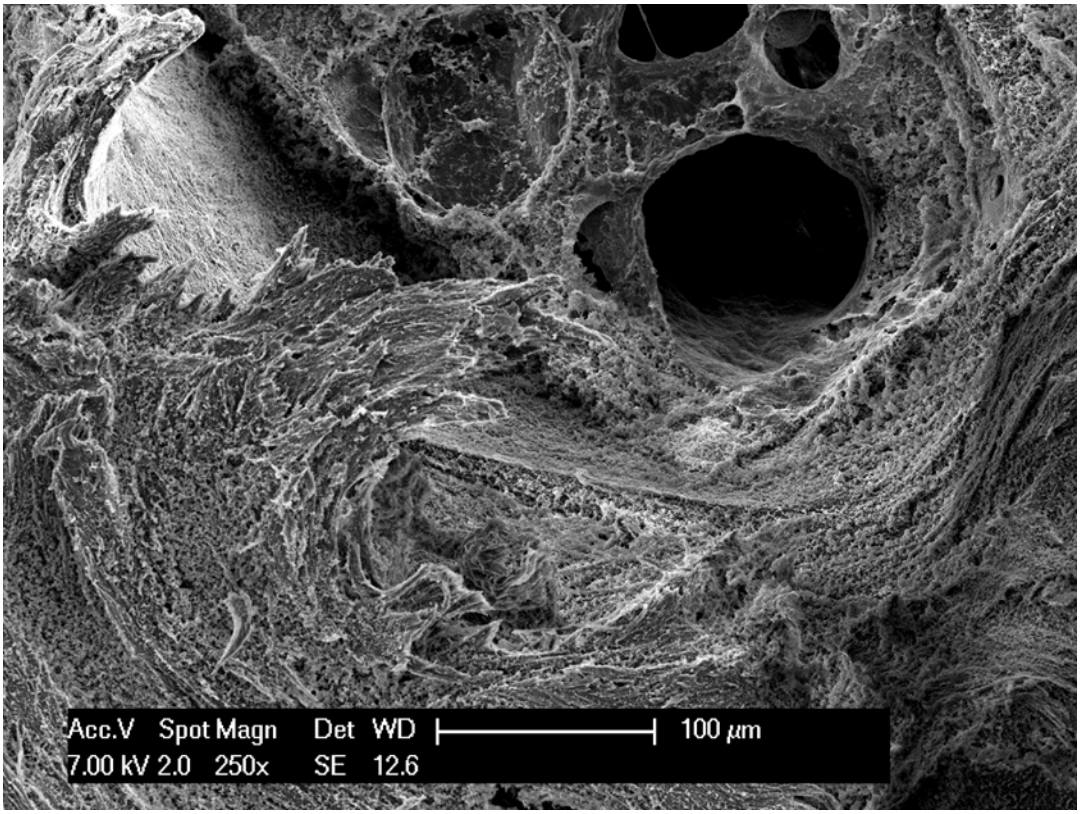

Fig. 22. Higher magnification detail of Fig. 21, showing a neoformed cavity, as a part of a substantial alteration of the bone tissue morphology.

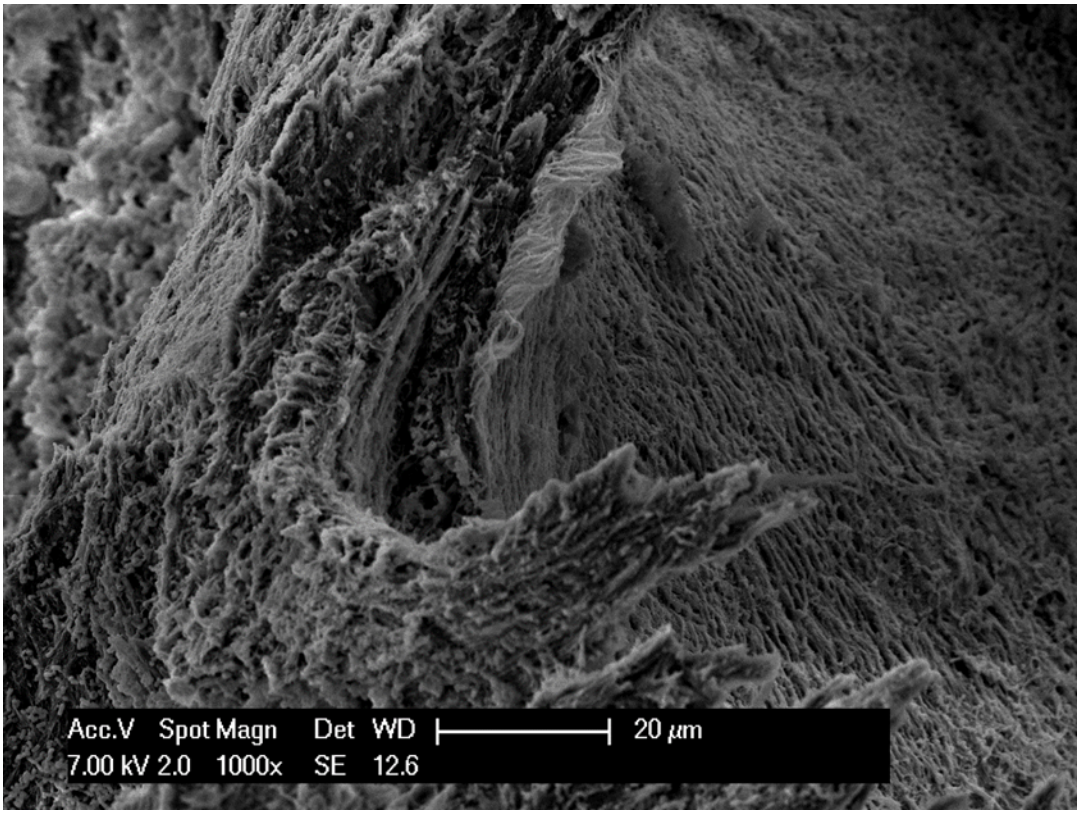

Fig. 23. Higher magnification detail of Fig. 22, highlighting the increasing demineralization process.

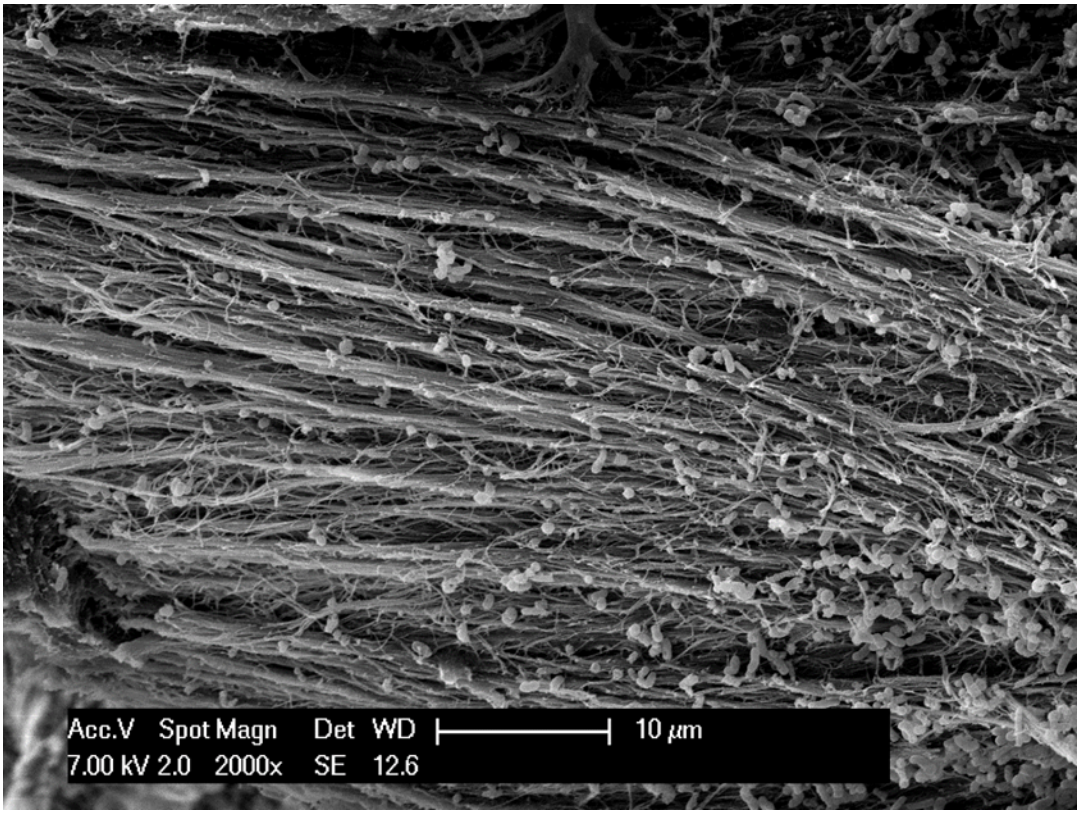

Fig. 24. Scanning electron micrograph of human cranial vault bone sample, after twenty weeks of bacterial incubation. As a result of the demineralization process, collagen bundles on the bone surface are exposed and clearly visible. Several bacteria are also shown.

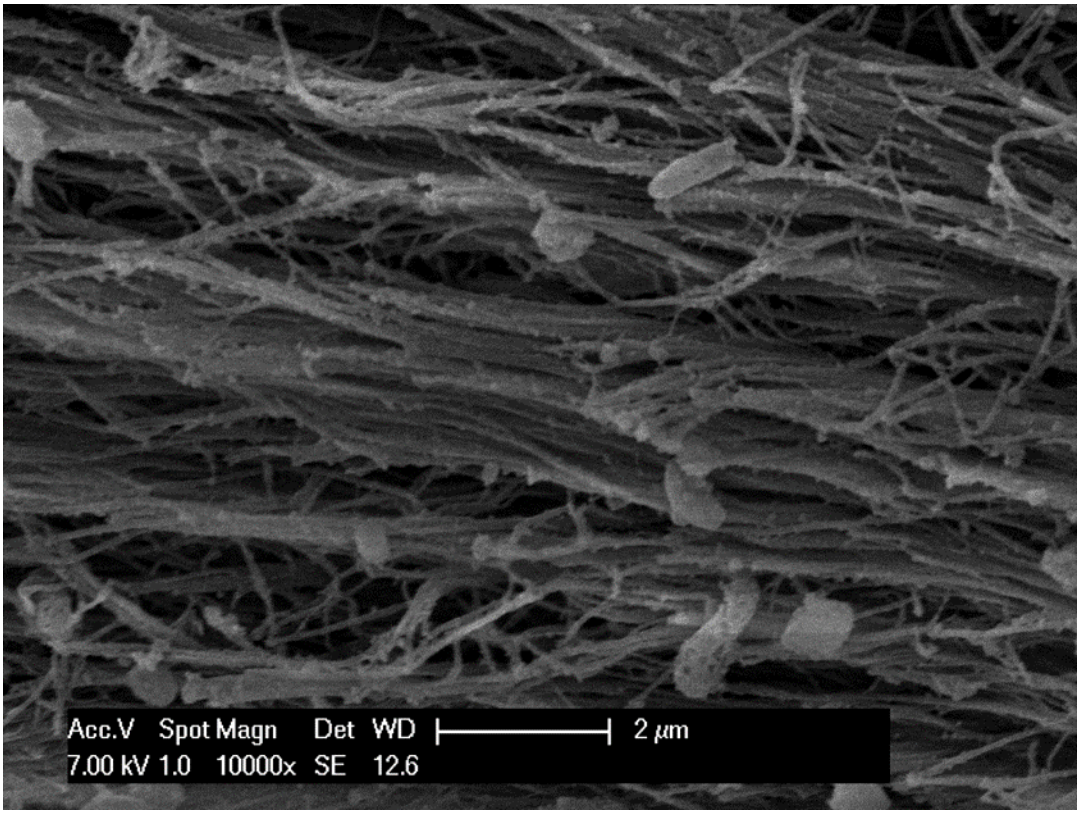

Fig. 25. Higher magnification detail of Fig. 24, showing bacteria located not only on the surface but also between the collagen fibrils.

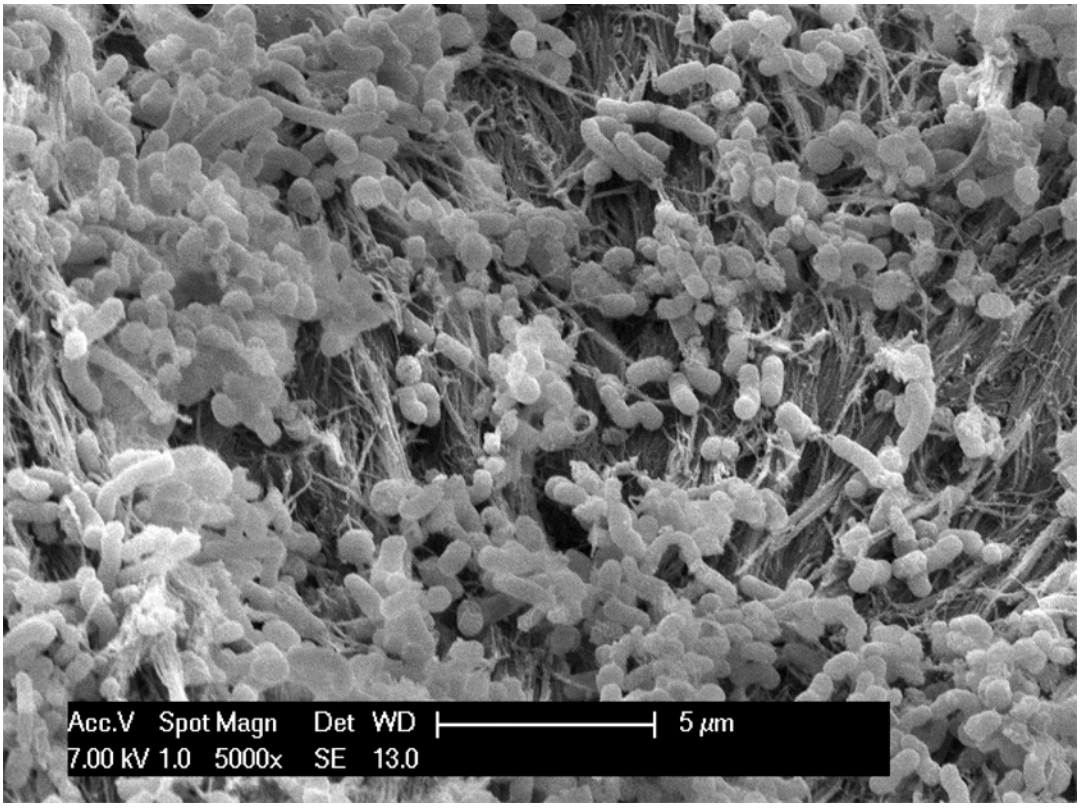

Fig. 26. Scanning electron micrograph of human cranial vault bone sample, after twenty weeks of bacterial incubation. A great number of differently shaped bacteria and some collagen fibrils are shown.

Interval 5 (21 to 38 week-long incubation period):

The examinations carried out during the interval from twenty-one to thirty-eight weeks of bacterial incubation revealed a further increase of the bone demineralization process on the whole sample surface, with no evidence of saving areas or preferential areas of build-up (Fig. 27, 28, 29). Although the vascular canal structure remained generally unaltered, the residual bone tissue presented an increase in morphological changes: areas of well-preserved native lamellar structure progressively decreased and newly- formed tubular structures appeared (Fig. 30, 31). These tunnels had an average diameter of about 50 microns, always run parallel to one another, apparently did not split or merge into each other, and their spatial organization seemed to respect the vascular canals, avoiding any contact with them. Moreover, rare tubular structures with a smaller diameter (ranging from 5 to 10 microns in diameter) and a spatial organization pattern similar to the above-mentioned structure have been observed (Fig. 27). Both types of tubular structure, those with larger diameter and those with smaller diameter, were located into the mesosteal area, without touching the outer or the inner circumferential lamellae at any point.

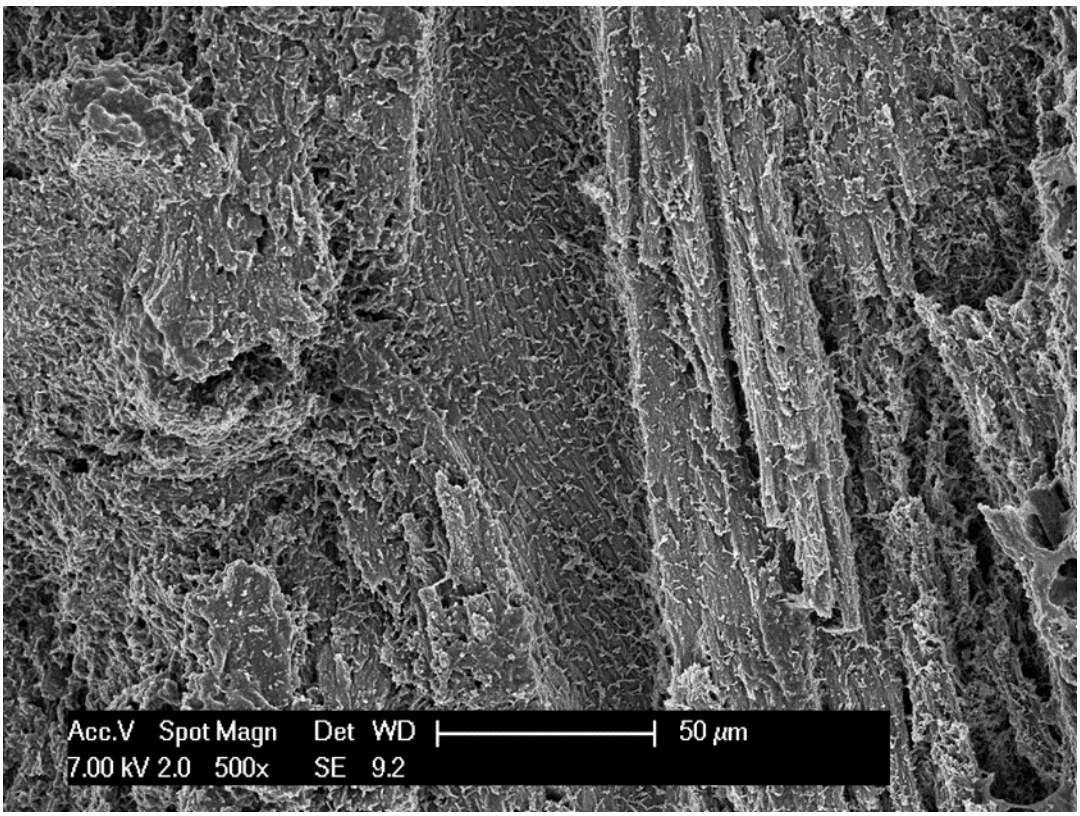

Fig. 27. Scanning electron micrograph of human cranial vault bone sample, after thirty- eight weeks of bacterial incubation. In the context of a severe, widespread demineralization, some tubular structures, with an average diameter of 10 microns, running parallel to one another and to a vascular canal are observed. The vascular canal structure is well-preserved.

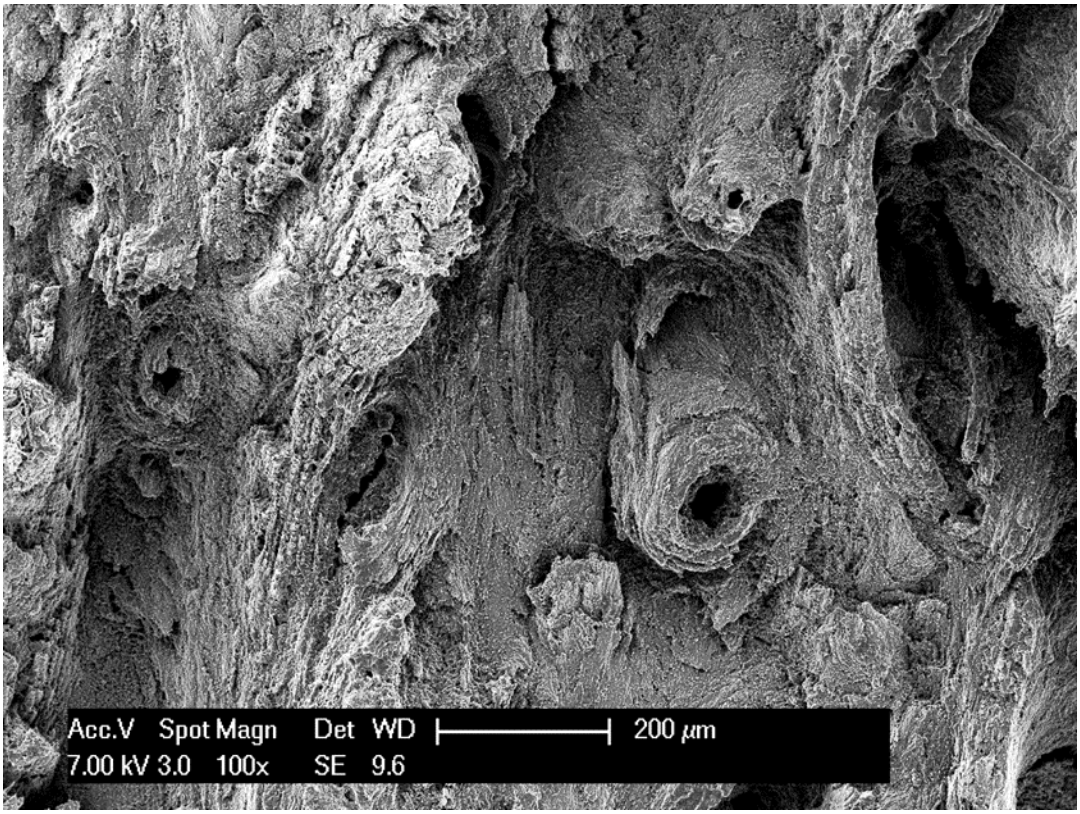

Fig. 28. Scanning electron micrograph of human cranial vault bone sample, after thirty- eight weeks of bacterial incubation, showing clear signs of demineralization and bone remodelling. The vascular canal structure appears preserved.

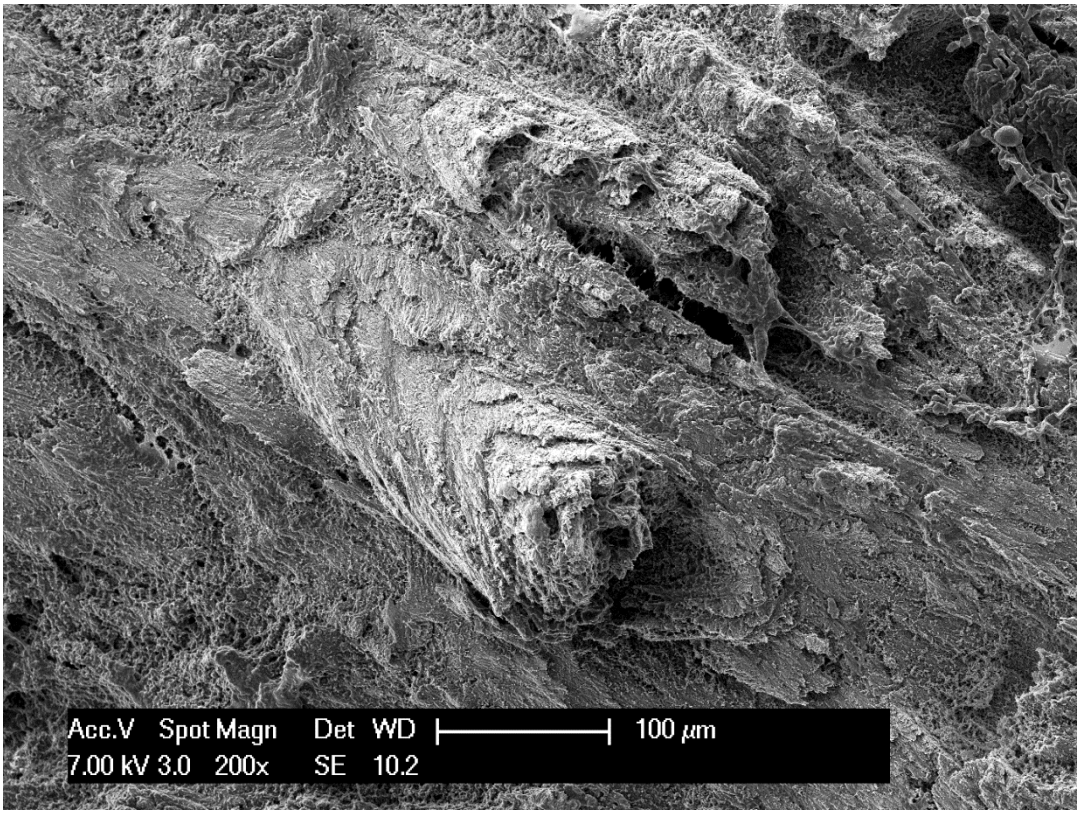

Fig. 29. Scanning electron micrograph of human cranial vault bone sample, after thirty- eight weeks of bacterial incubation. A severe decrease of the bone mineral content and bone remodelling are shown. The lamellar structure of the osteon is well preserved.

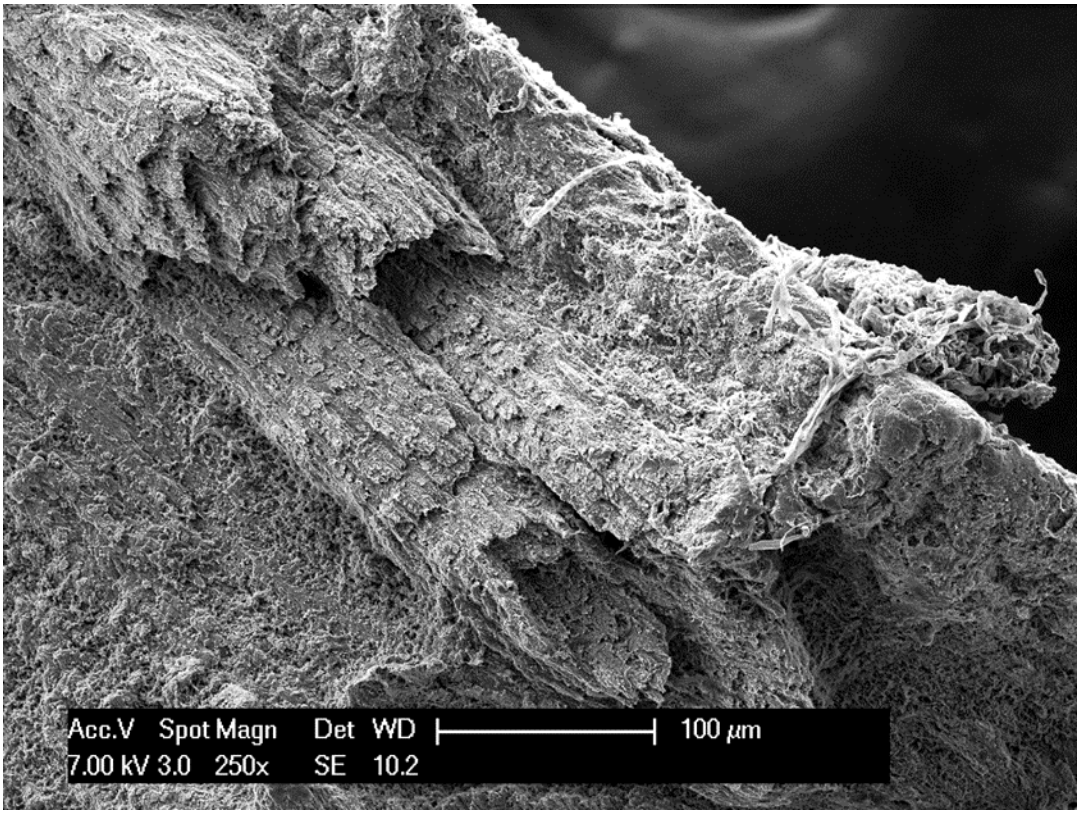

Fig. 30. Scanning electron micrograph of human cranial vault bone sample, after thirty- eight weeks of bacterial incubation, showing some tubular structure, unrelated to the osteonic structure, with and average diameter of 60 microns and running parallel to one another. Clear signs of demineralization are observed.

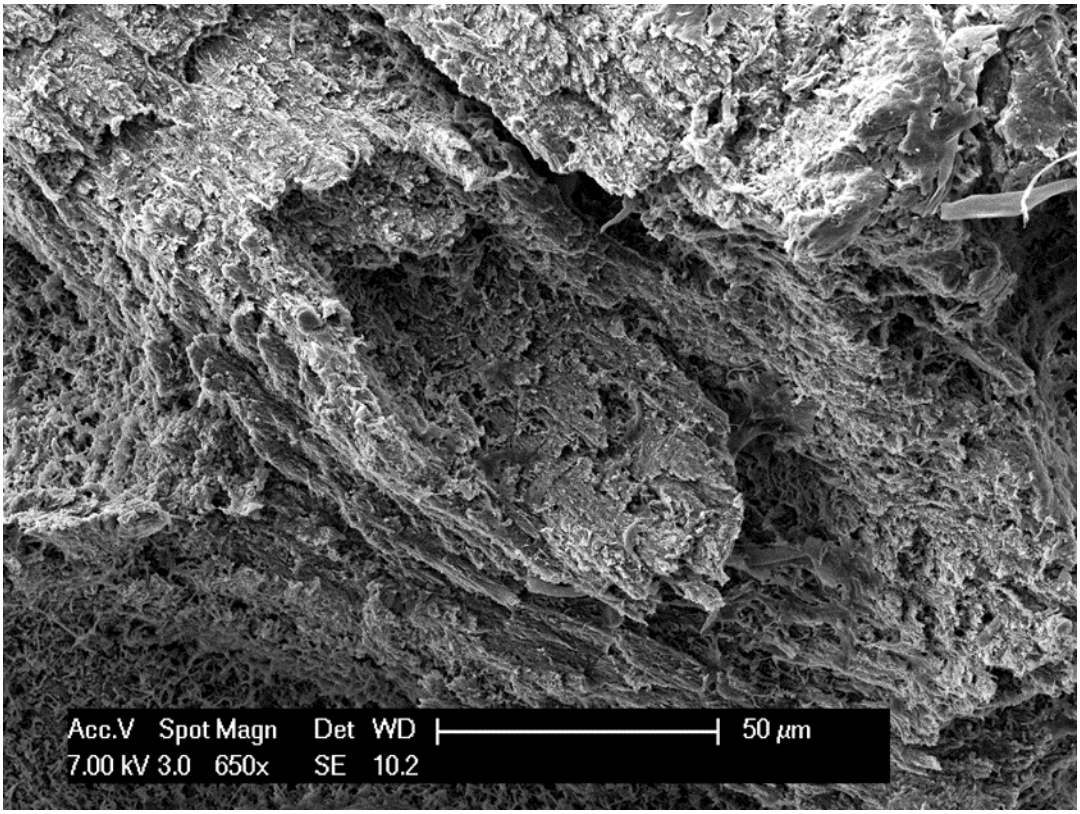

Fig. 31. Higher magnification detail of Fig. 30, showing a lamellate-like structure. Clear signs of severe demineralization are observed.

Interval 6 (39 to 48 week-long incubation period, Fig. 32-39):

The observations carried out during the interval from thirty-nine to forty-eight weeks of bacterial incubation proved that the rate of bone demineralization still increased, and again there was no evidence of saving areas or preferential areas of build-up. Although the vascular canals were visibly affected by demineralization, their structure remained morphologically intact. On the contrary, nearly all the compact lamellar bone tissue showed a significant structural alteration and the bone lamellar pattern was clearly recognizable only in few limited regions. All the analysed samples revealed the same large diameters tubular structure already described in the previous observation interval (interval 5: from 21 to 38 weeks of bacterial incubation), with an unaltered, identical morphology: average diameter of about 50 microns; always run parallel to one another, apparently did not ramify or merge into each other, spatial organization totally respectful of the vascular canal structure (no contact between tubular structures and vascular canals). Inside a number of these tunnels some canalicular and semi-canalicular structures are observed (Fig. 37-39).

No tubular structure of diameter ranging from 5 to 10 microns was detected. Only a single tubular structure adjacent the outer circumferential lamellae was observed (Fig. 29).

No bone alteration was observed in any of the untreated samples (bone samples incubated in thioglycollate), nor at time 0, nor at ending stage (48 week-long incubation period, Fig. 40-42).

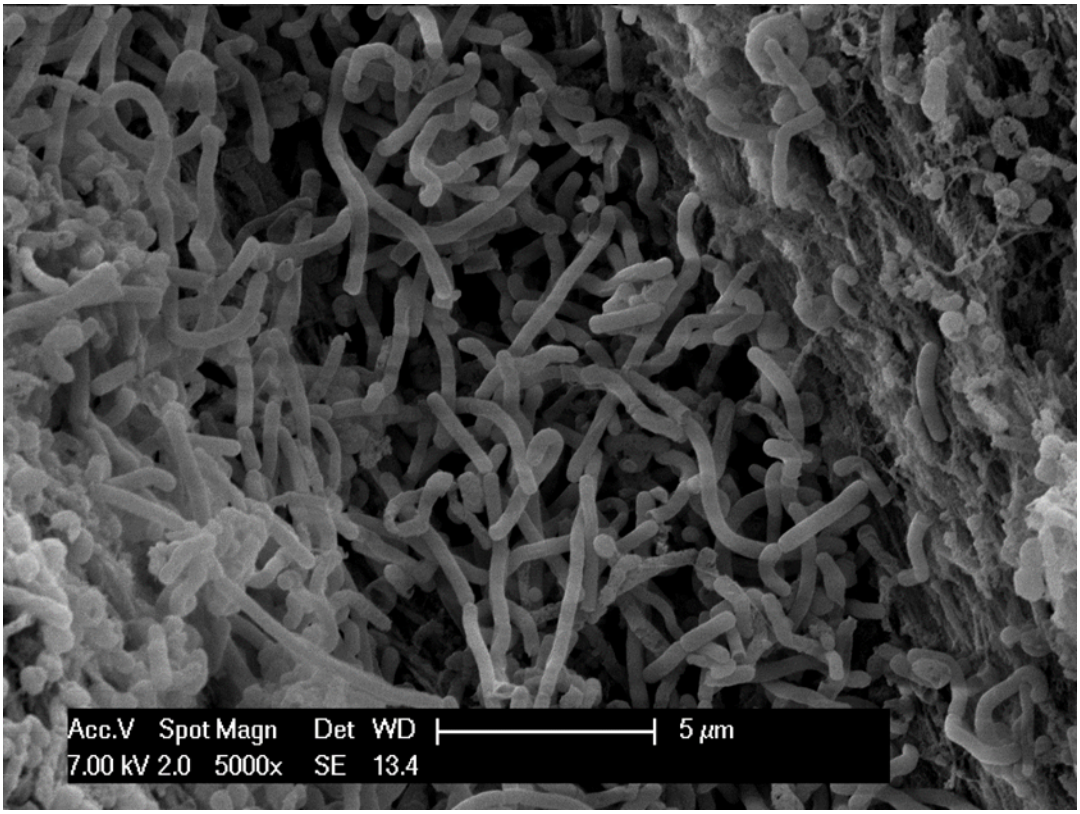

Fig. 32. Scanning electron micrograph of human cranial vault bone sample, after forty-eight weeks of bacterial incubation. A large amount of differently shaped bacteria is shown.

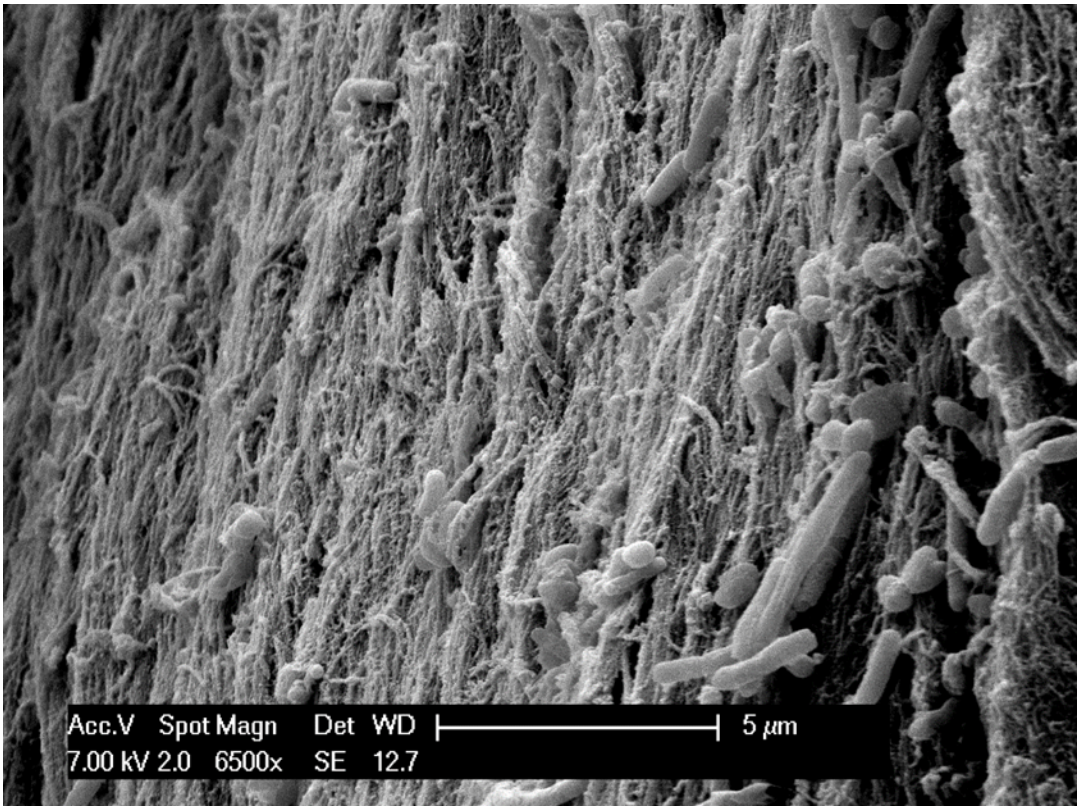

Fig. 33. Scanning electron micrograph of human cranial vault bone sample, after forty-eight weeks of bacterial incubation. As a result of the demineralization process, collagen fibrils on the bone surface are exposed and clearly visible. Several bacteria (cocci and bacilli of different size) are also shown, not only on the surface but also between the collagen fibrils.

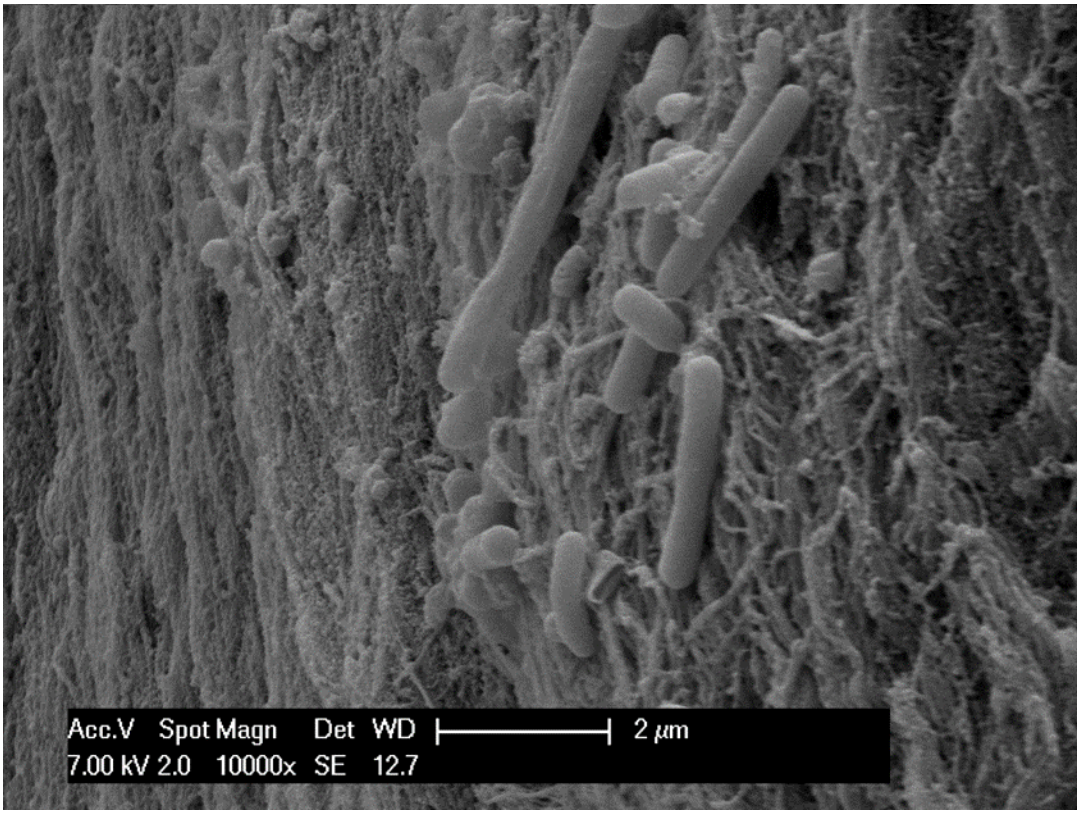

Fig. 34. Scanning electron micrograph of human cranial vault bone sample, after forty-eight weeks of bacterial incubation, showing a polymorph bacterial flora, tightly adhered to the demineralised collagen fibrils.

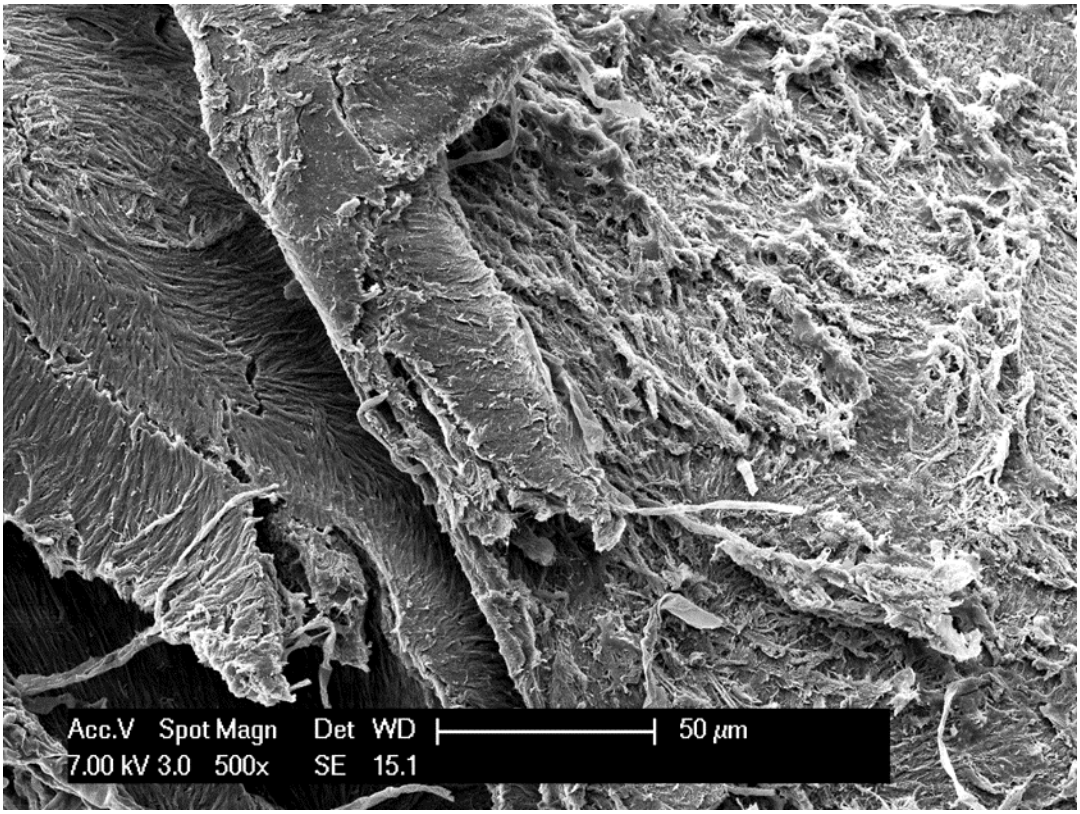

Fig. 35. Scanning electron micrograph of human cranial vault bone sample, after forty-eight weeks of bacterial incubation, showing next to the outer circumferential lamellae a singular tubular structure, with a diameter of about 40 microns. A severe demineralization is observed.

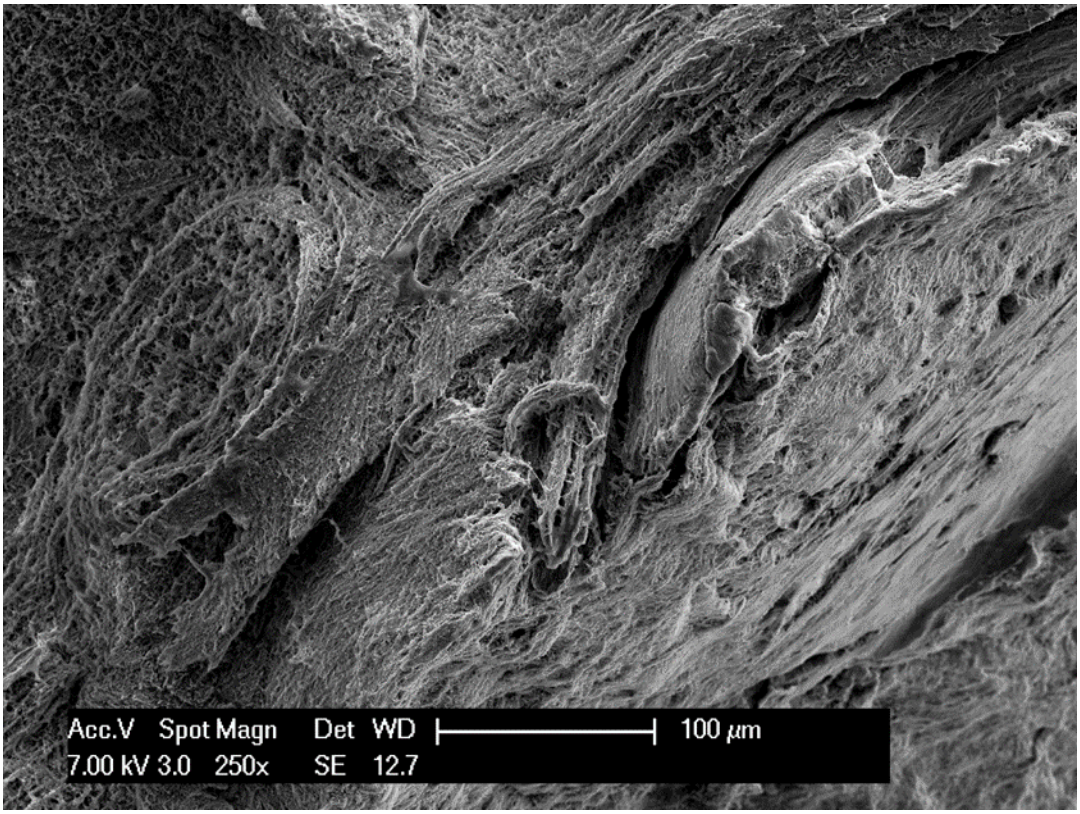

Fig. 36. Scanning electron micrograph of human cranial vault bone sample, after forty-eight weeks of bacterial incubation, showing widespread signs of severe demineralization and bone remodelling. A tubular structure, with an average diameter of 20 microns and a lamellate content, is observed.

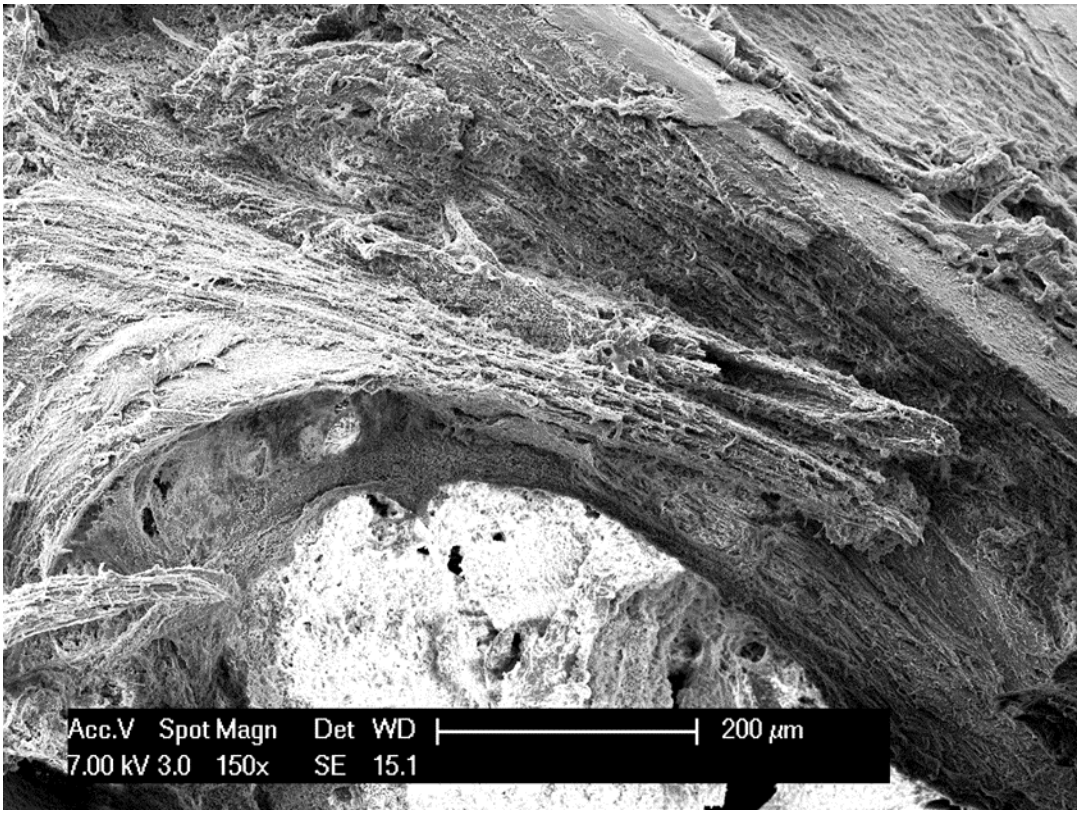

Fig. 37. Scanning electron micrograph of human cranial vault bone sample, after forty-eight weeks of bacterial incubation, showing some tubular shaped, mutually parallel structures (average diameter about 50 microns). Severe demineralization and bone remodelling are observed.

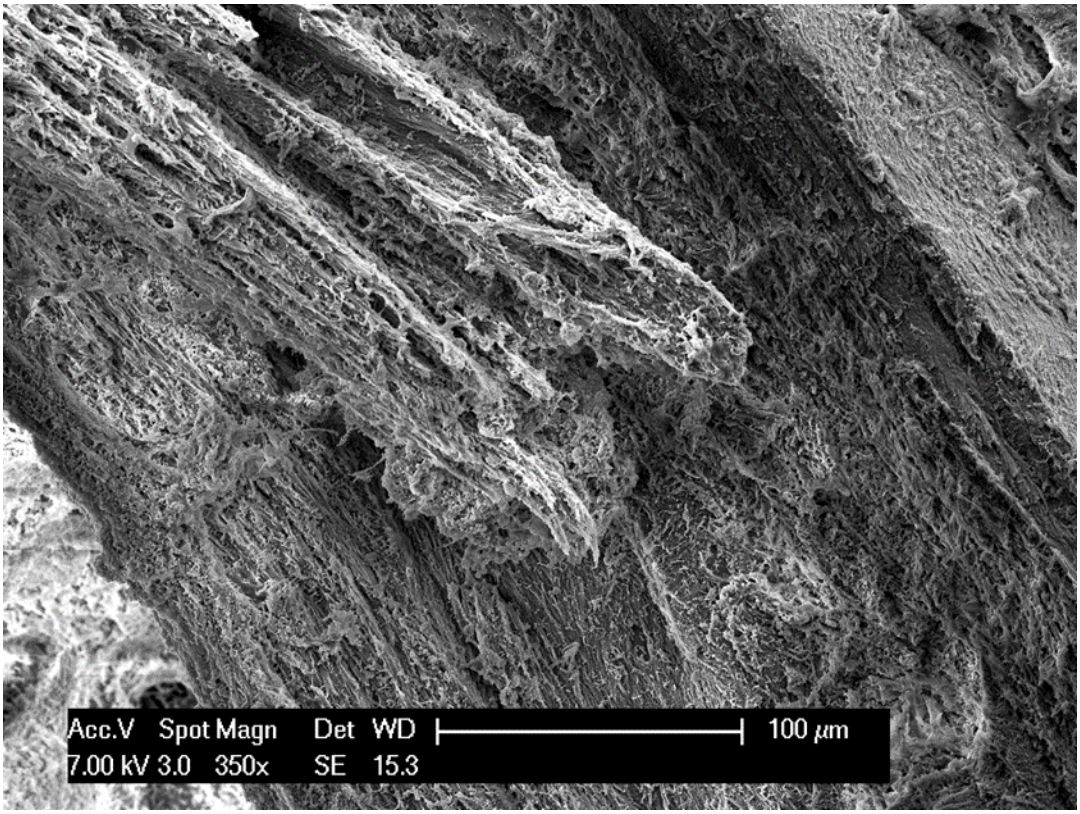

Fig. 38. Higher magnification detail of Fig. 37. A complex network of canalicular and semi- canalicular structures are observed inside each tunnel. Severe demineralization and bone remodelling are observed.

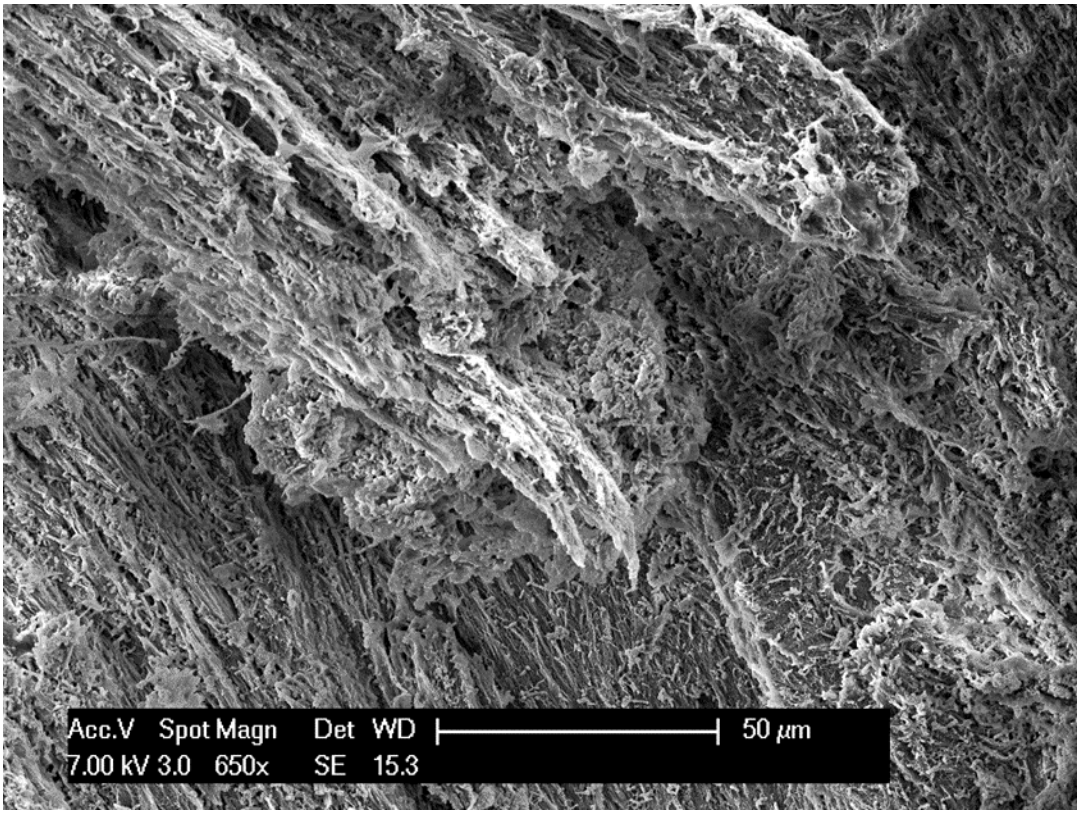

Fig. 39. Detail of Fig. 38, showing the canalicular network fulfilling each tunnel-shaped structure. Severe demineralization is observed.

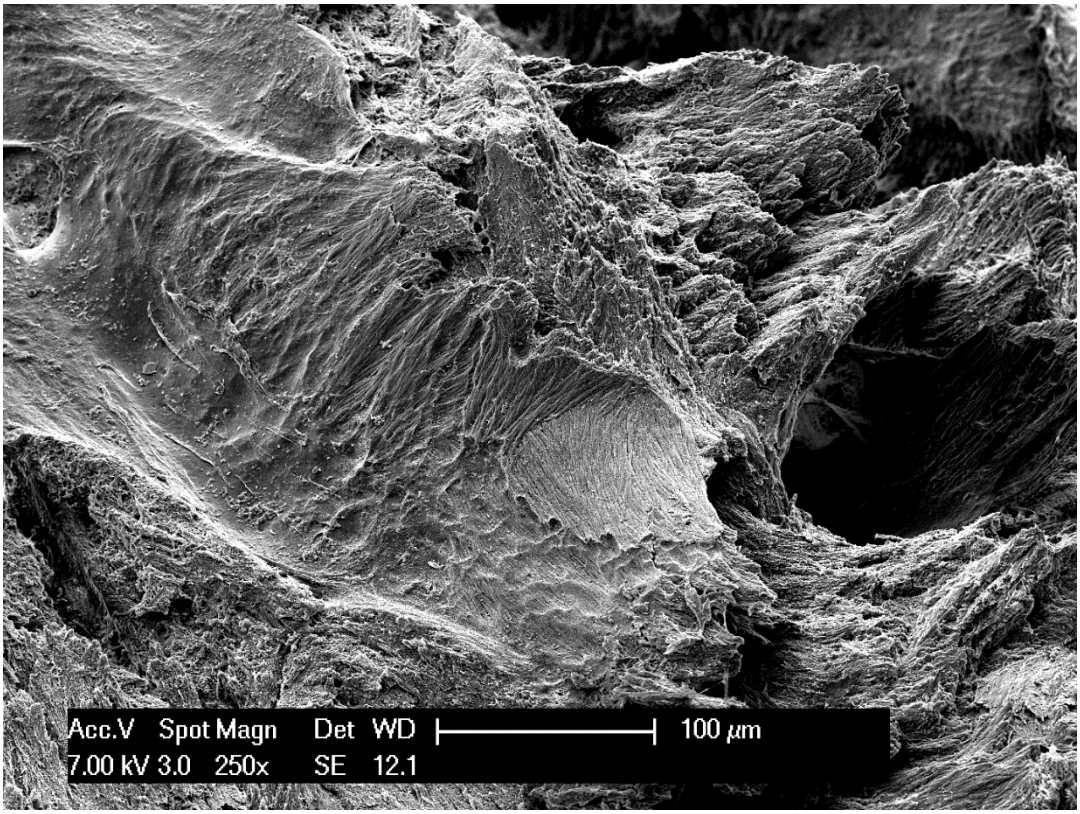

Fig. 40. Scanning electron micrograph of the fracture surface of human cranial vault bone sample, after forty-eight weeks of incubation in thioglycollate. No evidence of bone remodelling is observed and the bone tissue appears well preserved.

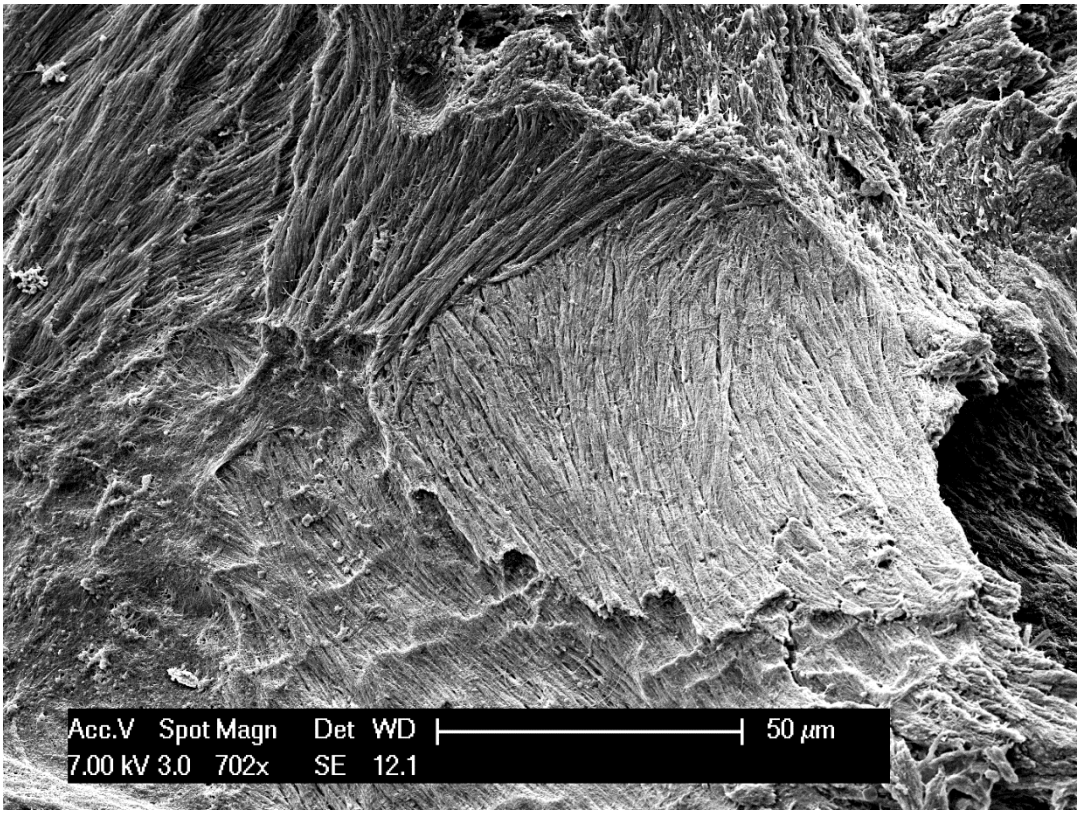

Fig. 41. Higher magnification detail of Fig. 40, showing a well preserved bone tissue, with typical structures of lamellar mature bone.

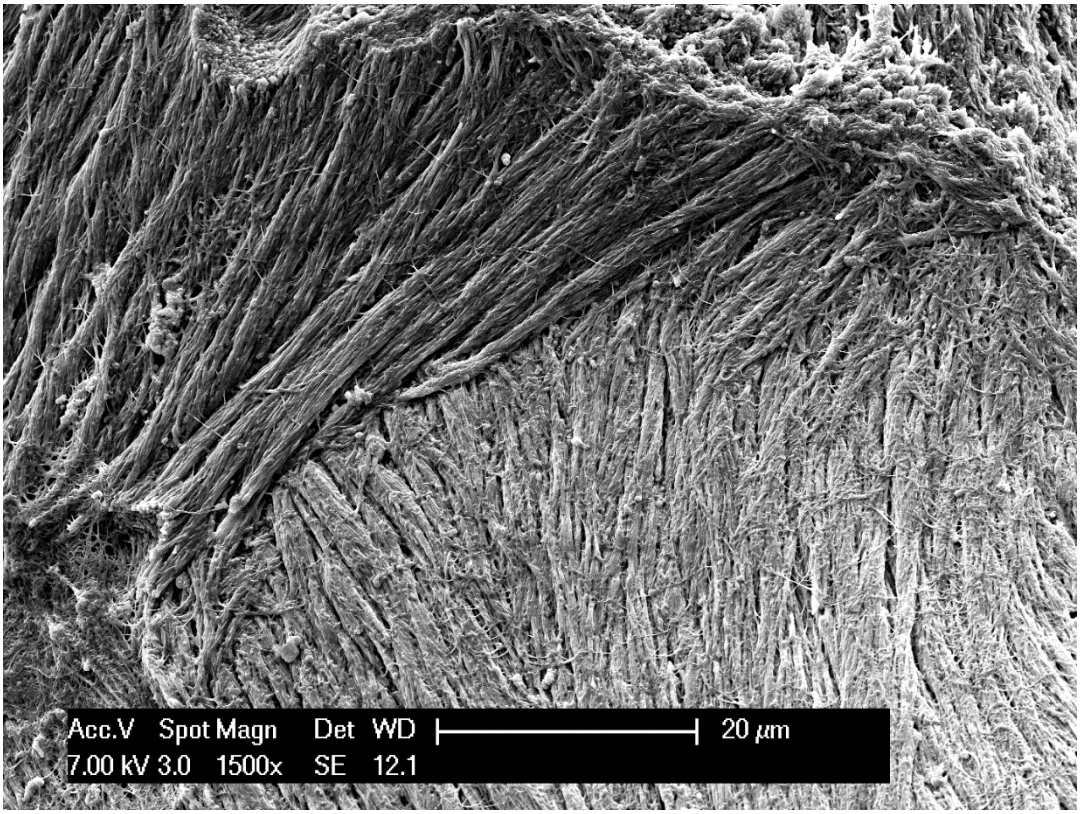

Fig. 42. Higher magnification detail of Fig. 41, showing a remarkably well preserved bone tissue, with differently oriented calcified collagen fibrils. No evidence of bone remodelling is observed.

DISCUSSION AND CONCLUSION

As reported in scientific literature, bone tunnelling in both archaeological bone and forensic bone samples may be schematically organised into two categories: Wedl tunnels and non-Wedl tunnels (there is also another particular class of tunnelling caused by cyanobacteria, which seems to occur when samples have been immersed in fresh water or salt water [Bell et al. 1991; Bell and Elkerton, 2008; Pesquero et al. 2010]). Wedl tunnels were described for the first time in 1864 (Wedl 1864): they are bored labyrinth-like branching structures caused by fungi, as experimentally proved by Marchiafava et al. (1974) and Fernández-Jalvo et al. (2010) among others, with a diameter ranging from 10 to 15 microns in Type I tunnels (Trueman and Martill, 2002) and from 5 to 10 microns in Type II tunnels.

Non-Wedl tunnels were described by Hackett (1981), who distinguished three types of microscopical focal destruction (MFD): linear longitudinal MFD (with a diameter ranging from 5 to 10 microns and a hypermineralised rim), budded MFD (with a diameter ranging from 30 to 60 microns, a mineralised cuff and an irregular shape) and lamellate MFD (with a diameter ranging from 10-20 microns to 60-250 microns, a mineralised edge and a lamellate content). A number of analysis demonstrated that all three kinds of non- Wedl tunnels are a consequence of bacterial activity (Hackett 1981; Yoshino et al. 2010; White and Booth 2014).

To date, there are two major hypotheses about bone tunnelling aetiology: the "exogenous model", where hard tissues remain both morphologically and biomolecularly intact till skeletonized, time when they are exposed to biodeterioration due to environmental factors and to bacteriologically induced bioerosion (Turner-Walker and Jans, 2008; Fernandez-Jalvo et al. 2010; Muller et al. 2011), and the "endogenous model", that correlate bone microstructural deterioration with endogenous microbial activity (Jans et al. 2004; Guarino et al. 2006; Nielsen-Marsh et al. 2007; Hollund et al. 2012; White and Booth 2014).

On the basis of the nearly complete equivalence of the morphological pattern of the micro-tunnelling we previously observed in human post-mortem bone samples (both archaeological samples [Fig. 43 and 44] and forensic specimens [Fig. 45 and 46]) as well as in human tartar specimens [Fig. 47 and 48; the figures from 43 to 48 were inserted as such being unpublished material], this research introduces a conceivable endogenous model of human bone biodeterioration, based on the action of oral cavity endogenous microorganisms.

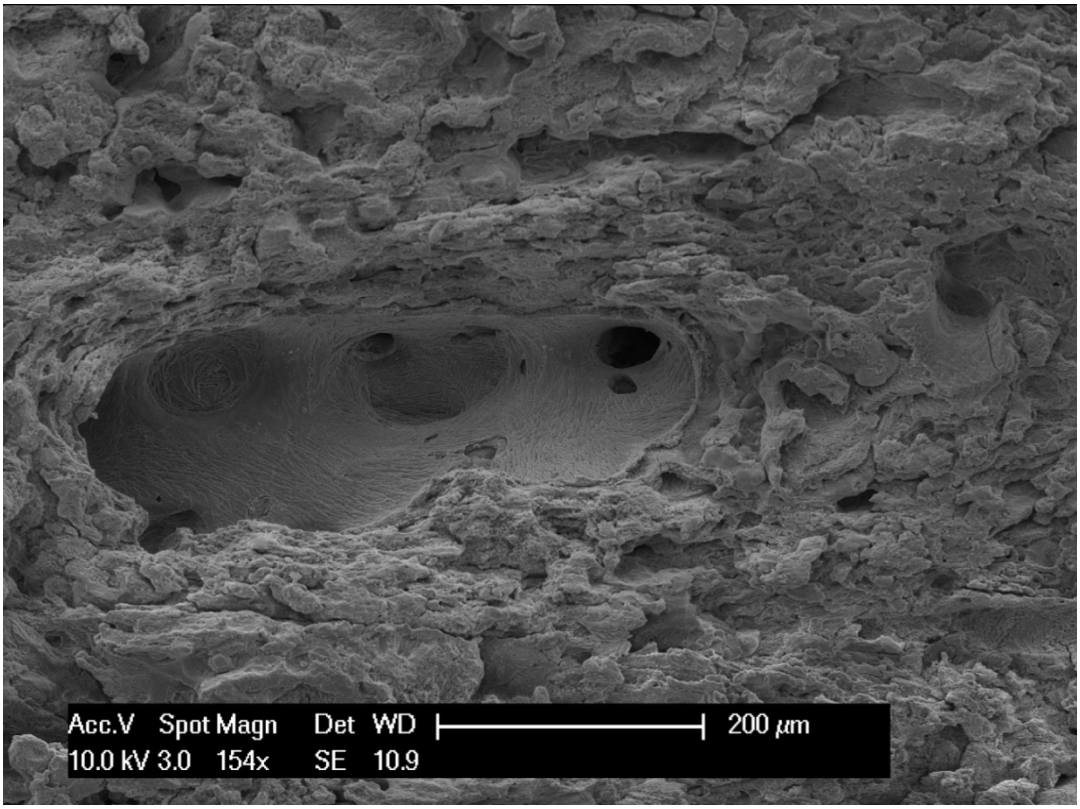

Fig. 43. Scanning electron micrograph of the substantia compacta of a femur (archaeological human bone sample, around year 1000 CE). The vascular canal structure appears well-preserved, while a complete demineralisation and bone remodelling are clearly visible.

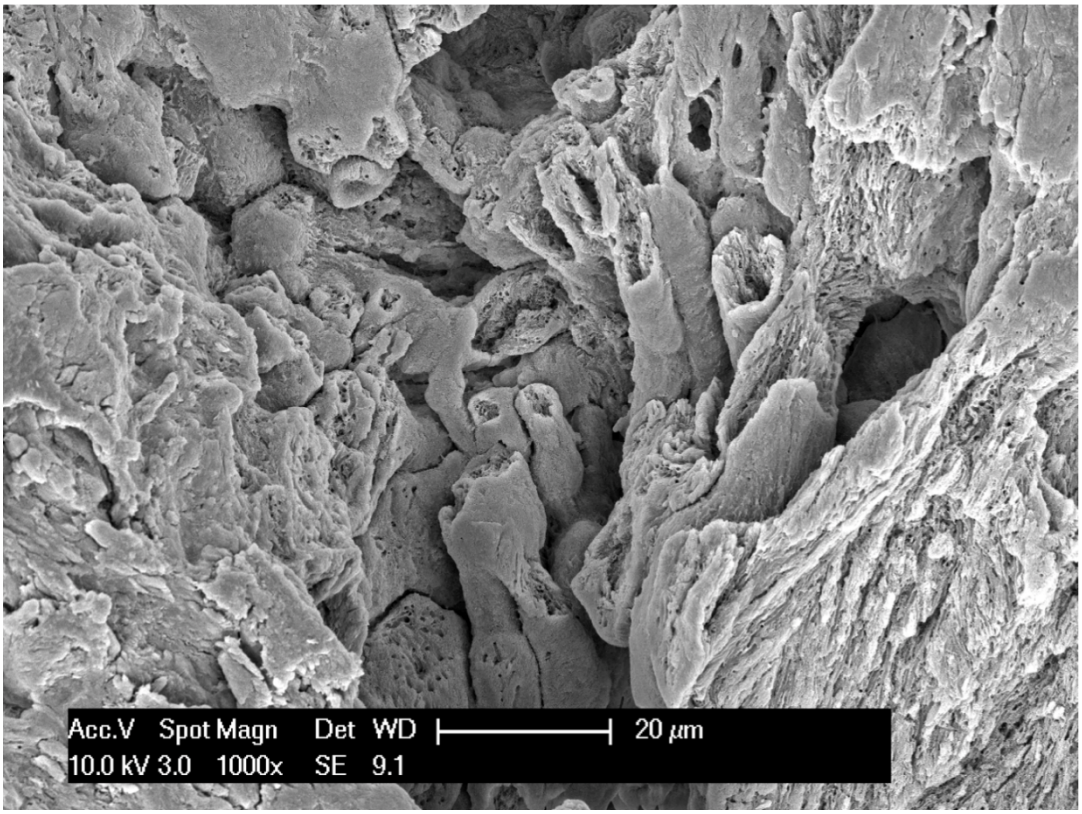

Fig. 44. Scanning electron micrograph of the substantia compacta of a femur (archaeological human bone sample, around year 1000 CE), showing a number of linear longitudinal MFD (non-Wedl).

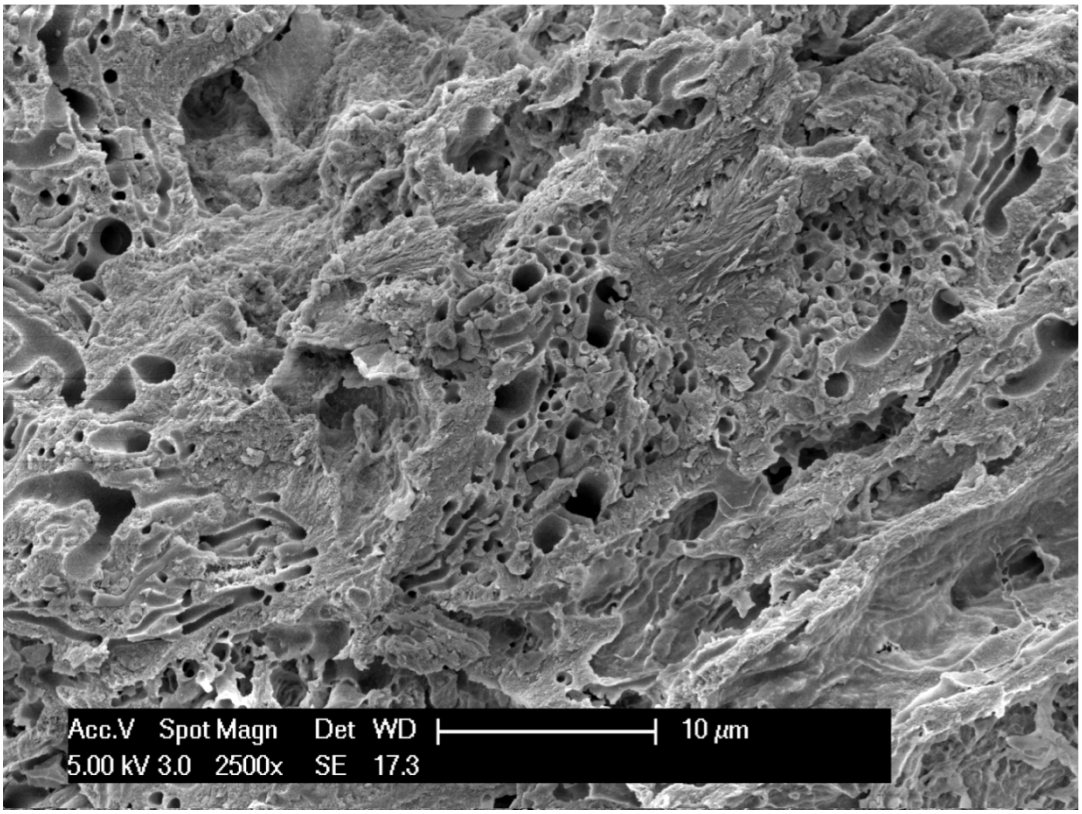

Fig. 45. Scanning electron micrograph of the substantia compacta of a tibia (forensic bone sample), showing a lot of labyrinth-like tubular structures with 1 micron average diameter. Severe cone remodelling, a great number of cribriform cavities and some bacilli are observed.

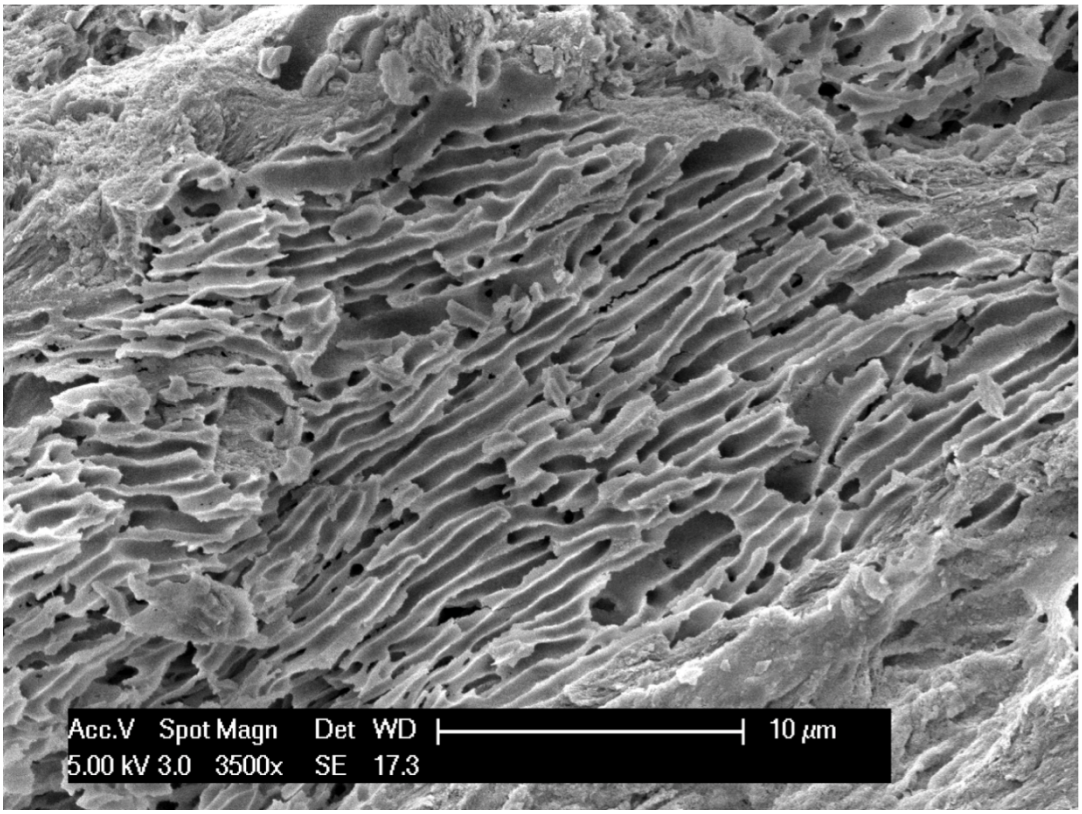

Fig. 46. Scanning electron micrograph of the substantia compacta of a tibia (forensic bone sample, estimated PMI: two years), showing an intricate honeycomb pattern of destruction, formed by small canalicular structures and little cribriform cavities.

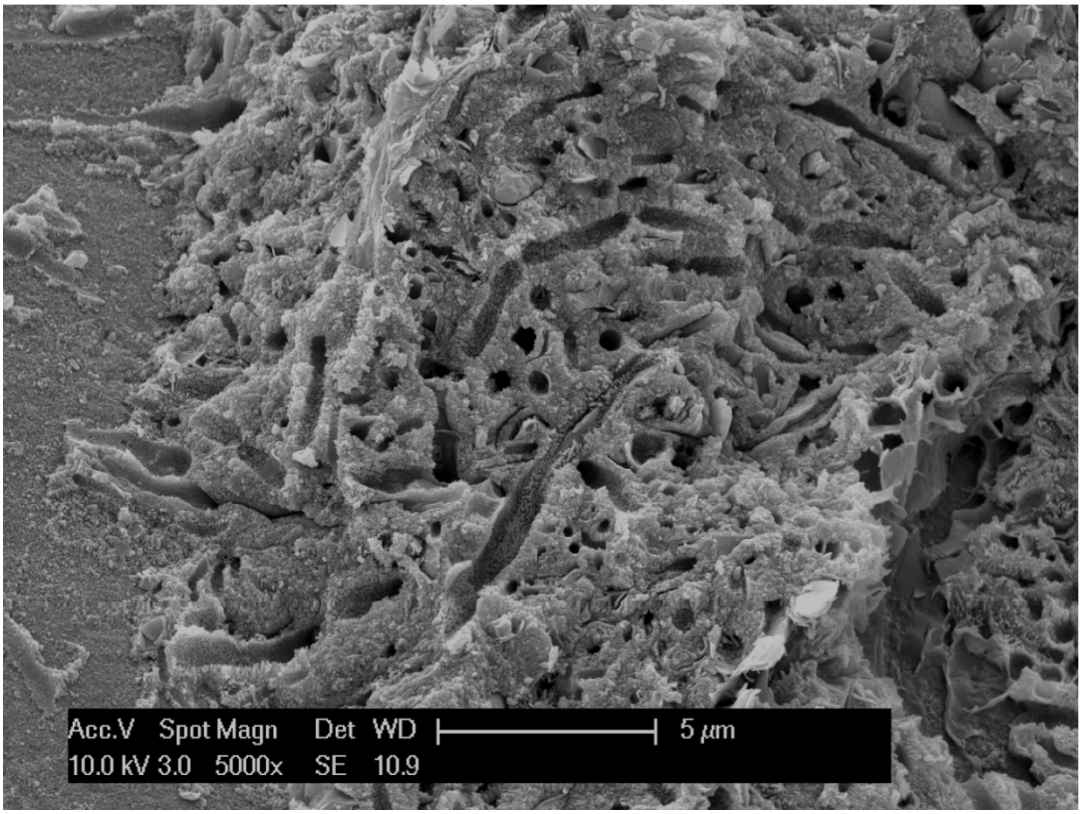

Fig. 47. Scanning electron micrograph of human tartar sample, showing small, round cavities and tubular structures.

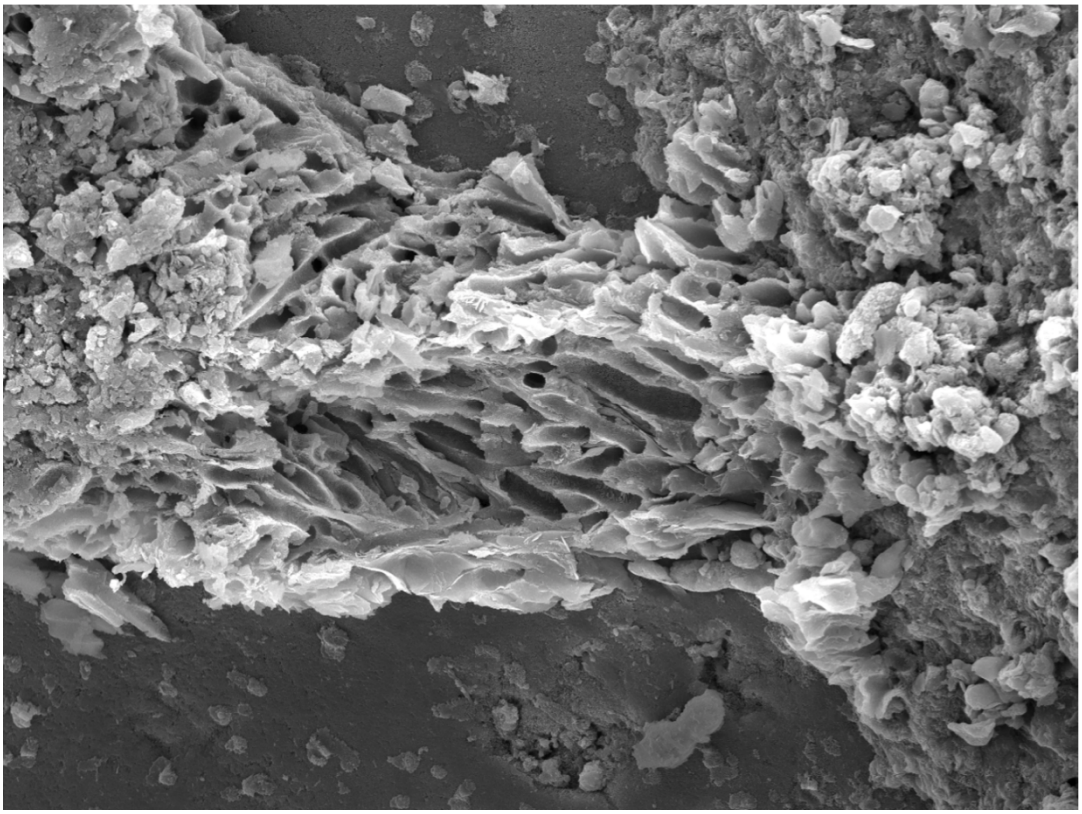

Fig. 48. Scanning electron micrograph of human tartar sample, showing small, round cavities and tubular structures.

Six bacterial species were isolated and identified from donor's tartar samples using MALDI-TOF MS:

- *Actinomyces odontolyticus* (score ≥ 2.000);
- *Actinomyces turicensis* (score between 1.700 and 1.999);
- *Lactobacillus delbrueckii* (score ≥ 2.000);
- *Lactobacillus paracasei* (score ≥ 2.000);
- *Lachnoanaerobaculum orale* (score ≥ 2.000);
- *Streptococcus constellatus* (score ≥ 2.000).

As discussed in literature, MALDI-TOF MS is able to identify with a high level of discriminatory power *Lactobacillus paracasei*, *Lactobacillus delbrueckii* and *Streptococcus constellatus* (Schott et al. 2016; Arinto-Garcia et al. 2015), while for *Actinomyces spp* and *Lachnoanaerobaculm orale* , which are not commonly isolated from clinical specimens, MALDI-TOF MS was reported to provide a less accurate identification (Könönen and Wade 2015; Lynch et al. 2016; Ng et al. 2012), therefore a 16S rRna sequencing was performed in order to confirm *Actinomyces spp* and *Lachnoanaerobaculm orale* identification.

Actinomyces are significatively represented in dental plaque of healthy individuals but they are also known to play a role in several dental and oral infections (for example caries, endodontic infections and dental implant- associated infections) (Sarkonen et al. 2005; Könönen and Wade 2015). The spectrum of diseases associated with *Actinomyces odontolyticus* and *Actinomyces turicensis* also includes pulmonary infections (Hall et al. 2001; Peaper et al. 2015), genitourinary infections (Hall et al. 2001; Sabbe et al. 1999), bacteremias and sepsis (Clarridge and Zhang 2002; Hall et al. 2001; Cone et al. 2003; Hansen et al. 2009; Kerttula et al. 2005).

In advanced dental caries, *Lactobacilli* are commonly considered as a secondary colonizer, but evidence exists of their role in exacerbate pre-existing lesions (Badet and Thebaud 2008).

Only a little is known about *Lachnoanaerobaculum orale*, an obligately anaerobic, Gram-positive, spore-forming bacillus isolated from the saliva of a healthy young man (Hedberg et al. 2012).

Streptococcus constellatus is commonly isolated from the respiratory tract and it is a well known commensal of the oropharyngeal, urogenital and gastrointestinal microbiota (Socransky et al. 1998; Whiley et al. 1992).

As documented in scientific literature on human oral microbiome, the complexity of the oral bacterial community in a living human is so considerable that, as Wade wrote, it seems to be quite an "impossible task to assign a role for each organism in the community" (Wade 2013) and diseases associated with the microbiome are not caused by a single pathogen but result from the complex interaction between the different microorganisms present (that collaborate to evade the host's immune response (Brook I 1994), work synergically to degrade complex substrates (Wade 2013) etc…), the human host and the environmental conditions.

Basing on these considerations, it seemed inappropriate to create an experimental model of human bone biodeterioration to investigate a mono-microbial hypotesis or to try to identify the peculiar role/function of a specific bacterium within a process, necessarily developed in a poli-microbic environment, in which an immune competence does not exist anymore and in which also anatomic physiological barriers are in decay, if not even completely destroyed.

We decided therefore to pool all the bacterial species in a single experimental model.

During the first four weeks of incubation with the bacterial strains isolated from tartar donors (*Lachnoanaerobaculum orale*, *Actinomyces odontolyticus*, *Streptococcus constellatus*, *Lactobacillus paracasei*, *Lactobacillus delbrueckii* and *Actinomyces turicensis*) no morphological changes were observed in any sample but an incremental, ubiquitous, bone demineralization: this observation seems to confirm Herrmann's previous hypotheses (1977) on decalcification as one of the earliest phases in post-mortem bone deterioration, as well as Hackett's considerations (1981) about the decrease in mineral component of hard tissue as probably the earliest sign of post mortem bone change and the study of Collins et al. (2002) who hypothesized that a localised demineralization is the starting stage of the microbial attack.

During the incubation period from five weeks to twenty weeks, while the demineralization process became more and more pronounced, evidences of bone remodeling arose: a progressive, substantial morphological alteration of large areas of bone tissue was observed and large cribriform cavities, not attributable to any physiological human bone structure, appeared.

The presence of budded-type MFD and lamellate tunnels (specifically located into the mesosteal area, whereas outer and inner circumferential lamellae are never invaded) was widely documented in examinations carried out during the interval from twenty-one to thirty-eight weeks of bacterial incubation; moreover, the observations conducted during the interval from thirty-nine to forty-eight weeks of bacterial incubation revealed a

number of budded-type MFD and lamellate tunnels too. These morphological data are consistent with Jans et al. (2004) statement that budded and lamellate tunnelling types are often found in association with each other.

Building up an experimental endogenous model of human bone biodeterioration in laboratory allows to standardise multiple parameters and omit known confounders, but it inevitably has to deal with some limiting factors (i.e., in this particular case, bacteria were determined by voluntary donors and small sampling population size, the number of available bone samples was limited, environmental conditions differed from those of the natural process, and the study time period was limited).

Despite these limitations, the bioerosion processes observed starting from the fifth week of incubation with the bacterial strains isolated from tartar donors, revealed an unexpected complete equivalence of the morphological pattern with both the phenomena described in literature and the ones we ourselves previously identified in our archaeological bone and forensic bone samples.

The macroscopical appearance was well preserved in all bone fragments throughout the whole experiment time, even when they had severe diagenetic changes at the microscopic level. These data are fully coherent with Hackett's observations (1981) and Hanson and Buikstra's notes that the periosteal surface seems to be always preserved (1987).

All the samples observed in this research showed that not only outer and inner circumferential lamellae are never invaded by non-Wedel tunnels but also that vascular canals are never affected by any degenerative alteration other than a demineralization. These observations might support the hypothesis that, somehow, adverse conditions for the proliferation of endogenous bacteria involved in human bone post mortem biodeterioration exist in both the microvascular environment and the external environment, after death.

In nature, a lot of environmental variables (i.e. oxygen rate, humidity, temperature, pH, presence of microorganisms, flora and fauna activities) as well as several individual variables (i.e. body size, age, cause of death), associated in different ways, might hypothetically affect the post-mortem degeneration process of organs and tissues. However, the resulting morphological patterns of bone tissue biodeterioration (Wedl and non-Wedl types of MFD), are fairly identical.

Although the experimental model here proposed uses a limited range of bacteria and keeps some parameters fixed (i.e. temperature), the bone changes obtained can be

completely superimposed to the ones observed in natural samples.

In the light of the complexity of post-mortem diagenetic changes in bone and of the non-unequivocalness of results of the experimental investigations conducted to verify the different models of hard tissue bioerosion-biodeterioration, we could hypothesize that bacteria associated with bone tissue deterioration can act synergistically and sequentially in nature (i.e. metabolic products of some bacteria might generate a favourable microenvironment for other bacterial proliferation and activity). Furthermore the "endogenous model" of bone biodeterioration and the "exogenous model" of hard tissue bioerosion-biodeterioration might not be mutually exclusive, but they could rather occur sequentially: the first in earlier post-mortem stages (Jans et al. 2004; Guarino et al. 2006; Nielsen-Marsh et al. 2007; Hollund et al. 2012; White and Booth 2014), the latter possibly after the skeletonization, when hard tissues are exposed to biodeterioration due to environmental factors and to bioerosion due to environment-associated microorganisms (Turner-Walker and Jans 2008; Fernandez-Jalvo et al. 2010; Muller et al. 2011).

The observations here exposed suggest that post-mortem morphological changes in bone can result from complex interactions between various bacterial strains acting partially by overlap, partially by sequence, rather than being merely linked to the bacterial genus.

REFERENCES

1. Aho AJ, Hirn M, Aro HT, Heikkila JT, Meurman O. Bone bank service in Finland. Experience of bacteriologic, serologic and clinical results of the Turku Bone Bank 1972-1995. Acta Orthop Scand. 1998; 69: 559-565.
2. Alkass K, Buchholz BA, Druid H, Spalding KL. Analysis of 14C and 13C in teeth provides precise birth dating and clues to geographical origin. Forensic Sci Int. 2011 Jun 15;209(1-3):34-41. doi: 10.1016/j.forsciint.2010.12.002. Epub 2011 Jan 3.
3. Arinto-Garcia R, Pinho MD, Carriço JA, Melo-Cristino J, Ramirez M. Comparing Matrix-Assisted Laser Desorption Ionization-Time of Flight Mass Spectrometry and Phenotypic and Molecular Methods for Identification of Species within the Streptococcus anginosus Group. J Clin Microbiol. 2015 Nov;53(11):3580-8. doi: 10.1128/JCM.01892-15. Epub 2015 Sep 9.
4. Ascenzi A, Silvestrini G. Bone-boring marine micro-organisms: an experimental investigation. J. Human Evol. 1984 Sep; 13(6):531-36.
5. Badet C, Thebaud NB. Ecology of lactobacilli in the oral cavity: a review of literature. Open Microbiol J. 2008;2:38-48. doi: 10.2174/1874285800802010038. Epub 2008 Apr 29.
6. Balzer A, Gleixner G, Grupe G, Schmidt HL, Schramm S, Turban-Just S. In vitro decomposition of bone collagen by soil bacteria: the implications for stable isotope analysis in archaeometry. Archaeometry. 1997 Aug;39(2):415–29.
7. Bell LS, Boyde A, Jones SJ. Diagenetic alteration to teeth in situ illustrated by backscattered electron imaging. Scanning. 1991;13(2): 173–83. doi:10.1002/sca.4950130204.
8. Bell LS, Elkerton A. Unique marine taphonomy in human skeletal material recovered from the medieval warship Mary Rose. Int. J Osteoarchaeol. 2008 Sep/Oct;18(5):523–35. doi:10.1002/oa.952.
9. Bell LS, Skinner MF, Jones SJ. The speed of post mortem change to the human skeleton and its taphonomic significance. Forensic Sci Int. 1996 Sep 30;82(2):129-40.
10. Brook I. The role of encapsulated anaerobic bacteria in synergistic infections. FEMS Microbiol Rev. 1994 Jan;13(1):65-74.
11. Buckley K, Kerns JG, Birch HL, Gikas PD, Parker AW, Matousek P, Goodship AE. Functional adaptation of long bone extremities involves the localized "tuning" of the cortical bone composition; evidence from Raman spectroscopy. J Biomed Opt. 2014;19(11):111602. doi: 10.1117/1.JBO.19.11.111602.
12. CDC. Update: Allograft-associated bacterial infections. United States, 2002. MMWR 2002; 51: 207-210.

13. CDC. Invasive Streptococcus pyogenes after allograft implantation Colorado, 2003. MMWR 2003; 52: 1173-1176.
14. Child AM, Gillard RD, Pollard AM. Microbially-induced promotion of amino acid racemization in bone: isolation of the microorganisms and the detection of their enzymes, J. Archaeol Sci. 1993 Mar;20(2);159–68.
15. Clark MA, Worrell MB, Pless JE. Postmortem Changes in Soft Tissues. In Forensic Taphonomy: The Postmortem Fate of Human Remains. CRC Press, 1997:151-64.
16. Clarridge JE 3rd, Zhang Q. Genotypic diversity of clinical Actinomyces species: phenotype, source, and disease correlation among genospecies. J Clin Microbiol. 2002 Sep;40(9):3442-8.
17. Collins MJ, Nielsen-Marsh CM, Hillier J, Smith CI, Roberts JP, Prigodich RV, Wess TJ, Csapö J, Millard A.R, Turner-Walker G. The survival of organic matter in one: a review. Archaeometry. 2002 Aug;44 (3):383-94.
18. Cone LA, Leung MM, Hirschberg J. Actinomyces odontolyticus bacteremia. Emerg Infect Dis. 2003 Dec;9(12):1629-32.
19. Cook GT, MacKenzie AB. Radioactive isotope analyses of skeletal materials in forensic science: a review of uses and potential uses. Int J Legal Med. 2014 Jul;128(4):685-98. doi: 10.1007/s00414-014-0970-8. Epub 2014 Feb 20.
20. Creagh D, Cameron A. Estimating the Post-Mortem Interval of skeletonized remains: The use of Infra-red spectroscopy and Raman spectro-microscopy. Radiat Phys Chem. 2017 Aug;137:225-29.
21. Creamer JI, Buck AM. The assaying of haemoglobin using luminol chemiluminescence and its application to the dating of human skeletal remains. Luminescence. 2009 Sep-Oct;24(5):311-6. doi: 10.1002/bio.1110.
22. Donaldson AE, Lamont IL. Biochemistry changes that occur after death: potential markers for determining post-mortem interval. PLoS One. 2013 Nov 21;8(11):e82011. doi: 10.1371/journal.pone.0082011. eCollection 2013.
23. Fernández-Jalvo Y, Andrews P, Pesquero D, Smith C, Marın-Monfort D, Sanchez B, Geigl E-M, Alonso A. Early bone diagenesis in temperate environments. Part I: surface features and histology, Palaeogeogr. Palaeoclimatol Palaeoecol. 2010 Mar;288(1-4):62–81.
24. Forbes SL, Stuart BH, Dadour IR, Dent BB. A preliminary investigation of the stages of adipocere formation. J Forensic Sci. 2004 May;49(3):566-74.
25. Goff ML. Estimation of Postmortem Interval Using Arthropod Development and Successional Patterns. Forensic Sci Rev. 1993 Dec;5(2):81-94.
26. Guarino FM, Angelini F, Vollono C, Orefice C. Bone preservation in human remains from the Terme del Sarno at Pompeii using light microscopy and scanning electron microscopy. J. Archaeol Sci. 2006 Apr;33(4):513–20.

27. Hackett CJ. Microscopical focal destruction (tunnels) in exhumed human bones. Med Sci Law. 1981 Oct;21(4):243-65.
28. Hall V, Talbot PR, Stubbs SL, Duerden BI. Identification of clinical isolates of actinomyces species by amplified 16S ribosomal DNA restriction analysis. J Clin Microbiol. 2001 Oct;39(10):3555-62.
29. Hansen JM, Fjeldsøe-Nielsen H, Sulim S, Kemp M, Christensen JJ. Actinomyces species: A danish survey on human infections and microbiological characteristics. Open Microbiol J. 2009 Jul 23;3:113-20. doi: 10.2174/1874285800903010113.
30. Hedberg ME, Moore ER, Svensson-Stadler L, Hörstedt P, Baranov V, Hernell O, Wai SN, Hammarström S, Hammarström ML. Lachnoanaerobaculum gen. nov., a new genus in the Lachnospiraceae: characterization of Lachnoanaerobaculum umeaense gen. nov., sp. nov., isolated from the human small intestine, and Lachnoanaerobaculum orale sp. nov., isolated from saliva, and reclassification of Eubacterium saburreum (Prevot 1966) Holdeman and Moore 1970 as Lachnoanaerobaculum saburreum comb. nov. Int J Syst Evol Microbiol. 2012 Nov;62(Pt 11):2685-90. doi: 10.1099/ijs.0.033613-0. Epub 2012 Jan 6.
31. Hedges REM. Bone diagenesis: an overview of processes. Archaeometry. 2002 Aug;44(3):319-28. doi: 10.1111/1475-4754.00064.
32. Hedges REM, Millard AR, Pike AWG. Measurements and relationships of diagenetic alteration of bone from three archaeological sites. J Archaeol Sci. 1995 Mar;22(2):201-09.
33. Hedges REM, Millard AR. Bones and groundwater: Towards the modeling of diagenetic processes. J Archaeol Sci. 1995 Mar;22(2):155–64.
34. Herrmann B. Ober die Reste des postcraniale Skelettes des Neanderthalers von Le Moustier. Z. Morph Anthrop. 1977;68(2):129-49.
35. Hollund HI, Jans MME, Collins MJ, Kars H, Joosten I, Kars SM. What Happened Here? Bone Histology as a Tool in Decoding the Postmortem Histories of Archaeological Bone from Castricum, The Netherlands. Int. J Osteoarchaeol. 2012 Sep/Oct;22(5):537–48. doi: 10.1002/oa.1273.
36. Howes JM, Stuart BH, Thomas PS, Raja S, O'Brien C. An investigation of model forensic bone in soil environments studied using infrared spectroscopy. J Forensic Sci. 2012 Sep;57(5):1161-7. doi: 10.1111/j.1556-4029.2012.02236.x. Epub 2012 Aug 6.
37. Jackes M, Sherburne R, Lubell D, Barker C, Wayman M. Destruction of microstructure in archaeological bone: a case study from Portugal. Int. J Osteoarchaeol. 2001 Nov/Dec;11(6):415–32. doi: 10.1002/oa.583.
38. Jans MME, Nielsen-Marsh CM, Smith CI, Collins MJ, Kars H. Characterisation of microbial attack on archaeological bone. J. Archaeol Sci. 2004 Jan;31(1):87-95. doi: 10.1016/j.jas.2003.07.007.

39. Jin Y, Yip HK. Supragingival calculus: formation and control. Crit Rev Oral Biol Med. 2002;13(5):426-41.
40. Kerttula AM, Carlson P, Sarkonen N, Hall V, Könönen E. Enzymatic/biochemical analysis of Actinomyces with commercial test kits with an emphasis on newly described species. Anaerobe. 2005 Feb-Apr;11(1-2):99-108. Epub 2005 Feb 1.
41. Knight B. Methods of dating skeletal remains. Med Sci Law. 1969 Oct;9(4):247-52.
42. Könönen E, Wade WG. Actinomyces and related organisms in human infections. Clin Microbiol Rev. 2015 Apr;28(2):419-42. doi: 10.1128/CMR.00100-14.
43. Longato S, Wöss C, Hatzer-Grubwieser P, Bauer C, Parson W, Unterberger SH, Kuhn V, Pemberger N, Pallua AK, Recheis W, Lackner R, Stalder R, Pallua JD. Post-mortem interval estimation of human skeletal remains by micro-computed tomography, mid-infrared microscopic imaging and energy dispersive X-ray mapping. Anal Methods. 2015 Apr 7;7(7):2917-2927. Epub 2015 Feb 18.
44. Lynch T, Gregson D, Church DL. Species-Level Identification of Actinomyces Isolates Causing Invasive Infections: Multiyear Comparison of Vitek MS (Matrix-Assisted Laser Desorption Ionization-Time of Flight Mass Spectrometry) to Partial Sequencing of the 16S rRNA Gene. J Clin Microbiol. 2016 Mar;54(3):712-7. doi: 10.1128/JCM.02872-15. Epub 2016 Jan 6.
45. Maclaughlin-Black SM, Herd RJ, Willson K, Myers M, West IE. Strontium-90 as an indicator of time since death: a pilot investigation. Forensic Sci Int. 1992 Nov;57(1):51-6.
46. Maile AE, Inoue CG, Barksdale LE, Carter DO. Toward a universal equation to estimate postmortem interval. Forensic Sci Int. 2017 Mar;272:150-153. doi: 10.1016/j.forsciint.2017.01.013. Epub 2017 Jan 18.
47. Marchiafava V, Bonucci E, Ascenzi A. Fungal osteoclasia: a model of dead bone resorption. Calcif Tissue Res. 1974 Mar 29;14(3):195-210.
48. McLaughlin G, Lednev IK. Potential application of Raman spectroscopy for determining burial duration of skeletal remains. Anal Bioanal Chem. 2011 Nov;401(8):2511-8. doi: 10.1007/s00216-011-5338-z. Epub 2011 Aug 26.
49. Mueller B. Gtichtlich Medizin. Springer, Berlin, 1953:70-74.
50. Muller K, Chadefaux C, Thomas N, Reiche I. Microbial attack of archaeological bones versus high concentrations of heavy metals in the burial environment: a case study of animal bones from a medieaval copper workshop in Paris. Palaeo-geogr. Palaeoclimatol. Palaeoecol. 2011 Sep 15;310(1-2):39–51.
51. Nagy G, Lorand T, Patonai Z, Montsko G, Bajnoczky I, Marcsik A, Mark L. Analysis of pathological and non-pathological human skeletal remains by FT-IR spectroscopy. Forensic Sci Int. 2008 Feb 25;175(1):55-60. Epub 2007 Jun 18.
52. Ng LS, Sim JH, Eng LC, Menon S, Tan TY. Comparison of phenotypic methods and matrix-assisted laser desorption ionisation time-of-flight mass spectrometry for the

identification of aero-tolerant Actinomyces spp. isolated from soft-tissue infections. Eur J Clin Microbiol Infect Dis. 2012 Aug;31(8):1749-52. doi: 10.1007/s10096-011-1496-3. Epub 2011 Dec 6.

53. Nielsen-Marsh CM, Smith CI, Jans MME, Nord A, Kars H, Collins MJ. Bone diagenesis in the European Holocene II: taphonomic and environmental considerations, J. Archaeol Sci. 2007 Sep;34(9):1523–31.
54. Peaper DR, Havill NL, Aniskiewicz M, Callan D, Pop O, Towle D, Boyce JM. Pseudo-outbreak of Actinomyces graevenitzii associated with bronchoscopy. J Clin Microbiol. 2015 Jan;53(1):113-7. doi: 10.1128/JCM.02302-14. Epub 2014 Oct 29.
55. Pesquero MD, Ascaso C, Alcalá L, Fernández-Jalvo Y. A new taphonomic bioerosion in a Miocene lakeshore environment. Palaeogeogr. Palaeoclimatol. Palaeoecol. 2010 Sep;295(1-2):192-98.
56. Puccini C. Istituzioni di medicina legale. Casa Editrice Ambrosiana, Milano, 2009: pp. 652-676.
57. Nicholson RA. Bone degradation, burial medium and species representation debunking the myths, an experiment-based approach. J. Archaeol Sci. 1996 Jul;23(4):513-33. doi: 10.1006/jasc.1996.0049.
58. Ramsthaler F, Kreutz K, Zipp K, Verhoff MA. Dating skeletal remains with luminol-chemiluminescence. Validity, intra- and interobserver error. Forensic Sci Int. 2009 May 30;187(1-3):47-50. doi: 10.1016/j.forsciint.2009.02.015. Epub 2009 Mar 25.
59. Rodriguez WC 3rd, Bass WM. Decomposition of buried bodies and methods that may aid in their location. J Forensic Sci. 1985 Jul;30(3):836-52.
60. Rodriguez WC 3rd. Decomposition of Buried and Submerged Bodies. In Forensic Taphonomy: The Postmortem Fate of Human Remains. CRC Press, 1997:459- 67.
61. Roux W. Über eine im Knochen lebende Gruppe von Fadenpilzen (Mycelites ossifragus). Z. wiss. Zool. 1887;45:227–54.
62. Rhine S, Dawson JE. Estimatión of Time Since Death in the Southwestern United States. In K.J. Reichs Forensic Osteology: Advances in the Identification of Human Remains. 2nd ed. Charles C. Thomas Publishing, Springfield, IL, 1998, pp. 145-159.
63. Sabbe LJ, Van De Merwe D, Schouls L, Bergmans A, Vaneechoutte M, Vandamme P. Clinical spectrum of infections due to the newly described Actinomyces species A. turicensis, A. radingae, and A. europaeus. J Clin Microbiol. 1999 Jan;37(1):8-13.
64. Salmon PL, Bondarenko OA, Henshaw DL. Dose210, a semi-empirical model for prediction of organ distribution and radiation doses from long-term exposure to Pb-210 and Po-210. Rad. Prot Dosim. 1999 Apr 1;82(3):175–92. doi.org/10.1093/oxfordjournals.rpd.a032623.
65. Schaffer J. Bemerkungen zur Geschichte der Bohrkanäle in Knochen und Zähnen. Anat. Anz. 1894;10:459–64.

66. Schaffer J. Über den feineren Bau fossiler Knochen. S.-B. Akad. Wiss. Wien, math.-nat. Kl. (III). 1889;98:319–82.
67. Schaffer J. Über Roux'sche Kanäle in menschlichen Zähnen. S.-B. Akad. Wiss. Wien, math.-nat. Kl. (III). 1890;99:146–52.
68. Schott AS, Behr J, Quinn J, Vogel RF. MALDI-TOF Mass Spectrometry Enables a Comprehensive and Fast Analysis of Dynamics and Qualities of Stress Responses of Lactobacillus paracasei subsp. paracasei F19. PLoS One. 2016 Oct 26;11(10):e0165504. doi: 10.1371/journal.pone.0165504. eCollection 2016.
69. Schrag B, Uldin T, Mangin P, Froidevaux P. Dating human skeletal remains using a radiometric method: biogenic versus diagenetic 90Sr and 210Pb in vertebrae. Forensic Sci Int. 2012 Jul 10;220(1-3):271-8. doi: 10.1016/j.forsciint.2012.03.014. Epub 2012 Apr 11.
70. Schrag B, Uldin T, Mangin P, Bochud F, Froidevaux P. Dating human skeletal remains using 90Sr and 210Pb: case studies. Forensic Sci Int. 2014 Jan;234:190.e1-6. doi: 10.1016/j.forsciint.2013.10.038. Epub 2013 Nov 12.
71. Schwarcz HP, Agur K, Jantz LM. A new method for determination of postmortem interval: citrate content of bone. J Forensic Sci. 2010 Nov;55(6):1516-22. doi: 10.1111/j.1556-4029.2010.01511.x.
72. Sledzik PS. Forensic Taphonomy: Postmortem Decomposition and Decay. In K.J. Reichs Forensic Osteology: Advances in the Identification of Human Remains. 2nd ed. Charles C. Thomas Publishing, Springfield, IL, 1998:109-119.
73. Socransky SS, Haffajee AD, Cugini MA, Smith C, Kent RL Jr. Microbial complexes in subgingival plaque. J Clin Periodontol. 1998;25:134-144.
74. Swift B. Dating human skeletal remains: investigating the viability of measuring the equilibrium between 210Po and 210Pb as a means of estimating the post-mortem interval. Forensic Sci Int. 1998 Nov 30;98(1-2):119-26.
75. Trueman CN, Martill DM. The long-term survival of bone: The role of bioerosion. Archaeometry. 2002 Aug;44(3):371-82.
76. Turner-Walker G, Jans MME. Reconstructing taphonomic histories using histological analysis. Palaeogeogr. Palaeoclimatol Palaeoecol. 2008 Sep;266(3-4):227–235. doi.org/10.1016/j.palaeo.2008.03.024.
77. Ubelaker DH, Buchholz BA, Stewart JE. Analysis of artificial radiocarbon in different skeletal and dental tissue types to evaluate date of death. J Forensic Sci. 2006 May;51(3):484-8.
78. Vastel L, Lemercier V, Kerboull L, Kerboull M. Fonctionnement d'une banque de tissus osseux en 1998. Rev Chir Orthop. 1999; 85: 164-173
79. Wade WG. The oral microbiome in health and disease. Pharmacol Res. 2013 Mar;69(1):137-43. doi: 10.1016/j.phrs.2012.11.006. Epub 2012 Nov 28.

80. Wedl C. Über einen im Zahnbein und Knochen keimenden Pilz. S.-B. Akad. Wiss. Wien, math.-nat. Kl. (I). 1864;50:171–93.
81. Whiley RA, Beighton D, Winstanley TG, Fraser HY, Hardie JM. Streptococcus intermedius, Streptococcus constellatus, and Streptococcus anginosus (the Streptococcus milleri group): association with different body sites and clinical infections. J Clin Microbiol. 1992;30:243-244.
82. White L, Booth TJ. The origin of bacteria responsible for bioerosion to the internal bone microstructure: Results from experimentally-deposited pig carcasses. Forensic Sci Int. 2014 Jun;239:92-102. doi: 10.1016/j.forsciint.2014.03.024.
83. Wilson SJ, Christensen AM. A test of the citrate method of PMI estimation from skeletal remains. Forensic Sci Int. 2017 Jan;270:70-75. doi: 10.1016/j.forsciint.2016.11.026. Epub 2016 Nov 24.
84. Woess C, Unterberger SH, Roider C, Ritsch-Marte M, Pemberger N, Cemper-Kiesslich J, Hatzer-Grubwieser P, Parson W, Pallua JD. Assessing various Infrared (IR) microscopic imaging techniques for post-mortem interval evaluation of human skeletal remains. PLoS One. 2017 Mar 23;12(3):e0174552. doi: 10.1371/journal.pone.0174552. eCollection 2017.
85. Yoshino M, Kimijima T, Miyasaka S, Sato H, Seta S. Microscopical study on estimation of time since death in skeletal remains. Forensic Sci Int. 1991 Mar;49(2):143-58.

PAPERS PUBLISHED DURING PhD

International Journal of Biological Macromolecules 107 (2018) 1668–1674

Contents lists available at ScienceDirect

International Journal of Biological Macromolecules

journal homepage: www.elsevier.com/locate/ijbiomac

Review

Not only tendons: The other architecture of collagen fibrils

Mario Raspanti*, Marcella Reguzzoni, Marina Protasoni, Petra Basso

Department of Medicine & Surgery, Insubria University, Varese, Italy

ARTICLE INFO

Article history:
Received 12 July 2017
Received in revised form
29 September 2017
Accepted 6 October 2017
Available online 10 October 2017

Keywords:
Collagen
Fibrillogenesis
Extracellular matrix

ABSTRACT

For many decades the fibrillar collagens have been the subject of a remarkable body of ultrastructural research. The vast majority of the studies, however, were carried out on tendon or on tendon-derived material. For many reasons this reflects an obvious choice but at the same time it also is an unfortunate circumstance, because this flooding of tendon-related data can easily encourage the false confidence that all connective tissues are similar. The reality is quite the opposite, and a different fibrillar structure has been long time observed on collagen fibrils from different tissues, the most notable example being offered by corneal fibrils. The same architecture can be found in a number of disparate tissues and may actually be the prevalent one on a whole-body scale. Although these fibrils diverge from those of tendon in their architecture, size, D-period, composition, cross-linking and fibrillogenesis mechanism, their structure was the subject of rather sparse ultrastructural studies and even today their mere existence is often overlooked or ignored. This paper summarizes the main aspects of the structural biology of these forgotten fibrils.

Contents

1. Introduction: a collagen primer

The collagen represent one of the most ancient protein families, being present in all the Metazoa and tracing its lineage up to protein motifs in choanoflagellates [1,2]. In mammalians we recognize about thirty genetically defined types identified with Roman numbers and which, as whole, represent more than one third of all proteins of the body. The hallmark of all collagens is the repeated basic structure $(Gly\text{-}Xaa\text{-}Yaa)_n$, where the residues designated as Xaa and Yaa can be any amino acid but are frequently represented by proline. All collagens have a quaternary structure, each functional molecule being composed of three distinct polypeptide chains (the so-called alpha-chains). In addition, collagens also have a highly complex supramolecular structure where molecules interact with each other at different hierarchical levels in order to form a variety of higher-order structures, including fibrils, microfibrils and felt-like sheets.

A few collagen types, defined fibrillar collagens, have an uninterrupted sequence of about 300 Gly-Xaa-Yaa triplets, flanked by shorter globular domains. Other collagen types have more or less interrupted sequences and are classified as fibril-associated collagens with interrupted triple helices (FACITs), membrane-associated collagens with interrupted triple helices (MACITs),

* Corresponding author at: Laboratory of Human Morphology, Dept. of Medicine and Surgery, Insubria University, Via Monte Generoso 71, 21100 Varese, Italy.
E-mail address: mario.raspanti@uninsubria.it (M. Raspanti).

https://doi.org/10.1016/j.ijbiomac.2017.10.037
0141-8130/

multiple triple-helix domains and interruptions (MULTIPLEXINs), microfibrillar collagens, etc. [3].

In this context we will deal exclusively with the main fibrillar collagens, i.e. the biochemical types I, II, III, V and XI. Collagen types XXIV and XXVII have recently joined the fibrillar collagens, but their role is still less defined [4]. The types II and III are homopolymers, each of them composed of three identical chains respectively named α1(II) and α1(III), while the type I is a heteropolymer made of two identical αI(I) chains and an α2(I). Collagen type V is also a heteropolymer made of three different chains, α1(V), α2(V) and α3(V), mixed in different, tissue-dependent combinations. The type XI seems to be, from a phylogenetical viewpoint, a more recent protein: it is closely related to the type V to the point that the α2(V) chain may replace the α2(XI) chain in some tissues, and the α3(XI) chain seems to be an alternative splicing of the α1(II) gene. All the genes coding for the fibrillar collagens are highly interrupted, being made of dozens of exons, and apparently descend from a common ancestor formed by 45 or 54 nucleotides, precisely a string of five or six triplets of the form Gly-Xaa-Yaa, coding for a short 15- or 18-residue chain. This ancient gene seems to have subsequently originate by successive duplications and mutations the actual library of large, highly interrupted genes, whose exons still betray the 45- or 54-base motif.

Although the primary structure of the α-chains is known, a word of caution is necessary since all collagens undergo massive post-translational modifications so that the correspondence between nucleotides and amino acid is far from granted. In particular the hydroxylation of proline residues to 4-hydroxyproline (or, less commonly, 3-hydroxyproline) is critical to the correct folding of the α-chains and therefore to the structure and function of collagen [5]. Another post-translational modification essential for the maturation of collagen is the oxidation of some lysine and hydroxylysine residues into an aldehyde group, which subsequently react with other lysine of hydroxylysine residues to form insoluble cross-links. Some hydroxylysine residues are glycosylated by specific enzymes into galactosyl- or glucosyl-galactosyl-hydroxylysine. Other non-enzymatic glycosylation processes [6] lead to the slow formation of advanced glycation end-products (AGE).

The central $(Gly\text{-}X\text{-}Y)_n$ domain of the collagen α-chains folds into a tight, left-handed helix with an average axial residue-to-residue spacing of about 0.286 nm and an angular separation of 108°, values which can vary slightly according to the size and shape of the different amino acids [7]. This coiling is largely due to steric repulsion between proline residues in the X position and 4-hydroxyprolines in Y-position, and is therefore highly dependent on the post-translational hydroxylation of proline. The peptide bonds form the backbone of the helix, leaving the side chains of amino acids exposed on the outside [8]. Since there are about three residues per turn and since every third residue of this domain is a glycine residue, on the surface of the helix appears a row of (almost) superimposed glycine residues. Since the glycine has no side chain (represented by a single hydrogen atom), this glycine row ultimately appears as a 'clean' line slowly spiraling along the molecule in a slightly right-handed helix with a pitch of approx. 8.58 nm.

This glycine line makes possible the aggregation of three chains into a right-handed triple helix, with all the glycine residues buried inside the structure and the side chains of all other residues exposed on the outside, where they are responsible of the intermolecular interactions. It is worth mentioning the reciprocal stabilizing effect of left-handed threads wound into a right-handed rope.

Although the collagen family consists of approximately 30 distinct types, the term "collagen" without other specifications is often used in reference to collagen type I, which is also the most extensively studied. Here the formation of the triple helix is directed by the carboxy-terminal globular domain (C-propeptide) and proceeds along the C → N direction [9]. Critically, this depends on the lack of steric hindrances in the glycine rows along the central axis. A point mutation can be tolerated in the X and Y position, but the substitution of a glycine in the third position with any other residue stops the formation of the triple helix and results in defective molecules. The clinical outcome is some form of Osteogenesis Imperfecta.

Normally the process leads to the formation of a long, somewhat flexible rod-like molecule 1.5 nm wide and over 300 nm long, topped at both ends by globular domains. In this form, also defined procollagen, the molecule is complete.

This is the starting point for the formation of supramolecular aggregates.

2. The formation of fibrils

In the extracellular space (or maybe intracellularly [10]) the terminal globular domains are cleaved by specific enzymes leaving only two small non-helical fragments (the telopeptides), which fold compactly along the helical portion. In this form the collagen molecule is essentially insoluble and begins to aggregate even at nanomolar concentrations. At this stage the intermolecular interactions are inherently labile, i.e. hydrophilic-hydrophobic or electrostatic; a careful analysis of the amino acid sequence reveals the superposition of several patterns and motifs coexisting along the molecule [11] that may be enough to direct an ordered layout in supramolecular aggregates [12]. In collagen type I the distribution of some amino acids (Lysine, Glutamine and Arginine) shows a periodicity of 18 residues, which reflects the length of the exons, while the distribution of polar and of hydrophobic residues shows a periodic repeat of 234 residues. The presence of other molecules (ATP, polyanions, cations, other collagen types etc.) can modify the balance of these labile interactions and thus promote one aggregation form rather than another, even without taking part of the final structure. This way a whole range of supramolecular aggregates, finite or periodic, symmetrical or asymmetrical, can appear [13–17].

The longitudinal distribution of polar and hydrophobic residues normally directs a lateral intermolecular interaction with an axial stagger of approximately 234 amino acid residues, i.e. about 67 nm, or an integer multiple of this measure. Since this measure is not an integral divider of the molecule length, after four repeats a short interval remains between the end of each molecule and the beginning of the next one [18]. This interaction pattern directly translates into a periodic structure with a period of 67 nm (the D-period), divided into an 'overlap' zone and a 'gap' zone, whose 5:4 mass ratio has subsequently found extensive experimental confirmation.

Other fibrillar collagens can co-precipitate to form mixed fibrils, but not all combinations are allowed. Collagens I, III and V are reciprocally miscible and form mixed fibrils present in all fibrous connective tissues, where type I seems always to be preeminent while types III and V appear in widely variable amounts in different tissues. The types II and XI are not miscible with other fibrillar collagens but co-form mixed fibrils typical of cartilage, together with collagen type IX and perhaps other FACITs.

Cartilage fibrils have been shown to have an epitaxial structure with an axial core including four collagen XI and ten collagen II molecules [19], surrounded by type II molecules and eventually by surface-bound type IX. Considering the similitude between type V and type XI it seems not implausible that type V collagen have a similar nucleating role in the formation of mixed fibrils with types I and/or type III [20–25]. Undoubtedly type V and I coform mixed fibrils *in vitro* whose diameter is somewhat proportional to the type I/type V ratio [20,26,27], and it has been suggested that type V has some nucleating/initiating role [24,25], but the same can be said of type III [28]. It has also been reported that fibrillogenesis *in vivo* is

altered or absent at all if type V is not present [29,30], but *in vitro* the process must have a different dynamics since it takes place anyway.

In general the fibril formation is obtained by warming and neutralizing an acidic collagen solution, and its progression can be evaluated by turbidimetry. This technique evidences an initial lag phase, followed by a steep increase which finally ends with a plateau once all the molecules are exhausted. This is consistent with a cooperative mechanism involving successive aggregation steps. More sophisticated techniques reveal a more complex picture: if the collagen solution is warmed before neutralization the process yields slender banded fibrils similar to those found in embryonic tissues, while if the solution is first neutralized then warmed it yields tiny unbanded filaments which successively coalesce into mature fibrils.

3. Different by size

As we said, the vast majority of the ultrastructural studies were carried out on tendon or, in vitro, on tendon-derived material. This flooding of tendon-related data can encourage a false confidence that all connective tissues are the same. The reality is quite the opposite, and *in vivo* a sharp dichotomy has been long time observed across different tissues.

Tissues from the locomotor system (i.e. tendons, bone, and some ligaments) and a few other tensile tissues such as the sclera show large and heterogeneous fibrils, with diameters ranging from a few nanometers to 300 nm or more, with a polymodal distribution of the diameters [31]. In these fibrils the molecules are arranged into supertwisted right-handed microfibrils running almost longitudinally and interdigitating with the neighboring ones [32], a complex architecture consistent at the same time with the microfibrillar aspect observed with electron- and atomic force microscopy and with the quasi-crystalline hexagonal packing reported by diffraction studies. In this paper these fibrils, mainly found in tendons, ligaments and bone, will not be discussed any further.

All the other connective tissues, including sources as diverse as tendon sheath, nerve sheath, interstitial stroma, arterial wall and cornea, exhibit fibrils with a smaller and extremely uniform diameter [31]. The average diameter of these fibrils can vary from tissue to tissue, from the 35 nm of cornea to the 110 nm of some nerve sheaths, yet it remains extremely uniform in any given location. In some cases, as in the endotenon sheaths, these fibrils can be in physical contact with the tendon fascicles but they always remain distinct and are immediately recognizable.

4. Different by layout

As a general rule, collagen fibrils in the locomotor system and in some connective tissues such as the sclera are subject to high tensile stresses and are laid out in compact patterns, where they tend to maintain a straight course compatible with their limited flexibility. An emblematic case is represented by tendon fibrils, that are essentially made of straight segments connected by planar crimps [33]. In the Haversian systems of compact bone the fibrils run parallel in compact layers, that can be arranged at an angle with each other in the familiar criss-cross pattern described in histology textbooks or superimposed with a steady, progressive change of direction to form a twisted plywood [34]. This is a distinctive architecture very efficient from a functional viewpoint and is often observed also in other unrelated contexts [35].

Where these fibrils run among multiple holes, as in the lamina cribrosa of the sclera and the optic nerve head, they form a dense intricate meshwork [36,37] where they run tangential to the holes while typically maintaining a straight course. This is an efficient setup to contrast circumferential expansion and to resist the tension exerted by the intraocular pressure.

By contrast the small uniform fibrils of sheaths, blood vessels wall, dermis and interstitial stroma are usually gathered in loose, flexible fascicles following a wavy course with no visible crimps. These fascicles can reversibly accommodate very large deformations and in some cases they can be straightened out to twice their resting length. A notable exception is represented by the corneal stroma, whose small uniform fibrils are kept in register by a unique and distinctive proteoglycan milieu.

5. Different by composition

In the years when these differences were becoming evident, the biochemical characterization of the different collagen types was also slowly emerging. The demonstration of collagen type III only in thin, uniform fibrils led to the hypothesis that type I collagen formed the thick multimodal fibrils of tendon, while the uniform fibrils of cornea, blood vessels etc. were made of type III [38]. This was not correct, but neither was entirely wrong: now we know that types I, III and V can coexist in the same fibril, where they can cross-link together [39], and that in all tissues the collagen I is always the prevalent type, while types III and V represent just a variable fraction. Yet in vitro the average fibril diameter, as well as the diameters distribution, shows substantial differences among pure type I collagen and mixtures of types I, III and V, and *in vivo* the average diameter is inversely proportional to the volume fraction of type V [20,26,27]. Instead of being made of collagen type III (as is still found in some histology textbooks) the small uniform fibrils seem now to contain sizable proportions of types III and V in addition to the fundamental type I. The fibrils of tendon, bones etc. remain made only of type I.

It is still questionable whether the types I, III and V are uniformly distributed in the mixed fibrils or not. The earlier research, reporting that the type V can be evidenced only in cut or crushed fibrils, suggested that it is present only in the fibril interior [23,40]. Because of the variable composition of type V it is possible that heterotrimer molecules have different interactions (and locations) than homotrimer ones [41].

6. Different by D-period

Although the exact value of the cross-banding varies slightly depending from the technique used, the tendon fibrils have a D-period of or near 67 nm. The uniform fibrils from nerve sheath (and tendon sheath, and cornea, etc.) by contrast have a shorter D-period of approximately 64 nm. A comparative analysis carried out by TEM, which can locate with high accuracy the position of sub-bands along the D-period, and by X-ray diffraction [42] revealed a perfect correspondence: all the features of the D-period were present, only proportionally and uniformly shortened. In other words the molecules are the same, but their axial length is proportionally compressed.

7. Different by architecture

A spiral layout of filamentous subunits within the collagen fibril was observed as early as 1949 [43]. At that time, however, the electron microscopy was in its infancy and other ultrastructural techniques didn't exist yet, so it was only much later that a few techniques, including freeze-fracture and, more recently, atomic force microscopy were able to yield high resolution pictures able to take further these observations [44–48]. The large and heterogeneous fibrils from tendon showed an almost parallel layout of the microfibrils (Figs. 1 and 3), slowly winding at such a shallow angle

Fig. 1. Freeze-fractured, fully hydrated rat tail tendon. The picture spans 1 μ × 1 μ. The longitudinal course of the microfibrils is clearly visible.

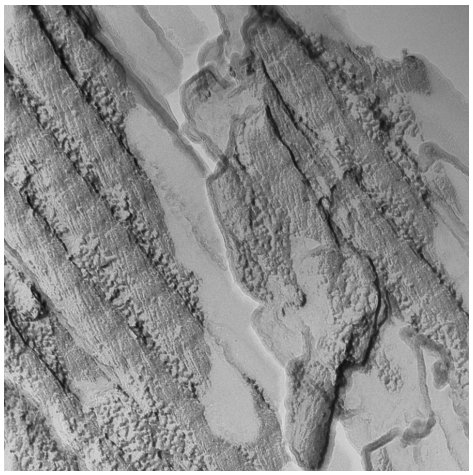

Fig. 2. Freeze-fractured fibrils from rat corneo-scleral limbus, same magnification. The microfibrils wind helically at approx. 17° to the fibril axis.

as to make its measurement difficult: they are often described as lying less than 5° to the fibril axis.

By contrast the small uniform fibrils, imaged with the same techniques (Figs. 2 and 4), showed microfibrils winding helically at approx. 17–18° to the fibril axis, again with slight variations depending from the technical approach [46–49]. This value explains the reduction of the axial period reported above: since the molecules are tilted with respect to the fibril axis, their axial projection (and that of all their parts) is uniformly shortened according to the cosine of the winding angle. The D-period, more precisely, is shortened to 64 nm, or 67 nm × cos(17°). It is – to say the least – surprising to find recent papers that still struggle to explain the D-period reduction [50].

Please note that for a clear D-period to appear it is not enough that the molecules maintain an appropriate reciprocal stagger, but it is also necessary that all the molecules project the same length along the fibril axis. This can be achieved in two ways.

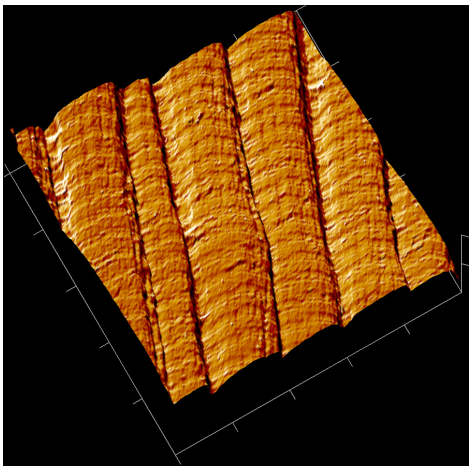

Fig. 3. Rat tail tendon imaged by fluid tapping-mode atomic force microscopy. This technique, together with the freeze-fracture, is the only one able to obtain high resolution pictures of hydrated, unprocessed tissue. The viewfield spans 1 μ × 1 μ.

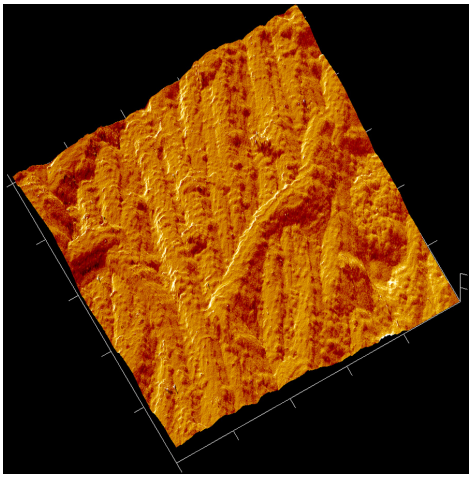

Fig. 4. Unfixed, untreated collagen fibrils of human aortic wall imaged by fluid tapping-mode atomic force microscopy, 1 μ × 1 μ. Compare this picture with Fig. 2.

The *constant pitch/variable angle* model is more intuitive and, although never formalized in writing, it was silently taken for granted for some time. This architecture can be imagined as a bundle of initially parallel filaments that is subsequently twisted until the outermost threads reach a 17° angle to the axis. Here we have however, a critical flaw: the outermost threads will project an axial length of 64 nm but those lying in the neutral position along the axis, being still straight, will project their full 67 nm length. The filaments in intermediate positions winding at intermediate angles will project intermediate lengths. It is therefore evident that this layout would be incompatible with the appearance of a D-banding. To overcome this deficiency it is necessary to suppose that the innermost molecules are axially compressed, their compression being balanced by a corresponding stretching of the outermost ones. It is unclear how all this compression and stretching can be viable from a thermodynamical viewpoint.

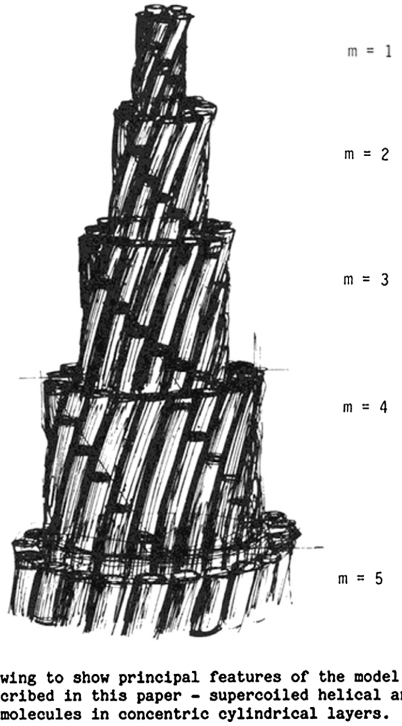

Fig. 5. The first hypothesis of the inner architecture of the constant-angle collagen fibrils as found in cornea and in the sheaths of nerves and tendons, from Galloway [51].

The only attractive feature of the variable angle model is that the 17° observed on the fibril surface could be envisioned as a limiting value that the molecules are unable to exceed and that, once reached, terminates the fibril accretion. This hypothesis would elegantly explain the diameter uniformity observed in these fibrils within a given tissue but, once again, would leave unexplained the difference in diameter measured in different tissues. In addition, such a molecular arrangement of almost-parallel threads would set a helical splitting plane along the fibril, a thing that was never observed in freeze-fractured specimens.

An alternative *constant angle/variable pitch* model was first proposed by John Woodhead-Galloway [51] (Fig. 5). Unfortunately it was published in a monography chapter of limited diffusion, so a very similar model was independently proposed a few years later [49]. In this architecture the fibril is made of distinct coaxial layers of sub-fibrils, which in each layer are helically wound to 17° around the fibril axis (Fig. 6). This way the threads describe a whole turn around the fibril in a length, or *pitch*, = $2\pi R \times \mathrm{cotg}(17^\circ)$, i.e. approximately $20.55 \times R$, dependent from the distance R from the fibril axis. Since each layer has a different pitch, each microfibril along its length comes to interact with different microfibrils of the neighboring layers, making these fibrils more resilient to deformation. It is possible, although still hypothetical, that individual molecules can extend from a microfibril to another, as in tendons [32]. Moreover, since all the threads wind at the same angle they all project the same axial length, automatically satisfying the basic requirement for the appearance of the D-banding. Although somewhat counter-intuitive, this model is consistent with the concentric features observed by other authors [52,53] and it satisfies all the requirements without requiring unexplained external factors, in contrast with the former one which requires hypothetical external compressive or tensile forces and an equally hypothetical variable gradient across the fibril radius. Experimental evidence was not available at the time, but the latter model seemed preferable on the basis of the Occam's razor: *entia non sunt multiplicanda praeter necessitatem*.

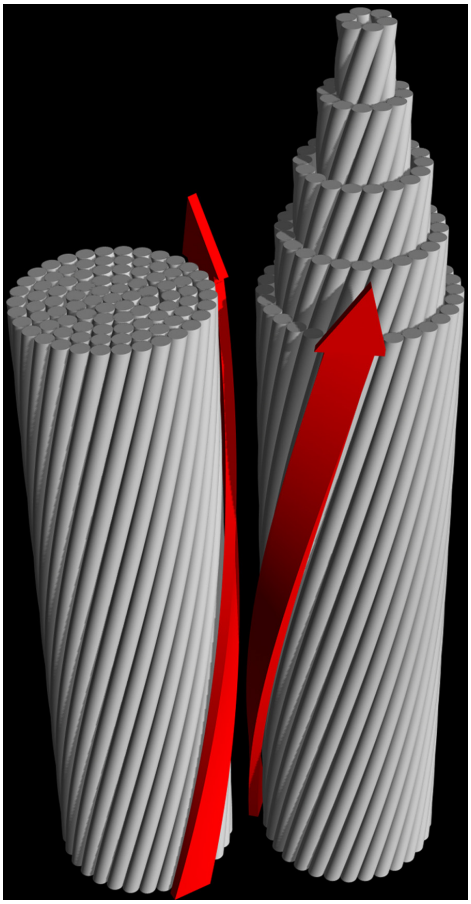

Fig. 6. 3D model of fibrils with helical microfibrils. The rightmost fibril exhibits the innermost layers of microfibrils, not unlike the layers of molecules in Fig. 5. Together, the two fibrils demonstrate that identically wound microfibrils actually run in different directions along the contact line, preventing any lateral fusion of the protofibrils.

An unequivocal evidence remained impossible to obtain until 2001, when the constant angle model was experimentally demonstrated by TEM microtomography of corneal fibrils [54,55], whose microfibrils appeared uniformly winding with the same angle to the fibril axis.

8. Different by cross-linking

As the fibrils mature, the collagen molecules become part of a network of stable cross-links through the lysine or hydroxylysine residues. The reaction is initiated by the copper metalloenzyme lysil oxydase, which converts the ε-amino group of certain lysyl

or hydroxylysyl residues to an aldehyde. This can then react with another aldehyde to form an aldol condensation product, or with unmodified lysine or hydroxylysine residue to form hydroxylysinonorleucine (HLNL) or dihydroxylysinonorleucine (DHLNL) respectively. All these bifunctional reducible crosslinks can then maturate into tri- or tetrafunctional nonreducible crosslinks [56].

In addition to these, in the small, uniform fibrils of skin and cornea HLNL reacts with a histidine to form histidino-HLNL (formerly known as hydroxyaldolhistidine). This involves an histidine residue that is offset from the lysine residues and that it is only accessible if adjoining molecules are slanted by 17° [57,58]. Not surprisingly this cross-link was never detected in tendon and bone.

9. Different by formation

The mechanism of fibrillogenesis has been mostly studied *in vitro* or, again, in embryonic tendons. It is generally agreed that the fibrils formation takes place in a multistage, cooperative process. At first, collagen molecules group into small clusters (protofibrils) that subsequently coalesce into fibrils [see [10] and [59]]. Since the molecules are essentially straight and parallel, when protofibrils (or even small fibrils) come into contact they can simply flow into each other. The process repeats itself up to the formation of mature fibrils, which can therefore grow not only by addition of individual molecules but also by fusion with other aggregates.

A few details remain to be elucidated: first of all, the factor(s) that terminate the fibril accretion, preventing the fibrils from coalescing into a single massive aggregate. Several causes have been hypothesized, including the persistence of propeptides, the binding of small proteoglycans, the intervention of FACITs, etc., or a combination of these [24]. Small leucine-rich proteoglycans (SLRPs) in particular are advocated by a conspicuous body of experimental evidence.

It is noteworthy, however, that all this holds true only if the molecules within the protofibrils run straight and parallel. If the collagen molecules wind helically the protofibrils cannot possibly merge: not only because the molecules in the contact area are pointing in different directions (Fig. 6), but also because each protofibril has its own radial structure and its own axis: their fusion into a single fibril would require a complete unwinding and rewinding, a thing clearly made implausible by thermodynamic considerations. In other words, these fibrils cannot grow by addition of protofibrils but only by addition of molecules [60,61].

This has two significant implications. First, the existing literature on fibrillogenesis does not apply to these fibrils. Second, the impossibility of a stochastic fusion of protofibrils can suffice to explain the remarkable uniformity of these fibrils: when the fibrillogenesis begins, each nucleation center competes with its neighbors for the available molecules until all these have been depleted. Since the environment is the same for all forming fibrils, they all end up of a similar size without the intervention of any external factor. This is not unlike what happens, e.g., in the formation of snowflakes. Again, we see at work the simplest possible solution.

Even so, a crucial detail is still missing: what causes the molecules to wind helically rather than lying side-by-side?

In the constant angle/variable pitch model confirmed by experimental evidence the molecules describe a full turn around the fibril axis in a length $L \approx 20.55 \times R$, implying that those molecules closer to the fibril axis, where R is close to zero, should wind in an implausibly tight spiral. The only alternative is the existence along the fibril axis of a distinct central structure, and hollow, tube-like fibrils with an electron-lucent core have been observed by TEM in invertebrates and in cyclostomes [62–64]. More recently a small central feature, positive to polysaccharide reactions, has been demonstrated by TEM and AFM in mammals, in fibrils of tendon sheath and nerve sheath but not in tendon fibrils [65]. The constancy with which this core is visible in each and every fibril of a transected bundle suggests that it remains present over the whole length of each fibril. It is hypothetical but not implausible that this structure governs the layout of the adjoining collagen molecules, and that these in turn impose a similar inclination to the molecules that subsequently join the growing fibril. The nature of this core is not known except that it is positive for polysaccharides, but it is noteworthy that collagen V is much more glycosylated than other types, that type V seems to be present only in the fibrils interior, and that type V has been already reported as an initiator/nucleator of fibrillogenesis.

On the basis of the experience so far accumulated on fibrillogenesis *in vivo* and *in vitro*, it would seem reasonable to hypothesize that the (almost) parallel layout of molecules and microfibrils observed in tendons and bone as a sort of default architecture, which takes place unless some other unknown key factor determines the onset of the helical layout.

A major issue of this concept is that fibrils with helical microfibrils were never obtained in vitro. Even soluble collagen extracted from 64 nm “helical” fibrils and reaggregated in vitro forms 67 nm “straight” fibrils [66,67]. Evidently this hypothetical key factor gets lost or remains inactive *in vitro*.

Fibrillogenesis in vitro is evidently different than in vivo: even tendon fibrils, made of straight and parallel molecules of type I collagen, reportedly require the presence of collagen types III and V as initiators or nucleators *in vivo*, while *in vitro* they form equally well, irrespective of their presence or absence. It is important to remember that the aggregation of collagen molecules is very sensitive to the presence of external modulating factors such as polyanions, ATP or other molecules which do not even remain to make part of the final product. The nature and action of the unknown factor which cause the onset of one or the other architecture remains to be elucidated by further research.

Acknowledgement

P.B. is a PhD student of the “Biotechnology, Biosciences and Surgical Technology” course at the Insubria University, Varese, Italy.

References

[1] N. King, M.J. Westbrook, S.L. Young, A. Kuo, M. Abedin, J. Chapman, S. Fairclough, U. Hellsten, Y. Isogai, I. Letunic, M. Marr, D. Pincus, N. Putnam, A. Rokas, K.J. Wright, R. Zuzow, W. Dirks, M. Good, D. Goodstein, D. Lemons, W. Li, J.B. Lyons, A. Morris, S. Nichols, D.J. Richter, A. Salamov, J.G. Sequencing, P. Bork, W.A. Lim, G. Manning, W.T. Miller, W. McGinnis, H. Shapiro, R. Tjian, I.V. Grigoriev, D. Rokhsar, The genome of the choanoflagellate Monosiga brevicollis and the origin of metazoans, Nature 451 (2008) 783–788.
[2] J.-Y. Exposito, C. Cluzel, R. Garrone, C. Lethias, Evolution of collagens, Anat. Rec. 268 (2002) 302–316.
[3] M.D. Shoulders, R.T. Raines, Collagen structure and stability, Annu. Rev. Biochem. 78 (2009) 929–958.
[4] D.A. Plumb, V. Dhir, A. Mironov, L. Ferrara, R. Poulsom, K.E. Kadler, D.J. Thornton, M.D. Briggs, R.P. Boot-Handford, Collagen XXVII is developmentally regulated and forms thin fibrillar structures distinct from those of classical vertebrate fibrillar collagens, J. Biol. Chem. 282 (2007) 12791–12795.
[5] J. Bella, D.J. Hulmes, Fibrillar collagens, Subcell. Biochem. 82 (2017) 457–490.
[6] K.M. Reiser, M.A. Amigable, J.A. Last, Nonenzymatic glycation of type I collagen. The effects of aging on preferential glycation sites, J. Biol. Chem. 267 (1992) 24207–24216.
[7] G.J. Cameron, D.E. Cairns, T.J. Wess, The variability in type I collagen helical pitch is reflected in the D periodic fibrillar structure, J. Mol. Biol. 372 (2007) 1097–1107.
[8] E.Y. Jones, A. Miller, Analysis of structural design features in collagen, J. Mol. Biol. 218 (1991) 209–219.
[9] J. Engel, D.J. Prockop, The zipper-like folding of collagen triple helices and the effects of mutations that disrupt the zipper, Annu. Rev. Biophys. Biophys. Chem. 20 (1991) 137–152.
[10] C.C. Banos, A.H. Thomas, C.K. Kuo, Collagen fibrillogenesis in tendon development: current models and regulation of fibril assembly, Birth Defects Res. Part C 84 (2008) 228–244.

[11] D.G. Arques, J.-P. Fallot, C.J. Michel, Identification of several types of periodicities in the collagens and their simulation, Int. J. Biol. Macromol. 19 (1996) 131–138.
[12] N. Kuznetsova, S. Leikin, Does the triple helical domain of type I collagen encode molecular recognition and fiber assembly while telopeptides serve as catalytic domains? Effect of proteolytic cleavage on fibrillogenesis and on collagen–collagen interactions in fibers, J. Biol. Chem. 274 (1999) 36083–36088.
[13] J.A. Chapman, D.J.S. Hulmes, Electron microscopy of the collagen fibril, in: A. Ruggeri, P. Motta (Eds.), Ultrastructure of the Connective Tissue Matrix, Martinus Nijhoff, The Hague, 1984, pp. 1–33.
[14] R. Mallinger, W. Kulnig, P. Böck, Symmetrically banded collagen fibrils: observations on a new cross striation pattern in vivo, Anat. Rec. 232 (1992) 45–51.
[15] M.F. Paige, J.K. Rainey, M.C. Goh, Fibrous long spacing collagen ultrastructure elucidated by atomic force microscopy, Biophys. J. 74 (1998) 3211–3216.
[16] J.K. Rainey, C.K. Wen, M.C. Goh, Hierarchical assembly and the onset of banding in fibrous long spacing collagen revealed by atomic force microscopy, Matrix Biol. 21 (2002) 647–650.
[17] R.W. Loo, J.B. Goh, C.C. Cheng, N. Su, M.C. Goh, In vitro synthesis of native, fibrous long spacing and segmental long spacing collagen, J. Vis. Exp. 67 (2012) e4417.
[18] A.J. Hodge, J.A. Petruska, Recent studies with the electron microscope on ordered aggregates of the tropocollagen macromolecule, in: G.N. Ramachandran (Ed.), Aspects of Protein Structure, Academic Press, London and New York, 1963, pp. 289–300.
[19] D.F. Holmes, K.E. Kadler, The 10+4 microfibril structure of thin cartilage fibrils, PNAS 103 (2006) 17249–17254.
[20] D.E. Birk, J.M. Fitch, J.P. Babiarz, K.J. Doane, T.F. Linsenmayer, Collagen fibrillogenesis in vitro: interaction of types I and V collagen regulates fibril diameter, J. Cell Sci. 95 (1990) 649–657.
[21] K.E. Kypreos, D. Birk, V. Trinkaus-Randall, D.J. Hartmann, G.E. Sonenshein, Type V collagen regulates the assembly of collagen fibrils in cultures of bovine vascular smooth muscle cells, J. Cell. Biochem. 80 (2000) 146–155.
[22] R.J. Wenstrup, J.B. Florer, E.W. Brunskill, S.M. Bell, I. Chervoneva, D.E. Birk, Type V collagen controls the initiation of collagen fibril assembly, J. Biol. Chem. 279 (2004) 53331–53337.
[23] J. White, J.A. Werkmeister, J.A. Ramshaw, D.E. Birk, Organization of fibrillar collagen in the human and bovine cornea: collagen types V and III, Connect. Tissue Res. 36 (1997) 165–174.
[24] K.E. Kadler, A. Hill, E.G. Canty-Laird, Collagen fibrillogenesis: fibronectin, integrins, and minor collagens as organizers and nucleators, Curr. Opin. Cell Biol. 20 (2008) 495–501.
[25] R.J. Wenstrup, S.M. Smith, J.B. Florer, G. Zhang, D.P. Beason, R.E. Seegmiller, L.J. Soslowsky, D.E. Birk, Regulation of collagen fibril nucleation and initial fibril assembly involves coordinate interactions with collagens V and XI in developing tendon, J. Biol. Chem. 286 (2011) 20455–20465.
[26] E. Adachi, T. Hayashi, In vitro formation of hybrid fibrils of type V collagen and type I collagen. Limited growth of type I collagen into thick fibrils by type V collagen, Connect. Tissue Res. 14 (1986) 257–266.
[27] T.F. Linsenmayer, E. Gibney, F. Igoe, M.K. Gordon, J.M. Fitch, L.I. Fesler, D.E. Birk, Type V collagen: molecular structure and fibrillar organization of the chicken α1(V)-NH2 terminal domain, a putative regulator of corneal fibrillogenesis, J. Cell Biol. 121 (1993) 1181–1189.
[28] K. Stuart, A. Panitch, Characterization of gels composed of blends of collagen I, collagen III, and chondroitin sulfate, Biomacromolecules 10 (2009) 25–31.
[29] R.J. Wenstrup, J.B. Florer, W.G. Cole, M.C. Willing, D.E. Birk, Reduced type I collagen utilization: a pathogenic mechanism in COL5A1 haplo-insufficient Ehlers-Danlos syndrome, J. Cell. Biochem. 92 (2004) 113–124.
[30] M. Sun, S. Chen, S.M. Adams, J.B. Florer, H. Liu, W.W.Y. Kao, R.J. Wenstrup, D.E. Birk, Collagen V is a dominant regulator of collagen fibrillogenesis: dysfunctional regulation of structure and function in a corneal-stroma-specific Col5a1-null mouse model, J. Cell Sci. 124 (2011) 4096–4105.
[31] D.A.D. Parry, A.S. Craig, Growth and development of collagen fibril, in: tissue. connective, A. In: Ruggeri, P. Motta (Eds.), Ultrastructure of the Connective Tissue Matrix, Martinus Nijhoff, The Hague, 1984, pp. 34–64.
[32] J.P.R.O. Orgel, T.C. Irving, A. Miller, T.J. Wess, Microfibrillar structure of type I collagen in situ, PNAS 24 (2006) 9001–9005.
[33] M. Raspanti, A. Manelli, M. Franchi, A. Ruggeri, The 3D structure of crimps in the rat Achilles tendon, Matrix Biol. 24 (2005) 503–507.
[34] M.M. Giraud-Guille, Twisted plywood architecture of collagen fibrils in human compact bone osteons, Calcif. Tissue Res. 42 (1988) 167–180.
[35] B. Satiat-Jeunemaitre, Spatial and temporal regulations in helicoidal extracellular matrices: comparison between plant and animal systems, Tissue Cell 24 (1992) 315–334.
[36] A.R. Elkington, C.B. Inman, P.V. Steart, R.O. Weller, The structure of the lamina cribrosa of the human eye: an immunocytochemical and electron microscopical study, Eye (Lond.) 4 (1990) 42–57.
[37] T. Oyama, H. Abe, T. Ushiki, The connective tissue and glial framework in the optic nerve head of the normal human eye: light and scanning electron microscopic studies, Arch. Histol. Cytol. 69 (2006) 341–356.
[38] E. Reale, F. Benazzo, A. Ruggeri, Differences in the microfibrillar arrangement of collagen fibrils. Distribution and possible significance, J. Submicrosc. Cytol. 13 (1981) 135–143.
[39] W. Henkel, R.W. Glanville, Covalent crosslinking between molecules of type I and type III collagen, Eur. J. Biochem. 122 (1982) 205–213.
[40] F. Ruggiero, C. Burillon, R. Garrone, Human corneal fibrillogenesis. Collagen V structural analysis and fibrillar assembly by stromal fibroblasts in culture, Invest. Ophth. Vis. Sci. 37 (1996) 1749–1760.
[41] H. Chanut-Delalande, A. Fichard, S. Bernocco, R. Garrone, D.J.S. Hulmes, F. Ruggiero, Control of heterotypic fibril formation by collagen V is determined by chain stoichiometry, J. Biol. Chem. 276 (2001) 24352–24359.
[42] M. Marchini, M. Morocutti, A. Ruggeri, M.H.J. Koch, A. Bigi, N. Roveri, Differences in the fibril structure of corneal and tendon collagen. An electron microscopy and X-ray diffraction investigation, Connect. Tissue Res. 15 (1986) 269–281.
[43] R.W.G. Wickoff, Electron Microscopy Technique and Applications, Interscience, New York, 1949, pp. 203.
[44] R. Reed, M.J. Wood, M.K. Keech, Helical nature of the collagen fibril, Nature 177 (1956) 697–699.
[45] M. Bouteille, D.C. Pease, The tridimensional structure of native collagenous fibrils: their proteinaceous filaments, J. Ultrastruct. Res. 35 (1971) 314–338.
[46] J.H. Lillie, D.K. MacCallum, L.J. Scaletta, J.C. Occhino, Collagen structure: evidence for a helical organization of the collagen fibril, J. Ultrastruct. Res. 58 (1977) 134–143.
[47] A. Ruggeri, F. Benazzo, E. Reale, Collagen fibrils with straight and helicoidal microfibrils: a freeze-fracture and thin section study, J. Ultrastruct. Res. 68 (1979) 101–108.
[48] S. Yamamoto, H. Hashizume, J. Hitomi, M. Shigeno, S. Sawaguchi, H. Abe, T. Ushiki, The subfibrillar arrangement of corneal and scleral collagen fibrils as revealed by scanning electron and atomic force microscopy, Arch. Histol. Cytol. 63 (2002) 127–135.
[49] M. Raspanti, V. Ottani, A. Ruggeri, Different architectures of the collagen fibril: morphological aspects and functional implications, Int. J. Biol. Macromol. 11 (1989) 367–371.
[50] M. Jastrzebska, D. Tarnawska, R. Wrzalik, A. Chrobak, M. Grelowski, E. Wylegala, D. Zygadlo, A. Ratuszna, New insight into the shortening of the collagen fibril D-period in human cornea, J. Biomol. Struct. Dyn. 8 (2016) 1–13.
[51] J. Galloway, Structure of collagen fibrils, in: A. Bairati, R. Garrone (Eds.), Biology of Invertebrate and Lower Vertebrate Collagens, Plenum Press, New York, 1985, pp. 73–82.
[52] D.J.S. Hulmes, T.J. Wess, D.J. Prockop, P. Fratzl, Radial packing, order, and disorder in collagen fibrils, Biophys. J. 68 (1995) 1661–1670.
[53] D.J.S. Hulmes, Building collagen molecules, fibrils, and suprafibrillar structures, J. Struct. Biol. 137 (2002) 2–10.
[54] D.F. Holmes, C.J. Gilpin, C. Baldock, U. Ziese, A.J. Koster, K.E. Kadler, Corneal collagen fibril structure in three dimensions: structural insights into fibril assembly, mechanical properties, and tissue organization, Proc. Natl. Acad. Sci. U. S. A. 98 (2001) 7307–7312.
[55] C. Baldock, C.J. Gilpin, A.J. Koster, U. Ziese, K.E. Kadler, C.M. Kielty, D.F. Holmes, Three-dimensional reconstruction of extracellular matrix polymers using automated electron tomography, J. Struct. Biol. 138 (2002) 130–136.
[56] M. Yamauchi, M. Sricholpech, Lysine post-translational modifications of collagen, Essays Biochem. 52 (2012) 113–133.
[57] G.L. Mechanic, E.P. Katz, M. Henmi, C. Noyes, M. Yamauchi, Locus of a Histidine-based, stable trifunctional, helix to helix collagen cross-link: stereospecific structure of type I skin fibrils, Biochemistry 26 (1987) 3500–3509.
[58] M. Yamauchi, G.S. Chandler, H. Tanzawa, E.P. Katz, Cross-linking and the molecular packing of corneal collagen, Biochem. Bioph. Res. Co. 219 (1996) 311–315.
[59] T. Sawada, S. Inoue, Ultrastructure of irregular collagen fibrils of shark mandible, Acta Zool.-Stockholm. 92 (2011) 62–66.
[60] M. Raspanti, Different architectures of collagen fibrils enforce different fibrillogenesis mechanisms, J. Biomed. Sci. Eng. 3 (2010) 1169–1174.
[61] M. Raspanti, Supramolecular assembly of type I collagen, in: N. Karamanos (Ed.), Extracellular Matrix: Pathobiology and Signalling, De Gruyter, Berlin, 2012, pp. 562–574.
[62] A. Bairati, Collagen: an analysis of phylogenetic aspects, Boll. Zool. 39 (1972) 205–248.
[63] S. Franc, Collagen of coelenterates, in: A. Bairati, R. Garrone (Eds.), Biology of Invertebrate and Lower Vertebrate Collagens, Plenum Press, New York, 1985, pp. 197–210.
[64] G. Tettamanti, A. Grimaldi, T. Congiu, G. Perletti, M. Raspanti, R. Valvassori, M. de Eguileor, Collagen reorganization in leech wound healing, Biol. Cell. 97 (2005) 557–568.
[65] M. Raspanti, M. Reguzzoni, M. Protasoni, D. Martini, Evidence of a discrete axial structure in unimodal collagen fibrils, Biomacromolecules 12 (2011) 4344–4347.
[66] B. Brodsky, E.F. Eikenberry, K. Cassidy, An unusual collagen periodicity in skin, Biochim. Biophys. Acta 621 (1980) 162–166.
[67] L.J. Gathercole, J.S. Shah, C. Nave, Skin-tendon differences in collagen D-period are not geometric or stretch-related artifacts, Int. J. Biol. Macromol. 9 (1987) 181–183.

EJO
ISSN 1120-6721

Eur J Ophthalmol 2017; 27 (6): 762-768
DOI: 10.5301/ejo.5000982

ORIGINAL RESEARCH ARTICLE

Multilayer microstructure of idiopathic epiretinal macular membranes

Claudio Azzolini[1], Terenzio Congiu[1], Simone Donati[1], Alberto Passi[1], Petra Basso[1], Eliana Piantanida[1], Cesare Mariotti[2], Francesco Testa[3], Simona M. Caprani[1], Jennifer Cattaneo[1], Riccardo Vinciguerra[1]

[1] Department of Medicine and Surgery, University of Insubria, Varese - Italy
[2] Department of Ophthalmology, Polytechnic University of Ancona, Ancona - Italy
[3] Eye Clinic, Multidisciplinary Department of Medical, Surgical and Dental Sciences, Second University of Naples, Naples - Italy

ABSTRACT

Purpose: To identify the ultramicroscopic structure of idiopathic epiretinal macular membranes (iEMMs) by scanning electron microscopy (SEM).

Methods: We examined 28 iEMMs surgically removed from 28 eyes of 28 patients. All specimens, previously observed at stereomicroscope, were treated with an osmium maceration technique. Fine resolution of iEMMs' 3D architecture and their interaction with the retina were studied using a Philips SEM-FEG XL-30 microscope.

Results: The specimens appeared as laminar connective structures partially or completely adherent to the inner limiting membrane (ILM). We identified 4 types of structures: (1) distinct layers of thin sheets of woven fibers; (2) folded layers of inhomogeneous thickness of fibrous material more consistent; (3) thicker and more rigid layers recognizable as collagen fibrils with typical 64-nm period, collagen fibrils isolated or intermingled between them; (4) lacunar structures with inflammatory and/or necrotic material. The first 3 types of structures appear to thicken towards a centripetal direction from the ILM to the vitreous in order from 1 to 3. The interface of ILM-iEMM tissue shows particular small bridges of connection. Cells are rarely found, especially in the tissue near the ILM.

Conclusions: Layers of various materials follow one another in iEMMs. Cells are rarely found. The interface ILM-iEMM tissue shows particular small bridges of connection. The dynamic modeling of bended layers begins in soft tissue.

Keywords: Collagen, Epiretinal membrane, Gliosis, Scanning electron microscopy

Introduction

First described in 1865, idiopathic epiretinal macular membrane (iEMM), also called macular pucker, premacular gliosis, and cellophane maculopathy, is caused by the ingrowth of an opaque, ipocellular, and avascular tissue on the macular surface. It has a tendency to develop traction and contraction of the underlined retina. Its prevalence is estimated at 2% in patients younger than 60 years and 12% in those older than 70 years (1-3).

It was postulated that retinal glial cells might migrate into the vitreous underlying holes of the inner limiting membrane (ILM), never demonstrated, followed by proliferative stimulus of intercellular protein. Secondary migration of fibrous astrocytes, further cell proliferation, and new collagen production contribute to the rigidity and contraction of the iEMM. The contraction is transmitted to the adjacent retina tissue. Another theory is that an anomalous posterior vitreous detachment allows the persistence of vitreous fibers and hyalocytes on ILM, giving a scaffold for proliferation of glial cells and hyalocytes. Hyalocytes may also stimulate Müller cells to send processes through an intact ILM, giving rise to a scaffold for other cells. The signaling transition, another theory, presumes that many specific proteins like basic fibroblast growth factor, glial cell line-derived neurotrophic factor (GFRα1, GFRα2, Ret), and vascular endothelial growth factor (VEGF) in aqueous and vitreous body induce membrane development pathway, activation, and cell adhesion through molecules like fibrinogen A, cytokines, growth factor, and platelet-derived growth factor-A. Transdifferentiation from glial cells to myofibroblasts is induced by molecules like NGF and tumor growth factor-β (4-14).

Scanning electron microscopy (SEM) could be useful in understanding membrane architecture and mechanism of formation of pathologic iEMMs, as well as in helping to improve pharmacologic or surgical therapy.

Accepted: April 6, 2017
Published online: May 19, 2017

Corresponding author:
Claudio Azzolini, MD
Department of Medicine and Surgery
University of Insubria
Via Guicciardini 9
Varese, Italy
claudio.azzolini@uninsubria.it

Methods

In this prospective interventional study, a consecutive case series of 28 eyes of 28 patients (16 men and 12 women), mean age at the time of surgery 63.5 years (range 45-78), were included. All patients complained of reduced vision and metamorphopsia associated with a diagnosis of an iEMM. Exclusion criteria were any type of previous laser, intravitreal injection, or surgical treatment, vascular retinopathy, previous inflammatory or traumatic eye diseases, and significant media opacities that precluded a good fundus examination or optical coherence tomography (OCT) imaging. Four iEMM specimens of the initial 32 patients were lost because their smallness hampered the SEM study; they were therefore excluded from the study. All patients signed written informed consent before inclusion in the study, including consent for surgery.

Patients' demographic data and parametric statistics are summarized in Table I. The study was conducted in accordance with the tenets of the Declaration of Helsinki.

All patients underwent 3-port pars plana vitrectomy by 23-G to 25-G sutureless technique (Millennium-Stellaris, Bausch & Lomb, Rochester, NY). A central vitrectomy was performed to create a tunnel to reach the posterior pole. The iEMM was engaged and then peeled from the nerve fiber layer, usually by intraocular forceps. In all cases, during surgery, the iEMM specimen was immediately placed on 4% buffered paraformaldehyde (Fig. 1) for a subsequent optic microscope (OM) and SEM study. Complete removal of all residual epiretinal tissues, as well as residual stained ILM (Blue Peel, Geuder, Germany), was then performed in all patients. Light fiber optic beam was maintained focused in the fovea the minimum time needed, reducing the light intensity as much as possible (15). After surgery, patients were examined at baseline and postoperatively at days 30, 90, and 180.

During each examination, complete ophthalmologic and functional outcomes were assessed with best-corrected visual acuity in logMAR and Amsler grid. Retinal quantitative and qualitative evaluation was performed by means of 3D-OCT Topcon 2000 (Topcon, Tokyo, Japan). Foveal central thickness was measured using high-resolution topography map automated protocol.

All the specimens of iEMMs have been previously observed at stereo OP in order to evaluate their consistence and thickness; then they were prepared for SEM study. To obtain a fine resolution of the 3D architecture of the iEMM, we used an improved protocol based on osmium maceration: this technique allows us to better define cells and stromal structure of soft tissues (16). The specimens were fixed with 2% glutaraldehyde in 0.1 M Na-cacodylate buffer (pH 7.2) for 1 hour at room temperature. After washes in cacodylate buffer, specimens were cut with a razor blade and postfixed in a solution of 1% osmium tetroxide, 1.25% potassium ferrocyanide for 1 hour, washed in phosphate-buffered saline (pH 7.2), dehydrated in an increasing series of ethanol, and finally dried in hexamethyldisilazane. Dried iEMM samples were mounted on aluminum stubs, gold coated with an Emitech K550 sputter coater, and then observed with an SEM-FEG XL-30 microscope (Philips, Eindhoven, the Netherlands). Only 2 specimens, fixed as above, were embedded in Epon, sliced in semi-thin sections, and colored in toluidine blue in order to confirm the stratification of iEMM.

Liquid chromatography electrospray-tandem mass spectrometry was used to identify the protein content in 3 iEMMs (cases 25, 26, and 27). The proteins in specimen underwent reduction, alkylation, and protease digestion (17). Mass spectrometry was performed using a LTQ Orbitrap Velos (Thermo Fisher Scientific, Waltham, MA) equipped with a nanospray source and Xcalibur 2.0 and Tune 2.4 as software (Thermo Fisher Scientific). Database searching was performed using the SEQUEST and MASCOT algorithms in Proteome

TABLE I - Patients' clinical characteristics

Patient/ sex/age, y	Preop OCT CRT, µm	iEMM layers appearance at SEM	Letters gained at month 1	Letters gained at month 6
1/F/68	320	a	5	15
2/M/71	360	b	0	5
3/M/56	360	a	5	20
4/F/65	395	b	5	15
5/F/78	410	b	0	10
6/M/63	325	a	5	10
7/M/72	390	b	10	20
8/M/45	410	b	10	15
9/M/69	400	c	10	15
10/F/68	390	b	15	15
11/M/59	395	b	10	20
12/F/60	410	b	10	15
13/M/68	405	b	10	10
14/M/69	290	a	0	0
15/F/58	385	c	0	5
16/F/49	370	c	0	0
17/M/58	390	b	0	5
18/M/48	385	b	5	10
19/M/66	295	b	5	5
20/F/68	400	b	5	15
21/M/59	390	b	0	10
22/F/48	285	b	10	10
23/F/72	280	c	15	20
24/F/69	285	c	15	15
25/M/48	385	b	0	5
26/M/79	360	b	5	5
27/M/69	290	b	0	5
28/M/76	305	b	5	10

The specimens were first observed with a stereomicroscope at 10x-40x. After this examination, we attributed a class justified by ultrastructural SEM data, according to the appearance of iEMM layers: (a) soft splay tissue, (b) soft splay folded and fibrotic folded tissue, and (c) soft splay folded tissue.
CRT = central retinal thickness; iEMM = idiopathic epiretinal macular membrane; OCT = optical coherence tomography; SEM = scanning electron microscope.

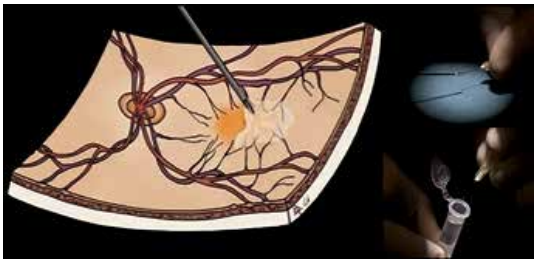

Fig. 1 - Idiopathic epiretinal macular membrane removal and bend specimen immediately placed in 4% buffered paraformaldehyde.

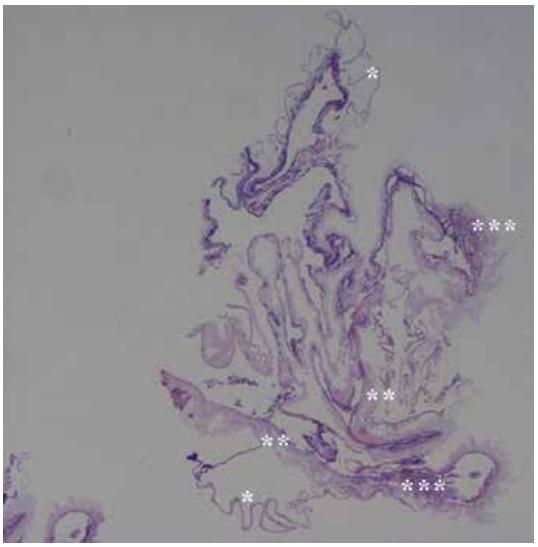

Fig. 2 - Semi-thin section stained with toluidina, 10×. The idiopathic epiretinal macular membrane appears folded back on itself. Well evident different density of tissue layers. *Inner limiting membrane; **soft tissue; ***thick tissue.

Discoverer 1.1 software (Thermo Fisher Scientific) against the human Uniprot/SwissProt and NCBInr sequence database, respectively (17, 18).

Results

The removed iEMMs, especially the thicker ones, appeared folded in on themselves and hardly to unbend immediately after collection. At stereo OP, the iEMM appeared with a stratified feature. The specimens appeared as laminar connective structures partially or completely adherent to the ILM (Fig. 2). Four cases presented only soft splay layers, 5 only soft folded layers, and 19 presented dense and thick fibrotic layers folded over the soft ones (Tab. I). The semi-thin sections highlight the diversity in thickness and density of the laminae. This aspect suggested cutting the full-thickness sample for subsequent analysis by SEM conducted as a dissection from the ILM to the layers on the side of the vitreous.

At SEM, in the outermost layer of the iEMMs, the ILM is well recognizable, remaining adherent to the sample as a smooth and thin layer with a compact texture. Through any tears in the ILM, the interface between this and the first fibrous layer affixed by the side of the vitreous body is visible (Fig. 3, A and B). This first layer is made irregular by dense microexpansions that can be interpreted as a junction system with ILM (Fig. 3C). The following layers, always affixed in the direction of the vitreous body, were made by thin sheets of corrugated loosely intertwined fibrils, like a gauze (Fig. 3D).

In the middle layer of the IEMM, the weaving fibrils become denser and even thin sheets have a more rigid shape (Fig. 4A). These layers are arranged in different directions and begin to show consistent folds (Fig. 4B). At higher magnification, collagen fibrils appear, detaching from the layer surface and running crosswise to the folds and connecting them (Fig. 4, C and D).

The layers on the side of vitreous body are clearly thicker and more rigid and the folds also are densely structured. On the surface of these layers and in continuity with the texture of the foil are visible bundles of collagen fibrils showing the typical 64-nm period (dried) (Fig. 5A) that gives rise to nests of collagen fibrils (Fig. 5B) and large and solid collagen fibers (Fig. 5C). These fibers are clearly interpretable as elements of rigidity of the layer. The more solid samples, just at the layers closest to the vitreous, showed an additional thickening due both to an increased deposition of the fibrous material and to the layers folding on themselves (Fig. 5D). Sometimes these thick layers can form wide folds, closed at the base.

Between the iEMM layers, more frequently in the intermediate layers, it is possible to observe flattened cells with protrusions taking close relationship with the collagen fibrils, typical of fibroblasts (Fig. 6A and B), and surprisingly small nests of cocci in case 12 (Fig. 6C and D).

Mass spectrometry analysis of the 3 IEMMs showed the presence of several proteins. Vimentin, laminin, and perlecan, a heparansulphate proteoglycan, are the main proteins identified.

Discussion

Idiopathic epiretinal macular membrane specimens taken during surgery evidenced at SEM 4 types of structures from the ILM to the vitreous: (1) thin sheets of woven fibers, with the sheets creating distinct layers (Fig. 3); (2) folded layers of inhomogeneous thickness of fibrous material more consistent (Fig. 4); (3) thicker and more rigid layers in some cases recognizable as collagen fibrils with typical 64-nm period (dried). Collagen fibrils are isolated or intermingled between them, giving rise to dense bundles of collagen fibers (Figs. 4 and 5); and (4) lacunar structures with inflammatory and/or necrotic material. The first 3 types of structures seem to evolve as a thickening towards a centripetal direction from the ILM to the vitreous. In this context, cells are rarely found, especially in tissue near the ILM and tissue near the vitreous. Cells are fibroblast-like (Fig. 6) among spaces of more soft tissue.

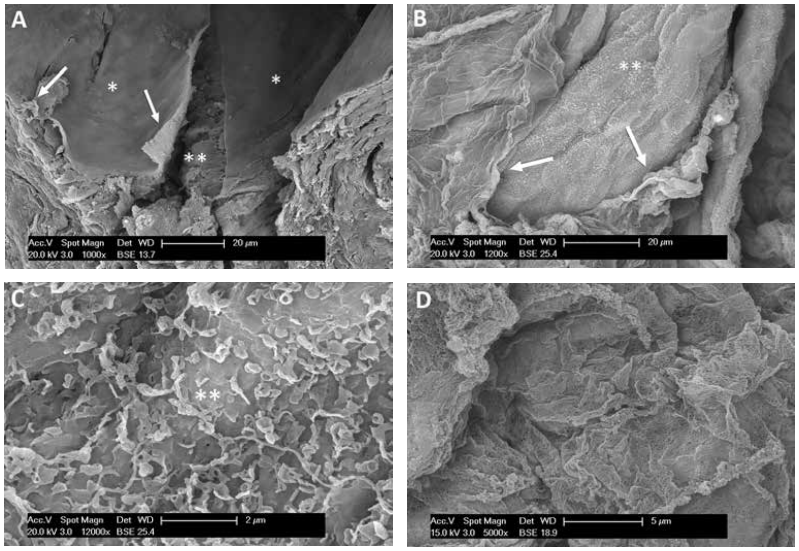

Fig. 3 - Scanning electron microscope specimens showing the outer layers of idiopathic epiretinal macular membrane (iEMM). Centripetal direction from the inner limiting membrane (ILM) toward the vitreous body: (**A**) retina side of ILM: this layer is partially torn but still adherent: the turned tearing edges of ILM suggest a mechanical action; (**B**) through the tear of ILM: the first layer of iEMM displaying a grid with microfolds of connection is visible; (**C**) the higher magnification of the contact surface ILM-iEMM highlights the dense contact placations; (**D**) layered interior of iEMM: the structure appears formed by thin layers of fibrous material. The weaving loose allows the formation of openings. *Retina side of ILM; **first iEMM layer; arrows: turned edges of ILM.

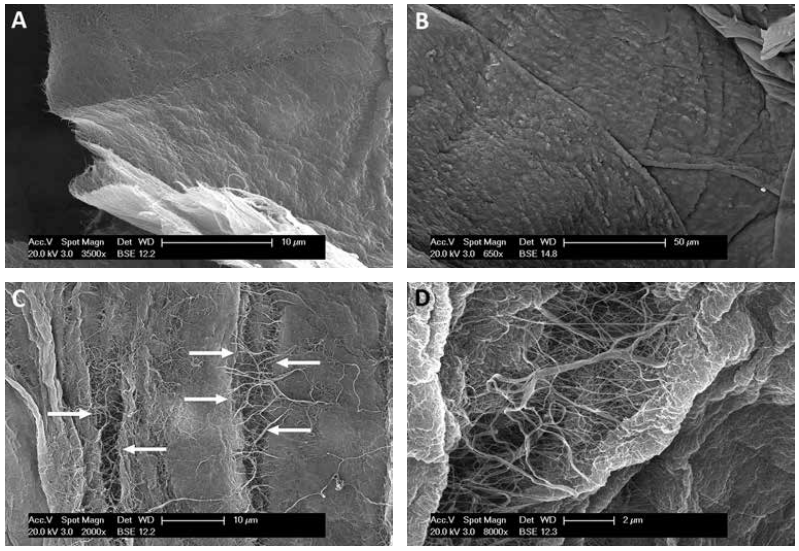

Fig. 4 - Scanning electron microscope specimens of intermediate layers of idiopathic epiretinal macular membrane. (**A**) Layer thickness is still thin but the texture is more dense than the outer layers; (**B**) multiple leaves superimposed and arranged in various directions: the leaves are thicker and appear more rigid, nevertheless they begin to show the folds; (**C**) fibrous layer shaped in parallel folds: note the collagen fibrils begin transversely between the adjacent folds; (**D**) at higher magnification, the detail of the single fibrils shows their organization in fibers. Arrows: collagen fibrils.

These observations suggest that the iEMM formation is initially formed by thin sheet of soft tissue over the ILM and then evolving in collagen fibrils giving rise to strong collagen fibers and dense tissue. The texture begins in the intermediate layer, becoming denser to form thick layers closest to the vitreous body. The inner layers in contact with the vitreous body show the structural folds of the mature iEMM, responsible for coarctation of the underlying tissue and inevitable retinal folds.

The interface between the ILM and the newly formed epiretinal tissue shows particular small bridges of connection (Fig. 3C). Those bridges of connection and vitreomacular adhesion represent the first step of an iEMM and could be also the initial glue between posterior hyaloid and ILM in other diseases such as vitreomacular traction and macular hole (8, 19). Those bridges of connection are probably the target of enzymatic vitreolysis (20-24).

The ILM is not always found on the retinal side of the specimens and this is another proof that the majority of ILM, but not the entire ILM, is surgically removed together with the iEMM, as already reported (8, 25, 26). Inner limiting membrane holes

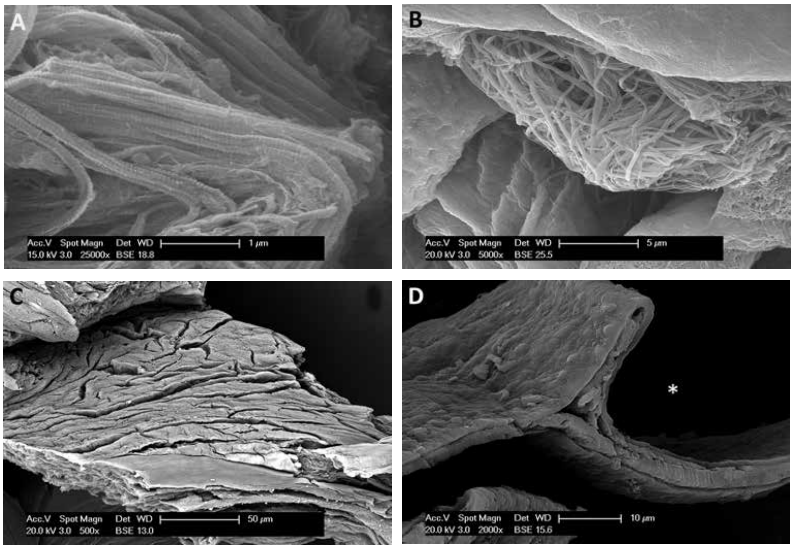

Fig. 5 - Scanning electron microscope specimens of inner layer of idiopathic epiretinal macular membrane (iEMM). (**A**) Fibrils with the typical 64-nm period (dried) appear continuous with the fibers of the epiretinal membrane layer; (**B**) tangle of collagen fibrils; (**C**) the collagen fibers formed by packages of collagen fibrils give rise to thick layers densely folded up in the part closest to the vitreous body; (**D**) section in full thickness with thick layers of iEMM bended in structural folds. *Vitreous Cavity.

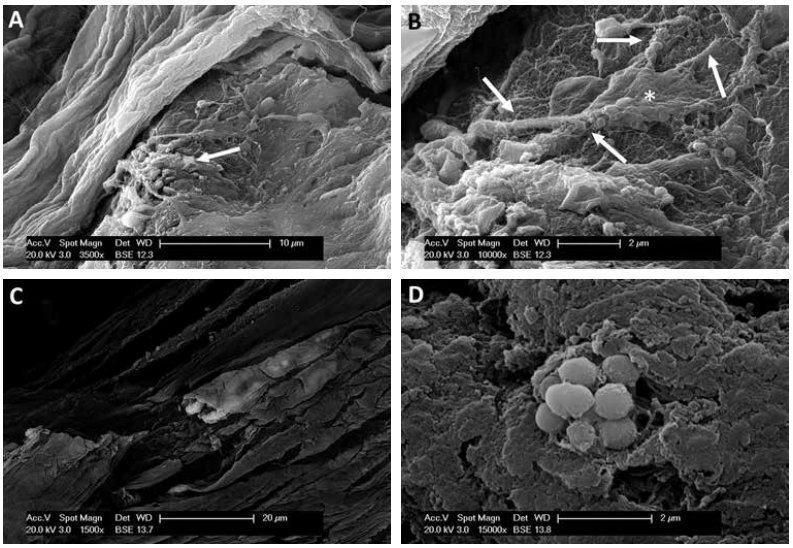

Fig. 6 - (**A**) Fibroblasts between the layers (arrow); (**B**) *fibroblast: at major enlargement the typical expansions of cells (arrows) and the close relationship with the fibers are clearly visible; (**C**, **D**) roundish formation compatible for shape and dimension to small nests of cocci, localized within the layer, emerging through natural apertures.

found on the specimen are secondary to the mechanical stripping during surgery or histologic study, as suggested by the reversed edge of the ILM (Fig. 3A). We never found in ILM holes with unreversed edge; this fact supports the hypothesis of a non direct migration of cells from the retina (4).

The use of mass spectrum analysis gave the opportunity to identify at protein level the structures described in microscopy in 3 cases. Vimentin, laminin, and perlecan identified in specimens are components of the basal membrane with pivotal role in retinal disease (27). Vimentin and perlecan can create fibrillar complex and are usually found in the basal membrane, more frequently in microvascular pathologies. Perlecan is of particular interest, as it is linked to many processes of neovascularization through a fragment thereof of endorepellina that antagonizes the pathway of VEGF and VEGFR, playing a role in retinal pathologies, probably in avascular iEMM tissue development. Perlocan, vimentin, and laminin conversely are related to a mechanical injury to the retina (28).

Surprisingly, we found some cocci bacteria in one case in the intermediate layer of iEMM. The fact that bacteria are

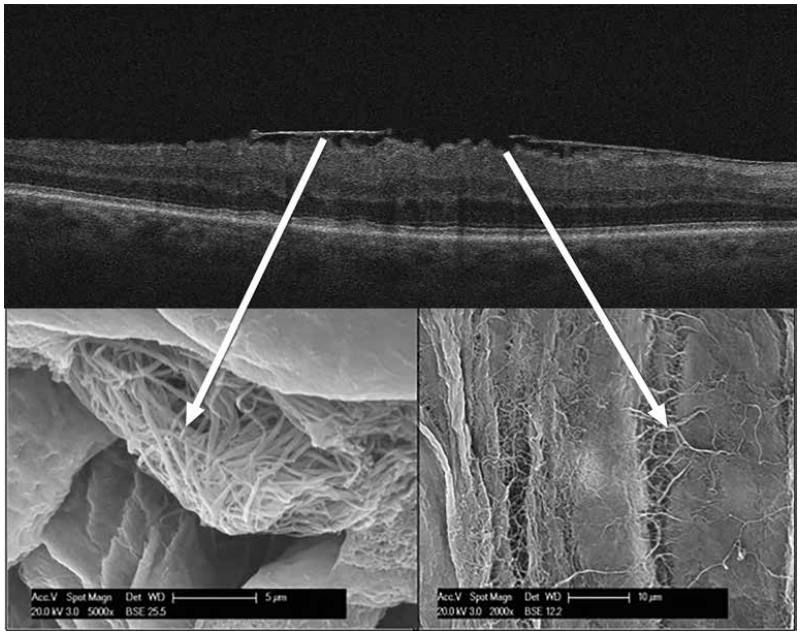

Fig. 7 - Hyperreflective optical coherence tomography (OCT) epiretinal layers may represent more dense fibrous tissue (left arrow), while hyporeflective OCT epiretinal layers may represent soft intermediate tissue (right arrow).

in the context of tissue gathered together in little nests excluded contamination; furthermore, this would be almost impossible as all specimens were immediately placed on 4% buffered paraformaldehyde after surgery.

The fact that OCT scans are centered on the fovea while SEM study is performed on the entire iEMM does not allow having a perfect correspondence between OCT and SEM images. We presume that more dense tissue gives rise to stronger OCT reflectivity (Fig. 7). We presume also that the decrease of visual acuity could be secondary to folded layers of inhomogeneous soft fibrous material (cases 1, 3, 6, and 14), not necessarily very consistent, which bend the inner retina. The improvement of visual acuity after surgery takes months, as already described (29-31), and in our case series gained visual acuities after surgery were found also after peeling of soft splay tissue. The surgeon must remove all tissue adherents to the retina.

Multiple abnormalities of the vitreomacular interface coming from macrofolds, microfolds, and hyperreflective microstructures found before iEMM surgery by adaptive optic images (32-34) could be related to the different structures found by SEM in our study.

Limitations of our study are the necessary widening maneuvers of the bended iEMMs as soon as possible after the sampling with possible artefacts. However, SEM observations are similar in all specimens, thus representing the reality of the structure of an iEMM.

In conclusion, layers of different structures are subsequently present in iEMM. Cells migrate gradually towards the vitreous side of the iEMM. Dynamic modeling of bended layers begins in soft tissue. The lack of unreversed ILM edge holes suggests that ILM holes are not involved in the pathogenesis of iEMMs. Visual acuity worsening is probably not always caused by IEMMs formed by dense tissue, but also by iEMMs formed by folded soft tissue that is not always easily visible by OCT. During surgery, the surgeon should remove all tissue adherent to the retina. The presence of proteins related to a mechanical injury to the retina confirms the hypothesis of the role of posterior vitreous traction in the development of iEMMs.

Disclosures

Financial support: No financial support was received for this submission.
Conflict of interest: None of the authors has conflict of interest with this submission.

References

1. Mitchell P, Smith W, Chey T, Wang JJ, Chang A. Prevalence and associations of epiretinal membranes. The Blue Mountains Eye Study, Australia. Ophthalmology. 1997;104(6):1033-1040.
2. Chan R, Collin HB. Epiretinal membrane with macular pucker. Clin Exp Optom. 2000;83(4):222-225.
3. Sandali O, El Sanharawi M, Basli E, et al. Epiretinal membrane recurrence: incidence, characteristics, evolution, and preventive and risk factors. Retina. 2013;33(10):2032-2038.
4. Kampik A. Pathology of epiretinal membrane, idiopathic macular hole, and vitreomacular traction syndrome. Retina. 2012;32(Suppl 2):S194-S198, discussion S198-S199.
5. Sebag J. Anomalous posterior vitreous detachment: a unifying concept in vitreo-retinal disease. Graefes Arch Clin Exp Ophthalmol. 2004;242(8):690-698.

6. Govetto A, Lalane RA III, Sarraf D, Figueroa MS, Hubschman JP. Insights into epiretinal membranes: presence of ectopic inner foveal layers and a new optical coherence tomography staging scheme. Am J Ophthalmol. 2017;175:99-113.
7. Joshi M, Agrawal S, Christoforidis JB. Inflammatory mechanisms of idiopathic epiretinal membrane formation. Mediators Inflamm. 2013;2013:192582.
8. Zhao F, Gandorfer A, Haritoglou C, et al. Epiretinal cell proliferation in macular pucker and vitreomacular traction syndrome: analysis of flat-mounted internal limiting membrane specimens. Retina. 2013;33(1):77-88.
9. Pollreisz A, Funk M, Breitwieser FP, et al. Quantitative proteomics of aqueous and vitreous fluid from patients with idiopathic epiretinal membranes. Exp Eye Res. 2013;108:48.58.
10. Mandal N, Kofod M, Vorum H, et al. Proteomic analysis of human vitreous associated with idiopathic epiretinal membrane. Acta Ophthalmol. 2013;91(4):e333-e334.
11. Iannetti L, Accorinti M, Malagola R, et al. Role of the intravitreal growth factors in the pathogenesis of idiopathic epiretinal membrane. Invest Ophthalmol Vis Sci. 2011;52(8):5786-5789.
12. Schumann RG, Eibl KH, Zhao F, et al. Immunocytochemical and ultrastructural evidence of glial cells and hyalocytes in internal limiting membrane specimens of idiopathic macular holes. Invest Ophthalmol Vis Sci. 2011;52(11):7822-7834.
13. Emami-Naeini P, Kumar Singh P, Boss JD, et al. Vitreous biomarkers in idiophatic epiretinal membrane. Invest Ophthalmol Vis Sci. ARVO Congress 2016. Abstract C0097.
14. Frisina R, Zampedri E, Zampedri E, et al. Microscopic study of surgically exised vitreoretinal membranes. Invest Ophthalmol Vis Sci. ARVO Congress 2016. Abstract C0038.
15. Azzolini C, Brancato R, Venturi G, Bandello F, Pece A, Santoro P. Updating on intraoperative light-induced retinal injury. Int Ophthalmol. 1994-1995;18(5):269-276.
16. Congiu T, Radice R, Raspanti M, Reguzzoni M. The 3D structure of the human urinary bladder mucosa: a scanning electron microscopy study. J Submicrosc Cytol Pathol. 2004;36(1):45-53.
17. Fontana L, Rovina D, Novielli C, et al. Suggestive evidence on the involvement of polypyrimidine-tract binding protein in regulating alternative splicing of MAP/microtubule affinity-regulating kinase 4 in glioma. Cancer Lett. 2015;359(1):87-96.
18. Bradford MM. A rapid and sensitive method for the quantitation of microgram quantities of protein utilizing the principle of protein-dye binding. Anal Biochem. 1976;72:248-254.
19. Duker JS, Kaiser PK, Binder S, et al. The International Vitreomacular Traction Study Group classification of vitreomacular adhesion, traction, and macular hole. Ophthalmology. 2013;120(12):2611-2619.
20. Stalmans P, Benz MS, Gandorfer A, et al. MIVI-TRUST Study Group. Enzymatic vitreolysis with ocriplasmin for vitreomacular traction and macular holes. N Engl J Med. 2012;367(7): 606-615.
21. Haller JA, Stalmans P, Benz MS, et al. MIVI-TRUST Study Group. Efficacy of intravitreal ocriplasmin for treatment of vitreomacular adhesion: subgroup analyses from two randomized trials. Ophthalmology. 2015;122(1):117-122.
22. Azzolini C, D'Angelo A, Maestranzi G, et al. Intrasurgical plasmin enzyme in diabetic macular edema. Am J Ophthalmol. 2004;138(4):560-566.
23. Sebag J. The emerging role of pharmacologic vitreolysis. Retinal Physician. 2010;7(2):52-56.
24. Sebag J. Pharmacologic vitreolysis. In: Sebag J, Editor. Vitreous in health and disease, 2014; chapter VI. A. New York: Springer.
25. Gandorfer A, Haritoglou C, Scheler R, Schumann R, Zhao F, Kampik A. Residual cellular proliferation on the internal limiting membrane in macular pucker surgery. Retina. 2012;32(3): 477-485.
26. Carpentier C, Zanolli M, Wu L, et al. Pan-American Collaborative Retina Study Group. Residual internal limiting membrane after epiretinal membrane peeling: results of the Pan-American Collaborative Retina Study Group. Retina. 2013;33(10):2026-2031.
27. Langford-Smith A, Keenan TD, Clark SJ, Bishop PN, Day AJ. The role of complement in age-related macular degeneration: heparan sulphate, a ZIP code for complement factor H? J Innate Immun. 2014;6(4):407-416.
28. Lewis GP, Fisher SK. Up-regulation of glial fibrillary acidic protein in response to retinal injury: its potential role in glial remodeling and a comparison to vimentin expression. Int Rev Cytol. 2003;230:263-290.
29. Donati S, Caprani SM, Semeraro F, et al. Morphological and functional retinal assessment in epiretinal membrane surgery. Semin Ophthalmol. 2016;10:1-8.
30. Song SJ, Kuriyan AE, Smiddy WE. Results and prognostic factors for visual improvement after pars plana vitrectomy for idiopathic epiretinal membrane. Retina. 2015;35(5):866-872.
31. García-Fernández M, Castro Navarro J, González Castaño C, García Alonso A, Fonollá Gil M. Epiretinal membrane surgery: anatomic and functional outcomes. Arch Soc Esp Oftalmol. 2013;88(4):139-144.
32. Lombardo M, Scarinci F, Giannini D, et al. High resolution multimodal imaging after idiopathic epiretinal membrane surgery. Retina. 2016;36(1):171-180.
33. Lombardo M, Scarinci F, Ripandelli G, Cupo G, Stirpe M, Serrao S. Adaptive optics imaging of idiopathic epiretinal membranes. Ophthalmology. 2013;120(7):1508-9.e1.
34. Ooto S, Hangai M, Takayama K, et al. High-resolution imaging of the photoreceptor layer in epiretinal membrane using adaptive optics scanning laser ophthalmoscopy. Ophthalmology. 2011;118(5):873-881.

frontiers in Cellular and Infection Microbiology

OPINION
published: 13 July 2016
doi: 10.3389/fcimb.2016.00074

Neisseria meningitides Can Survive in Corpses for At Least Eleven Days

Antonio Osculati[1], Silvia D. Visonà[1], Alberto Colombo[2], Petra Basso[3], Luisa Andrello[4] and Antonio Toniolo[2]*

[1] Department of Public Health, Experimental and Forensic Medicine, University of Pavia, Pavia, Italy, [2] Laboratory of Microbiology, ASST-Settelaghi, University of Insubria, Varese, Italy, [3] Department of Biotechnology and Life Sciences, University of Insubria, Varese, Italy, [4] Service of Legal Medicine of Canton Ticino, Bellinzona, Switzerland

Keywords: ***Neisseria meningitidis*, survival, meningococcal sepsis, forensic autopsy, infectious disease transmission**

OPEN ACCESS

Edited by:
W. Edward Swords,
Wake Forest School of Medicine, USA

Reviewed by:
Alison Criss,
University of Virginia, USA
Susu M. Zughaier,
Emory University, USA

****Correspondence:***
Silvia D. Visonà
sd.visona@studenti.uninsubria.it

Received: *13 May 2016*
Accepted: *27 June 2016*
Published: *13 July 2016*

Citation:
Osculati A, Visonà SD, Colombo A, Basso P, Andrello L and Toniolo A (2016) Neisseria meningitides Can Survive in Corpses for At Least Eleven Days. Front. Cell. Infect. Microbiol. 6:74. doi: 10.3389/fcimb.2016.00074

Among the potential hazards of working in a mortuary and handling corpses, the risk of infectious disease acquisition is well-documented, and warrants attention. The main biological risk in this environment is due to infections caused by *Mycobacterium tuberculosis*, blood-borne hepatitis, and agents responsible for transmissible spongiform encephalopathies, such as variant Creutzfeld-Jakob disease. All these pathogens remain alive and are infectious postmortem. In addition, other pathogens present in cadavers, such as *Neisseria meningitidis*, are a potential source of infection during necropsy (Burton, 2003).

Generally, it is believed that pathogens do not survive for more than a few minutes on environmental surfaces; however, *N. meningitidis* has been found to survive for up to 72 h on glass and metal surfaces (Tzeng et al., 2014). To date, there is a lack of data regarding the duration of survival of *N. meningitidis* in corpses, even though people who handle cadavers are commonly considered to be at risk of infection (Burton, 2003).

During forensic examinations, deaths due to meningitis are often encountered. Recently, *N. meningitides* was detected in two corpses preserved at 4°C for 11 and 7 days, respectively, at our hospital. The first and more remarkable case regards a 28-year-old woman who died from fulminant meningitis. The anamnesis was negative until the day before she died. The woman presented to the Emergency Department with a high fever, shivers, nausea, and vomiting. The objective examination did not indicate any significant findings, except for abdominal tenderness and inflammation of the pharynx. Therefore, the patient was discharged. A few hours later, the woman returned to the same hospital with a higher fever (40°C) and persistent vomiting. Then, she was admitted to the Department of Internal Medicine. At the time of admission, blood samples were taken for microbiological testing, and antibiotic therapy (3 g of ampicillin and 2 g of cefotaxime) was administered. The clinical exams did not find anything remarkable except for the fever. At 2 h after admission, the woman presented with breathing difficulty, hypotension, diffuse petechiae, mild rigor nuchalis, and a temperature of 37.5°C.

The patient was intubated, mechanical ventilation was enacted, and then she was brought to the Intensive Care Unit, where, 2 h later, she died. The microbiological test results, available after death, pointed out the presence of group C *N. meningitidis* in the blood. The day after, a medical autopsy was performed: macroscopically, diffuse petechiae and massive hemorrhage of the adrenal glands were observed. Bacterial cultures of the blood samples detected the growth of group C *N. meningitidis*.

Eleven days after the woman's death, the prosecutor ordered an additional autopsy in order to investigate the hypothesis of medical malpractice. Before the internal examination, using a carefully sterile technique, bacteriological samples were taken from blood (particularly from the neck vessels. Then, during the internal examination, samples of brain, liver, adrenal gland, bone marrow were collected using sterile instruments and containers.

Briefly, blood (100 μL) was plated on selective Martin Lewis Agar (Becton Dickinson, Heidelberg, DE) and incubated in aerobic environment with 5% CO_2 for 48 h.

Specimens of other tissues were first inoculated in Brain Heart infusion Broth (Becton Dickinson, Sparks, US) and incubated in same conditions. After 24 h, 100 μL of broth were plated on Martin Lewis Agar and incubated in conditions of aerobic environment with 5% CO_2.

After 48 h of incubation we revealed growth of colonies on all the culture plates: in particular, on the plate inoculated with blood sample, we found more than 10^6 Colony Forming Units (CFU).

At gram staining they appeared as Gram negative diplococci, with positive reaction for oxidase and catalase, suggesting *Neisseria* spp.

The bacteria were identified as *N. meningitidis* using MALDI-TOF MS (Bruker Daltonics, Germany). Slide agglutination (Remel, US) showed reaction with serum against capsule polysaccharide of serogroup C.

At the same time, we performed a molecular analysis on all the specimens.

DNA extraction from clinical samples was carried out using the QIAamp DNA Mini Kit (Qiagen), according to manufacturer instructions. Purified DNA were kept at −80°C.

Bacterial DNA was amplified both with 16S rRNA primers, a primer pair targeting ctrA gene for identification of *N. meningitidis* species, and six primers pairs targeting serogroup-specific capsule biosynthesis genes (A, B, C, X, Y, W135) of *N. meningitidis*.

PCR was run with 35 cycles of 95°C for 30 s, 60°C for 1 min, 72°C for 1 min, and a final extension of 72°C for 10 min. A 10 μl of amplified product was run in a 1% agarose gel stained with ethidium bromide. Amplified products were visualized and photographed under UV light.

PCR analysis confirmed identification of *Neisseria meningitidis* Group C.

These results allowed us to confirm that the woman's death was due to fulminant sepsis from group C *N. meningitidis*, as suggested by the clinical and premortem microbiological exams. More remarkably, these findings pointed out that the pathogen was still alive in various organs of the corpse at 11 days after death and able to grow in culture.

The other case concerns a 6-month-old girl who was brought to the Emergency Department with a high fever (up to 39°C). A few hours later, the baby presented with cyanosis and breathing difficulty, and then she suddenly died. A forensic autopsy was performed at 7 days after death. The macroscopic examination revealed pulmonary edema and bilateral adrenal hemorrhage. During the autopsy, namely before internal examination, blood (from neck vessels), and cerebrospinal fluid (through lumbar puncture) samples were collected with sterile techniques for subsequent microbiological examinations. The methods here previously mentioned were used. *N. meningitidis* was found to grow in cultures of blood and cerebrospinal fluid samples after incubation for 48 h, thus providing the postmortem diagnosis of sepsis due to *N. meningitidis*. A premortem diagnosis was not possible because the fulminant disease caused the baby to die very quickly. Indeed, in this second case, the detection of *N. meningitidis* in postmortem cultures was crucial for the determination of the cause of the death. However, the most remarkable finding was the detection of *N. meningitidis* in cultures of samples preserved for 7 days after the death of the patient.

To the best of our knowledge, there is only one other case of late postmortem detection of *N. meningitidis* reported in the literature. In this 2013 case report, group B *N. meningitidis* was identified in a putrefied corpse of a man who was found dead at home (Maujean et al., 2013). The last time that this man had been seen alive was about 10 days previously. No other information regarding the time of death was available.

Formerly, the persistence of *N. meningitidis* in corpses has been identified only after a few hours after death, between 4 and 10 h (Ploy et al., 2005). In contrast, the observations presented here suggest that *N. meningitidis* can survive for more than 10 days after the death of an infected subject. The factors that can contribute to the growth of the bacteria in corpses are various. The abundance of nutritional elements like iron, amino acids, and other carbon sources is likely to be of importance, in combination with the absence of host defenses in corpses (Zughaier et al., 2014).

However, these findings indicate that pathologists as well as other mortuary workers should exercise special precautions when working with corpses infected with *N. meningitidis* because the biological fluids and tissues of the corpses are still infectious for many days after death.

We believe that these two reports are remarkable because they improve the current knowledge regarding infections due to *N. meningitidis*, an extremely relevant pathogen that causes a high mortality rate, especially among young people.

AUTHOR CONTRIBUTIONS

AO performed one of the autopsies, collected the data, and critically reviewed the manuscript. SV participate in the data collection and drafted the manuscript. AC performed the microbiological examinations and critically reviewed the manuscript. PB performed the microbiological examinations and critically reviewed the manuscript. LA collected the data and performed one of the autopsies. AT critically reviewed the manuscript.

REFERENCES

Burton, J. L. (2003). Health and safety at necropsy. *J. Clin. Pathol.* 56, 254–260. doi: 10.1136/jcp.56.4.254

Maujean, G., Guinet, T., Fanton, L., and Malicier, D. (2013). The interest of postmortem bacteriology in putrefied bodies. *J. Forensic Sci.* 58, 1069–1070. doi: 10.1111/1556-4029.12155

Ploy, M. C., Garnier, F., Languepin, J., Fermeaux, V., Martin, C., and Denis, F. (2005). Interest of postmortem-collected specimens in the diagnosis of fulminant meningococcal sepsis. *Diagn. Microbiol. Infect. Dis.* 52, 65–66. doi: 10.1016/j.diagmicrobio.2004.12.012

Tzeng, Y.-L., Martin, L. E., and Stephens, D. S. (2014). Environmental survival of *Neisseria meningitidis*. *Epidemiol. Infect.* 142, 187–190. doi: 10.1017/S095026881300085X

Zughaier, S. M., Kandler, J. L., and Shafer, W. M. (2014). *Neisseria gonorrhoeae* modulates iron-limiting innate immune defenses in macrophages. *PLoS ONE* 9:e87688. doi: 10.1371/journal.pone.0087688

Conflict of Interest Statement: The authors declare that the research was conducted in the absence of any commercial or financial relationships that could be construed as a potential conflict of interest.

MICROSCOPY RESEARCH AND TECHNIQUE 79:691–699 (2016)

The Application of Heat-Deproteinization to the Morphological Study of Cortical Bone: A Contribution to the Knowledge of the Osteonal Structure

UGO E. PAZZAGLIA,[1]* TERENZIO CONGIU,[2] PETRA BASSO,[2] IVANO ALESSANDRI,[3] LUCIA CUCCA,[4] AND MARIO RASPANTI[2]

[1]*Department of Medical and Surgical Specialities, Radiological Sciences and Public Health, University of Brescia, Brescia, Italy*
[2]*Department of Surgical and Morphological Sciences, University of Insubria, Varese, Italy*
[3]*Department of Mechanical and Industrial Engineering, Chemistry for Technologies Lab, University of Brescia, Brescia, Italy*
[4]*Department of Chemistry, University of Pavia, Pavia, Italy*

KEY WORDS cortical bone; heat-deproteinization; collagen fibrils; hydroxyapatite; osteon

ABSTRACT Observation of heat-deproteinized cortical bone specimens in incident light enabled the high definition documentation of the osteonal pattern of diaphyseal Haversian bone. This prompted a study to compare these images with those revealed by polarized light microscopy, carried out either on decalcified or thin, undecalcified, resin-embedded sections. Different bone processing methods can reveal structural aspects of the intercellular matrix, depending on the light diffraction mode: birefringency in decalcified sections can be ascribed to the collagen fibrils orientation alone; in undecalcified sections, to both the ordered layout of collagen and the inorganic phase; in the heat-deproteinized samples, exclusively to the hydroxyapatite crystals aggregation mode. The elemental chemical analysis documented low content of carbon and hydrogen, no detectable levels of nitrogen and significantly higher content of calcium and phosphorus in heat-deproteinized samples, as compared with dehydrated controls. In both samples, the X-ray diffraction (XRD) pattern did not show any significant difference in pattern of hydroxyapatite, with no peaks of any possible decomposition phases. Scanning electron microscopic (SEM) morphology of heat-deproteinized samples could be documented with the fracturing technique facilitated by the bone brittleness. The structure of crystal aggregates, oriented in parallel and with marks of time periods, was documented. Comparative study of deproteinized and undecalcified samples showed that the matrix inorganic phase did not undergo a coarse grain thermal conversion until it reached 500°C, maintaining the original crystals structure and orientation. Incident light stereomicroscopy, combined with SEM analysis of deproteinized bone fractured surfaces, is a new enforceable technique which can be used in morphometric studies to improve the understanding of the osteonal dynamics. *Microsc. Res. Tech. 79:691–699, 2016*.

INTRODUCTION

Bone tissue is a biological, composite material formed of a matrix of an organic phase (mainly collagen fibrils) and a mineral phase. Elasticity and stiffness, essential for the bone mechanical function, depend on either the organic or the mineral phase. However, in intact bone tissue, calcium crystallites are so densely packed inside and between the collagen fibrils that dissociation between the two phases and observation is not possible with direct, morphological methods.

The development of cortical bone structural models was based in the early studies on the extraction of the mineral phase using chemical decalcification (Ascenzi and Bonucci, 1968; Boyde and Hobdell, 1969; Gebhardt, 1906; Giraud-Guille, 1988; Marotti, 1993; Ranvier, 1887; Reid, 1986; Riggs et al., 1993a,b; Rouillier et al., 1956; Ruth, 1947; Von Ebner, 1887; Ziegler, 1908). This process enabled the application of the standard histological and electron microscopy techniques currently used for soft tissues. Undecalcified tissue sample observations could be made using resin embedding and cutting with heavy, motorized microtomes or using cutting–grinding techniques. Both involve a strong mechanical and chemical manipulation of the bone tissue, with the inevitable bias of processing artifacts (Congiu et al., 2014; Pazzaglia et al., 2011).

An alternative approach to the morphological study of the mineral phase is extraction of the organic component. This can be done using hydrazine (Karampas

*Correspondence to: Ugo E. Pazzaglia, Department of Medical and Surgical Specialities, Radiological Sciences and Public Health, University of Brescia, Brescia, Italy. E-mail: ugo.pazzaglia@asst-spedalicivili.it

Received 24 February 2016; accepted in revised form 28 April 2016

The authors declare that they have no conflict of interest.

REVIEW EDITOR: Prof. Alberto Diaspro

DOI 10.1002/jemt.22686
Published online 10 June 2016 in Wiley Online Library (wileyonlinelibrary.com).

et al., 2012) or via thermal treatment which burns and vaporizes the protein fraction. The heat treatment to remove the bone matrix organic phase (calcination) has been applied particularly in anthropology (Castillo et al., 2013; Piga et al., 2009; Quatrehomme et al., 1998; Thomson, 2004). However, the method has been also applied to examine the spatial orientation and relationship of calcium crystallites in collagen scaffolds (Carter et al., 2002; Raspanti et al., 1994, 1995, 1996).

The present study was prompted by light microscopy with; the initial observation of heat-treated cortical bone specimens at low magnification. Simply processed by polishing and observed wet in incident light, this highlighted the lamellar structure by increasing magnification and suggested the possibility of extending the observation of heat-deproteinized cortical bone to scanning electron microscopy (SEM). Indeed, the brittleness of heat-treated samples could be easily manipulated to produce sufficiently flat fracture planes oriented longitudinally or transversally to the diaphyseal axis.

The aim of the study was to document that heat deproteinization completely removed the protein fraction and that the mineral phase preserved the structural pattern of the collagen scaffold. To validate the first statement, elemental chemical analysis, SEM energy dispersive X-ray analysis and X-ray diffraction (XRD) analysis were used. For the second, comparison of the bright/dark band pattern in polarized and incident light microscopy and scanning electron microscopy of specular, fractured surfaces were carried out.

MATERIALS AND METHODS

Human bone specimens were obtained from below-the-knee amputations in three young, male subjects aged, respectively, 25, 30, and 32 years old, who had suffered severe traumatic limb injuries. Part of cortical tibial specimens had been used in an already published article (Pazzaglia et al., 2013); the remaining cortical bone segments were processed for the present study. All the patients gave their consent for a segment of the amputated limb to be used for scientific purposes and the study protocol was approved by the Council of the Department of Medical and Surgical Specialties, Radiological Sciences and Public Health of the University of Brescia. The specimens were stored at 4°C in neutral formaldehyde solution (10%) until further processing. The samples were cut with a low speed, circular, diamond blade saw (Remet, Casalecchio di Reno, Bologna, Italy) into rectangular blocks of about $3 \times 4 \times 5$ mm or $3 \times 4 \times 15$ mm, the latter with the longer side corresponding to the diaphyseal long axis. After dehydration in increasing concentrations of ethanol solution and delipidation in acetone, 15 specimens were left to air dry at room temperature for a week (control dehydrated specimens). Another 15 were subject to heat treatment in a muffle furnace at 500°C overnight (heat-deproteinized specimens). The weight loss of the processed specimens after thermal treatment was between 34.7% and 38.1%; the loss of volume (shrinkage) was not assessable in specimens of this size. Transversally and longitudinally cut surfaces of both dehydrated controls and heat-deproteinized, thick cortical bone specimens were ground down manually using abrasive paper (grain 500 and 1,000) to a thickness of 2 mm under running tap water; the surface to be examined was further polished on a very fine-grain black slate; at each step, the specimens were repeatedly cleaned using ultrasound to remove surface debris. To prepare thin slices, the samples were embedded in methyl methacrylate, cut with the low speed circular saw to about 1 mm thick and then ground down manually, as described above, to a thickness of 50 μm.

Polarized and Incident Light Microscopy

The surface of thick, deproteinized specimens was examined wet under an Olympus BX51 microscope using two external light sources (Olympus KL 1500 LCD) with an incident angle of about 45°. These included either transversally or longitudinally cut surfaces of the cortex. Images were captured with a Colorview IIIu camera mounted on the microscope. Resin-embedded 50 μm thin sections of both heat-deproteinized and control samples were examined wet in incident reflected and linearly polarized light, with the conventional 90° angle between polarizing and analyzing planes, to obtain comparable images of corresponding fields with the two microscopic techniques.

Scanning Electron Microscopy

The same thick surface samples already examined with the light microscope were then processed for SEM observation. They were again dehydrated in increasing concentrations of ethanol solution and subjected to critical point drying in CO_2. The specimens were secured on stubs with conductive tape, coated with a thin layer of gold or carbon in a vacuum sputter Emitech K550 and studied with a Philips XL30 scanning electron microscope either in the secondary electron imaging (SEI) or back-scattered electron (BEI) mode, coupled with an energy dispersive X-ray analyzer (EDAX Genesis, 2000).

The long parallelepiped-shaped specimens were manually fractured at the middle of their height. The paired fractured surfaces were cleaned with a compressed air jet, processed, and mounted on stubs for SEM observation. The fractured surfaces of this group of samples were analyzed with EDAX for C, P, and Ca mapping.

Elemental Chemical Analysis.. The analysis of carbon, nitrogen, and hydrogen were performed with a Perkin Elmer CHN 2400 device. Samples of 2.5 mg are heated to 1,800°C in an O_2 environment and the combustion produces CO_2, H_2O, and NO_2 (reduced in a reduction tube to N_2) which are conveyed by a helium stream into a chromatographic column and then analyzed with a TCD (thermal conductivity detector) which identifies the percentages of C, N, and H. The measurements of calcium, phosphorus, sodium, and magnesium were carried out using ICP-OES Perkin Elmer 3300 DV after demineralization in nitric acid and H_2O_2. Bone samples were first homogenized with an agate mortar and pestle; then approximately 200 mg were added, in a Teflon bomb, to 6 mL of 70% nitric acid and 1 mL of 30% hydrogen peroxide, which then underwent a digestion process in a microwave oven. After adequate dilution with ultrapure distilled water, the samples were analyzed to determine the

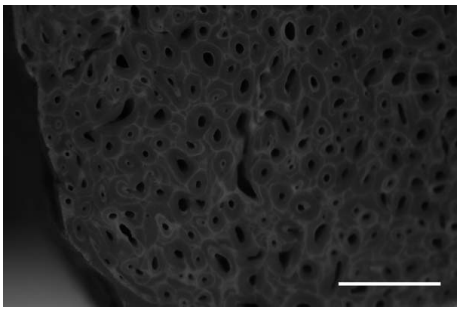

Fig. 1. Thick section of heat-deproteinized femoral diaphysis in incident light (bar = 500 μm). Bright reversal lines allow definition of the osteonal pattern at low magnification (wet specimen).

concentrations following instrumental specifications, using an external calibration method.

XRD Analysis

Both control and heat-deproteinized samples for XRD structural characterization were ground down to p 3000 on slate-gray before examination. The analysis was carried out by X-ray diffraction (diffractometer: Philips X'Pert Pro, detector: X-Celerator, radiation source: Cu Kα = 0.154 nm, operation voltage and current: 40 kV and 40 mA, respectively) using a conventional Bragg–Brentano setup.

RESULTS

Light Microscopy

Transversely sectioned heat-treated cortical bone was observed wet in incident, reflected light at low magnification. A thick, bright band marked the peripheral boundary of each osteon, which gave a well-defined map of the osteon distribution on a large surface area of the diaphysis (Fig. 1). Observation at higher magnification broke down the bands into thinner bright lines. Their pattern showed, in transverse sectional planes, the typical bright/dark sequence, which was concentric to the osteon central canal; the thick bright band of the reversal line at low magnification, was also broken down into more tightly packed, thin lines at higher magnification (Fig. 2A). In the longitudinal sections, the bright lines ran parallel to the central canal (Fig. 2B). Comparative polarized and incident light observation was carried out in 50-μm thick sections of non-decalcified control and deproteinized specimens. The bright/dark sequence of non-decalcified controls was present in polarized light, but not in incident light (Figs. 3A and 3B). Deproteinized samples showed the bright/dark sequence with both techniques (Figs. 3C and 3D).

Scanning Electron Microscopy

Heat-treated cortical bone (manually fractured) produced a separation plane which ran perpendicular to the diaphysis major axis. The complementary fracture could be subjected to SEM observation without etching or other processing before coating (Fig. 4). The lamellar pattern resulted clearly highlighted (Fig. 5A)

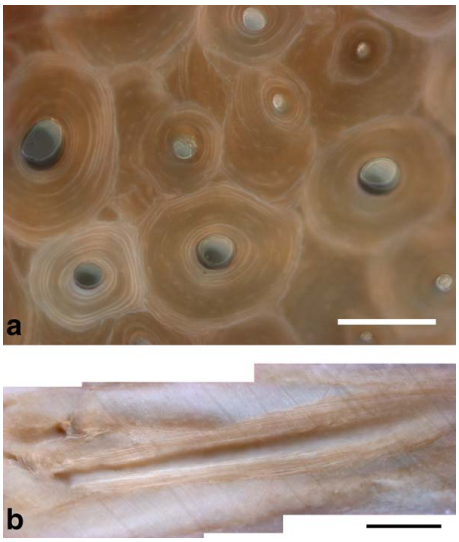

Fig. 2. Thick section of heat-deproteinized bone in Incident light. (A) Transversal section showing the pattern of osteons reversal and interlamellar lines (wet specimen, bar = 200 μm). (B) Longitudinal section showing the regular, parallel pattern of interlamellar lines (wet specimen, bar = 300 μm). [Color figure can be viewed in the online issue, which is available at wileyonlinelibrary.com.]

because, in all the osteons, the fracture line spread circularly at the same level along the single lamella, but with alternating height levels in the radial direction: thus it formed a concentric system of crests and grooves (Figs. 5A–5D). With increased magnification, the hydroxyapatite aggregates appeared as straight, rod-like structures whose diameter could vary between 50 and 100 nm, but whose length was not assessable (Fig. 6A). These HA-rod-like structures were oriented in a parallel manner and aggregated in clusters. If compared with undeproteinized bone fibrils, they did not appear so tightly packed as the latter (Fig. 6B). Holes and fissures between rod-like or fibrils bundles corresponded to canaliculi (Figs. 6A and 6B).

Elemental Chemical and SEM Energy Dispersive X-Ray Analysis

After heat-treatment, the bones appeared grey, compared with the white dehydrated control samples. The % dry weight loss after heat- treatment (determined on a group of 10 specimens) was 36.4% ± 1.7. The loss of volume was not assessable in specimens of this size. The chemical analysis showed very low content of carbon and hydrogen, and no detectable levels of nitrogen in deproteinized bone ($P \leq 0.001$). The calcium and phosphorus content was significantly higher in deproteinized than it was in control bone ($P \leq 0.001$); sodium and magnesium were detected in traces in both samples. The Ca/P value, (given as weight ratio between deproteinized and control samples) was not significant ($P = 0.134$) (Table 1). The Ca/P molar ratio for

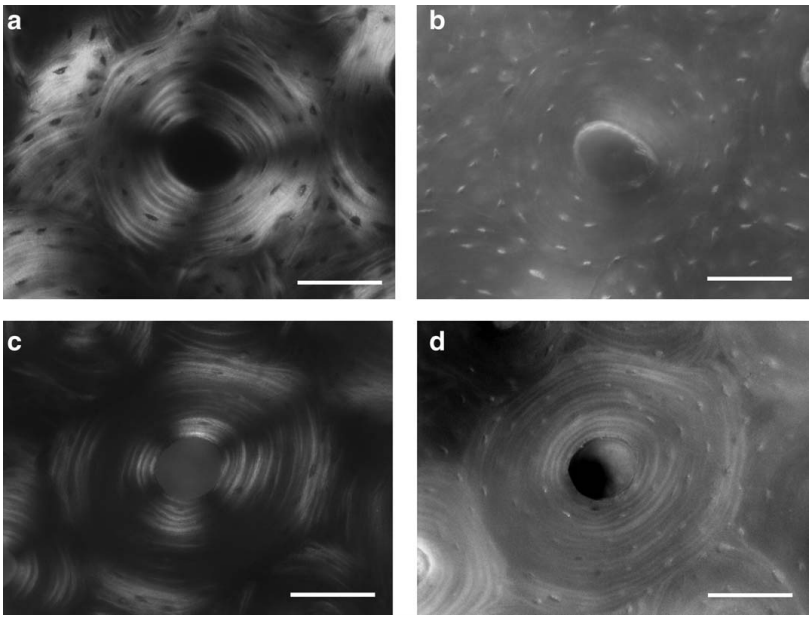

Fig. 3. Comparison of undecalcified and heat-deproteinized bone sections (thickness 50 μm): the same osteon was observed respectively in polarized and incident light (bar = 100 μm). (A) Undecalcified, polarized light—showing the bright/dark band sequence around the central canal as it can be observed with higher brightness in decalcified sections. (B) Undecalcified, incident light—no reflection on the osteonal transversal surface. A band of reflection is evident on the upper border of the central canal. (C) Heat-deproteinized, polarized light: the bright/dark sequence is maintained by the mineral cast of collagen fibrils. The refracted light intensity is lower than in undecalcified bone section of A. (D) Heat-deproteinized, incident light: the mineral cast of collagen fibrils induce on the surface a weak patterning of reflected light bands not present in B.

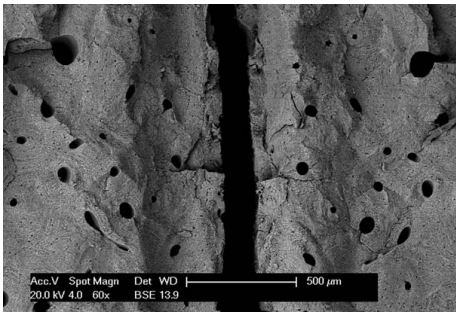

Fig. 4. SEM-BEI (heat-deproteinized sample, 60×). Fractured, paired surfaces: the separation plane is irregular but complementary, as shown by the correspondence of the vascular canals and of the osteonal surfaces on the left and right side.

hydroxyapatite was 1.5, and not significant between the two groups ($P = 0.455$).

SEM energy dispersive X-ray analysis of heat-treated bone surfaces did not show zonal concentration of the elemental signals in terms of the morphological details of the surface. Carbon signal was evenly distributed but less dense than that of calcium and phosphorus (Fig. 7).

XRD Analysis

The XRD diffraction patterns of both dehydrated control and heat-treated bone specimens do not show any significant differences between the two samples and correspond to the reference pattern of hydroxyapatite (Spatial Group: $P6_3/m$, JCPDS number: 9-432) (Fig. 8). The figure shows a magnification of the 25°–42° range, indexed with the corresponding hydroxyapatite reflections. No peaks of any possible decomposition phases, such as tricalcium phosphate (~31°), or calcium oxide (~37.5°), were detected.

DISCUSSION

Elemental chemical analysis, SEM EDAX, and XRD analysis compared between heat-treated and control samples gave analytical evidence that collagen and any other organic component of the matrix had been removed by the thermal treatment at 500°C overnight, leaving the mineral phase alone. The carbon content of deproteinized bone was a very low (0.98%) in the dry weight, suggesting that the carbon atoms detected represented the carbon–phosphate percentage of the mineral phase, rather than residuals of proteins. This data

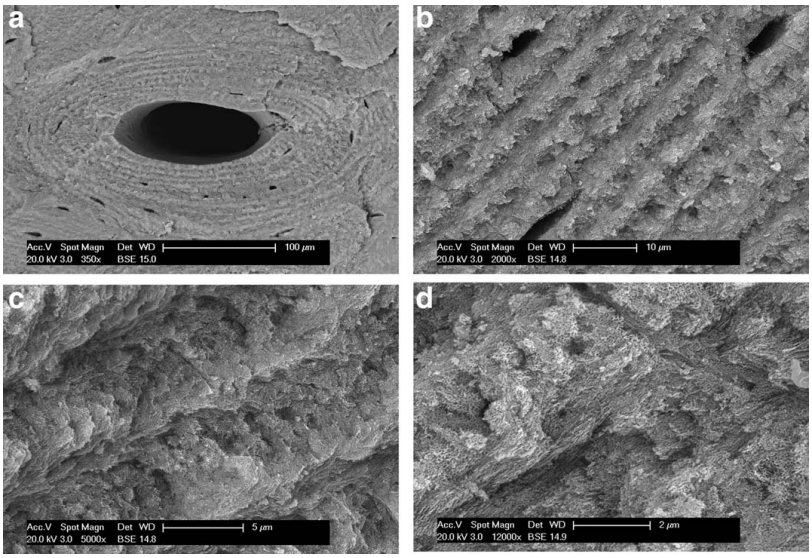

Fig. 5. SEM-BEI (heat-deproteinized sample, fractured surface). (A) The mechanical separation documented an ordered layout of mineral crystal aggregates around the central canal without any enhancement with chemical etching (350×). (B) The concentrical lines pattern consists in a sequence of crests and grooves. Osteocyte lacunae are also evident (2,000×). (C) Detail of B showing the composite structure of the mineral phase formed by aggregates of filamentous structures (5,000×). (D) Detail of C at higher magnification showing the different orientation of the rod-like crystal aggregates: those corresponding to the crest are vertically arranged, those in the groove lie parallel on the transversal plane (12,000×).

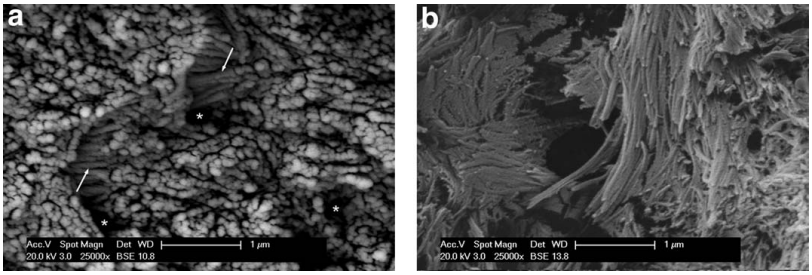

Fig. 6. (A) SEM-BEI (heat-deproteinized bone, fractured surface, 25,000×). Rod-like structures corresponding to hydroxyapatite aggregates after collagen has been removed by heat-treatment. They form clusters with different orientations, but within each cluster they look parallelely oriented. Those exposed longitudinally show a surface transversal banding (arrows). Holes correspond to canalicula (asterisks). (B) SEM-BEI (fractured transverse surface of dehydrated, undecalcified control, 25,000×). Bundles of tightly packed collagen fibrils with evident period. Size of collagen fibrils is compatible with that of rod-like structures of A.

TABLE 1. Elemental chemical analysis of heat-treated and control bone samples for carbon, nitrogen, calcium, phosphorus, hydrogen, sodium, magnesium (results expressed as percentage of the dry weight), and ratio Ca/P compared between the two groups

	n	C	N	Ca	P	Ca/P	H	Na	Mg
Deproteinatedbone	4	0.98 ± 0.02	0	27.6 ± 0.51	13.8 ± 0.29	2.0 ± 0.08	0.18 ± 0.05	0.42	0.25
Non-deprotein.bone	4	12.93 ± 0.5	4.04 ± 0.1	25.5 ± 0.49	12.02 ± 0.3	2.1 ± 0.08	2.48 ± 0.1	0.6	0.24
		$P < 0.001$	$P < 0.001$	$P = 0.001$	$P < 0.001$	$P = 0.134$	$P < 0.001$		

are is also consistent with SEM EDAX mapping, showing a uniform distribution of carbon in the deproteinized bone, albeit with a lower density than that of control bone.

It is a generally accepted concept that, in bone, the inorganic substance is crystalline irrespective of the stage of formation and that it is apatitic in structure and composition (Bigi et al., 1997; Eanes and Posner,

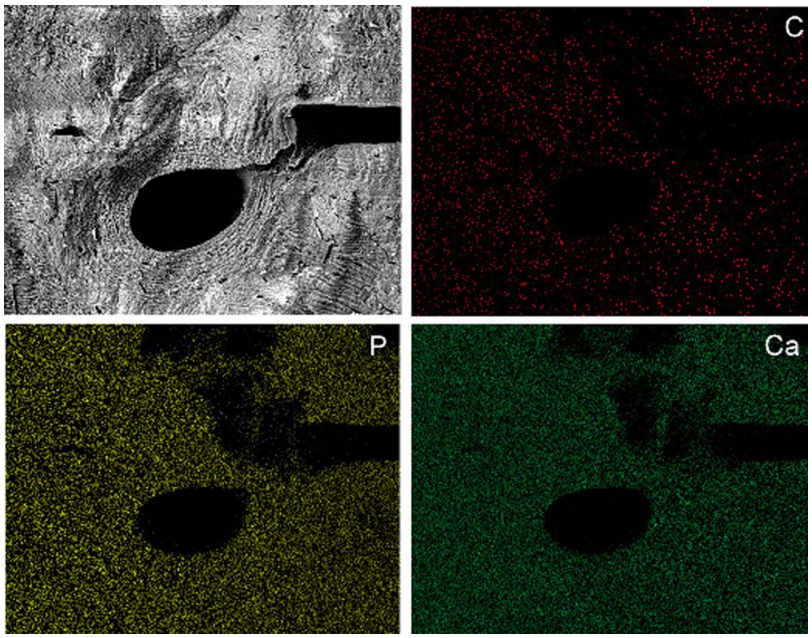

Fig. 7. SEM of heat-deproteinized transversally fractured cortex and EDAX analysis of the same field showing the homogeneous distribution of carbonium (C), phosphorus (P), and calcium (Ca). [Color figure can be viewed in the online issue, which is available at wileyonlinelibrary.com.]

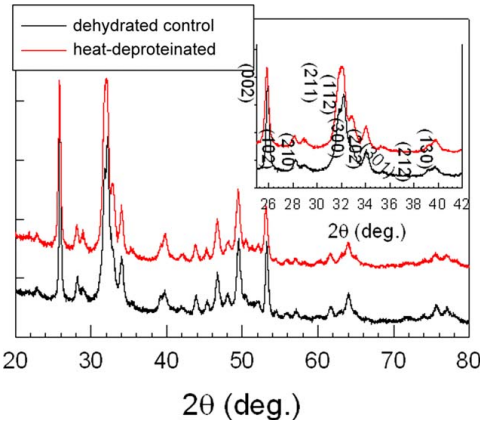

Fig. 8. XRD diffraction patterns of dehydrated controls (black spectrum) and heat-deproteinized samples (red spectrum), showing the univariance of the inorganic phase after heat treatment at 500°C.

1970; Glimcher, 1990; Posner, 1987). The thermal treatment did not change the Ca/P value, given as weight ratio, which in adult human bone is recorded within the range 2.09–2.25 (Zipkin, 1970) or, if given as molar ratio, within the range 1.57–1.71 (Woodard, 1962). The observed values in both deproteinized and control samples of the present study were within this range. XRD data have confirmed that the thermal treatment used in this study did not significantly affect the structural integrity of hydroxyapatite. None of the decomposition products such as tricalcium phosphate or calcium oxide was detected.

According to results reported in scientific literature (Lin et al., 2000), bone apatite is stable in air up to 1,200°C. The only significant structural changes could be due to the loss of lattice water, which occurs over a wide range of temperatures above 400°C. Dehydration introduces a number of lattice defects, transforming hydroxyapatite ($Ca_{10}(PO_4)_6(OH)_2$) into oxyhydroxyapatite ($Ca_{10}(PO_4)_6(OH)_{2-x}O_x\square_x$, where $\square$ is a lattice vacancy). Where $x = 1$ hydroxyapatite has been converted into oxyapatite, which undergoes decomposition into tricalcium phosphate, tetracalcium phosphate and calcium oxide above 1,200°C, that is, well above the experimental conditions used in the thermal treatment of this study. Although the degree of lattice dehydration could not be quantified from the XRD data, a direct comparison between the dehydrated controls and the heat-treated samples indicated that the thermal treatment at 500°C achieved full deproteinization of bone while keeping its overall apatite structure. Thermal treatment at high temperature (1,000°C) is known to cause significant alterations to the HA

crystal structure and composition, including increase of crystal size and crystallinity, reduction of the surface area and appearance of other phases (Danilchenko et al., 2006; Joscheck et al., 2000). However, by keeping the heat below 600°C the effects on the inorganic phase, even if they cannot be completely excluded (Karampas et al., 2012), can be significantly reduced (Raspanti et al., 1994). The XRD diffraction pattern deduced by this study matched with the reference pattern of hydroxyapatite. Since, during osteogenesis, the mineral deposition occurs when the collagen fibrils have been already forced out of the cell, aggregated and oriented below the active osteoblast (Pazzaglia et al., 2010), the evidence that heat treatment did not alter significantly the crystalline structure validated the assumption that the crystallites scaffold could reproduce the fibrils architecture of the matrix with the accuracy of a cast. This would extend the application technique to the wider field of the morphological study of calcified tissues.

Few studies with polarized light microscopy have been carried out on the heat-deproteinized bone (Ascenzi, 1948a, b, 1949; Ascenzi and Bonucci, 1964) because of the difficulty in producing thin slices. The observation in incident reflected light of heat-deproteinized samples overcame the problem of thin section preparation. As shown in the present article, a large specimen area can be examined at low magnification with the stereomicroscope. In transversal, cortical sections osteon counting and density assessment was made easier because boundaries and osteonal geometry were clearly outlined. The secondary remodeling in diaphyseal cortical bone is mostly longitudinally oriented and the new osteons overlap on the densely packed material of the older ones. Different osteon classes can be defined based on the outer marginal erosion (Currey, 1964; Jowsey, 1966; Smith, 1963). Therefore, a morphometric evaluation of the cortical bone remodeling rate can be undertaken on deproteinized bone samples observed in incident light .

SEM observation of heat-deproteinized fractured surfaces did not require etching with acid or basic solutions to clean the surface and enhance the osteon and lamellar boundaries, as necessary with non-deproteinized samples (Congiu et al., 2014). Neither dehydration nor CO_2 critical point drying was necessary, as is currently required in the preparation of biological specimens, because the small bone debris produced by the fracture could be cleared with a compressed air jet before coating.

The transversally fractured surfaces displayed an osteonal pattern characterized by a concentric sequence of crests and grooves. The fracture surface morphology showed the three-dimensional (3D) geometry of the HA crystal aggregates. The fracture plane ran from the point of highest compressive strain (corresponding to the external cortical layer because the sample was bent externally) to the endosteum. The separation was induced by the tensional forces on most of the cortical thickness. This manipulation produced a separation plane approximately transversal to the diaphyseal axis. The whole plane was not flat and its reliefs were determined by the distribution of the points of lower resistance to the tensional forces on the tested sample. However, within the peripheral boundary of the individual osteon (reversal line) the crests height and the grooves depth were remarkably constant.

Earlier SEM studies based on heat-deproteinized bone (Raspanti et al., 1994, 1995, 1996) in fresh fractured surfaces of the radial cortex of adult horses showed needle-like structures closely corresponding, in terms of position and orientation, to the native collagen fibrils. In scientific literature, the shape of bone mineral crystals has been reported as needle-like, rod-like, or filament shaped (Bonucci, 2007; Fratzl et al., 1991, 1992) but also as platelet-like (Ziv and Weiner, 1994). Their size depended on the different methods of study and the type of bone, with a wide range of recorded variation (Bonucci, 2007), but always in the order of nanometers. The transmission electron microscopy of non-decalcified cortical bone specimens gave evidences that crystal aggregates inside the collagen fibrils could have the shape of straight needle-like structures (Ascenzi et al., 1978; Boothroyd, 1975), but most often these were so irregular that the term "filaments" would have been more appropriate (Bonucci, 2007). The SEM observations of the present study showed a rod-like shape of the mineral fraction, which we interpreted as aggregates of the crystallites inside the native fibril.

At a lower magnification, these reproduced the traits of the collagen fibril periodic bands as routinely observed in decalcified specimens.

Mechanical, chemical, and thermal manipulation has been widely used in the study of hard tissues (Congiu et al., 2014; Pazzaglia et al., 2012, 2013; Raspanti et al., 1995; Skedros et al., 2005) and all the proposed models of bone structural organization are derived from their application. SEM observation of fractured or sectioned (polished and etched) bone surfaces substantially improved the resolution as compared with light microscopy. However the optical properties of the oriented structural elements of cortical bone had a fundamental role in the development of knowledge at a microscopic level of the osteonal microarchitecture and of the Haversian bone system in general, because they mark the boundaries of the lamellar elementary unit. Therefore, polarized light microscopy has been extensively applied to the study of Haversian bone system and the osteonal microstructure (Ascenzi and Bonucci, 1968; Ascenzi et al., 2003; Giraud-Guille, 1988; Reid, 1986; Riggs et al., 1993a,b; Skedros et al., 2011). These observations have been integrated with other techniques, such as SEM fractured surface analysis (Frasca et al., 1981; Pazzaglia et al., 2011), cut surface etching (Marotti, 1993; Pazzaglia et al., 2012) or staining methods of the traditional histology (Bain et al., 1990; Villanueva et al., 1986). Each staining and processing technique enhances zonal differences of the bone intercellular matrix through selective modifications of its components (the organic and the mineral fraction or both). A common pattern of the secondary osteons system appear whatever method of study is applied: the basophilic interlamellar lines of standard decalcified histological slides, the bright lines of polarized or incident light microscopy (in decalcified and deproteinized samples, respectively), the interlamellar lines enhanced by chemical etching in non-decalcified/non-deproteinized samples of SEM and the sequence of

crests and grooves of fractured deproteinized bone. Each method documented morphological aspects which, in various ways, must be considered artifactual. However, they enabled the development of the cortical bone structural models.

The application of incident light stereomicroscopy, combined with SEM analysis of transversally fractured cortex in deproteinized bone presented in this study, are new. All the methods of study applied so far support the recognition of the lamella as the basic element of the Haversian system. Since the lamellar apposition in secondary remodeling is carried out by a pool of osteoblasts inside the closed space of the cutting cone tunnel (Parfitt, 1984; Pazzaglia et al., 2012), the determination of parameters like number, thickness, circularity/completeness of lamellae, and occlusion of the central canal can enhance the functional understanding of the osteonal dynamics.

ACKNOWLEDGMENTS

The study was carried out using a scanning electron microscope belonging to the *Centro Grandi Strumenti* of the University of Insubria and research was funded by the University of Brescia, Department of Medical and Surgical Specialties, Radiological Sciences and Public Health.

The authors acknowledge the contribution of the Scientific Committee of the *Mario Boni Foundation* in drafting the experimental design and preparation of the manuscript. They further acknowledge the useful discussions with and suggestions by Maria Pesavento, professor of Analytical Chemistry at the University of Pavia.

REFERENCES

Ascenzi A. 1948a. Contributo allo studio delle proprietà ottiche dell'osso umano normale. II. Sulla birifrangenza totale. R C Accad Naz Lincei (Classe Sci Fis Mat Nat) 5:100–107.

Ascenzi A. 1948b. Contributo allo studio delle proprietà ottiche dell'osso umano normale. III. Sulla birifrangenza di forma e la birifrangenza propria. R C Accad Naz Lincei (Classe Sci Fis Mat Nat) 5:171–180.

Ascenzi A. 1949. Quantitative researches on the optical properties of human bone. Nature (London) 163:604.

Ascenzi A, Bonucci E. 1964. A quantitative investigation of the birefringence of the osteon. Acta Anat 44:236–262.

Ascenzi A, Bonucci E. 1968. The compressive properties of single osteons. Anat Rec 61:377–392.

Ascenzi A, Bonucci E, Ripamonti A, Roveri N. 1978. X-ray diffraction and electron microscope study of osteons during calcification. Calc Tissue Res 25:133–143.

Ascenzi MG, Ascenzi A, Benvenuti A, Burghammer M, Panzavolta S, Bigi A. 2003. Structural differences between "dark" and "bright" isolated human osteon lamellae. J Struct Biol 141:22–33.

Bain SD, Impeduglia TM, Rubin CT. 1990. Cement line staining in undecalcified thin sections of cortical bone. Stain Technol 65:1–5.

Bigi A, Cojazzi G, Panzavolta S, Ripamonti A, Roveri N, Romanello M, Noris-Suares K, Moro L. 1997. Chemical and structural characterization of the mineral phase from cortical and trabecular bone. J Inorg Biochem 68:45–51.

Boyde A, Hobdell MH. 1969. Scanning electron microscopy of lamellar bone. Z Zellforsch 93:213–231.

Bonucci E. 2007. Biological calcification. Berlin – Heidelberg – New York: Springer Verlag.

Boothroyd B. 1975. Observations on embryonic chick-bone crystals by high resolution transmission electron microscopy. Clin Orthop Rel Res 106:290–310.

Carter DH, Scully AJ, Heaton DA, Heaton DA, Young MP, Aaron JE. 2002. Effect of deproteination on mineral morphology: Implications for biomaterials and aging. Bone 31:389–395.

Castillo RF, Ubelaker DH, Lorente Acosta JA, de la Rosa RJ, Garcia IG. 2013. Effect of temperature on bone tissue: Histological changes. J Forensic Sci 58:578–582.

Congiu T, Pazzaglia UE, Basso P, Quacci D. 2014. Chemical etching in processing cortical bone specimens for scanning electron microscopy. Microsc Res Tech 77:653–660.

Currey JD. 1964. Some effects of aging in human Haversian systems. J Anat 98:69–75.

Danilchenko SN, Koropov AV, Protsenko I, Sulkio-Cleff B, Sukhodub LF. 2006. Thermal behavior of biogenic apatite crystals in bone: An X-ray diffraction study. Cryst Res Tech 41:268–275.

Eanes ED, Posner AS. 1970. Structure and chemistry of bone material. In: Schraer H, editor. Biological calcification: Cellular and molecular aspect. New York: Appleton-Century-Crofts. pp. 1–26.

Frasca P, Harper RA, Katz JL. 1981. Scanning electron microscopy studies of collagen, mineral and ground substance in human cortical bone. Scan Electr Microsc 3:338–346.

Fratzl P, Fratzl-Zelman N, Klaushofer K, Vogl G, Koller K. 1991. Nucleation and growth of mineral crystals in bone studied by small-angle X-ray scattering. Calc Tissue Int 48:407–413.

Fratzl P, Groschner M, Vogl G, Plank H, Jr, Eschberger J, Fratz-Zelman N, Koller K, Klaushofer K. 1992. Mineral crystals in calcified tissues: A comparative study by SAXS. J Bone Miner Res 7:329–334.

Gebhardt W. 1906. Ueber funktionelle wichtige Anordungsweisen der feineren und groberen Bauelemente des Wirbeltierknochens. II Spezieller Tail. Der Bau der Haverssohnen Lamellensysteme und seine funktionelle Bedeutung. Arch Entwickl Mech Org 20:187–322.

Giraud-Guille MM. 1988. Twisted plywood architecture of collagen fibrils in human compact bone osteons. Calc Tissue Int 42:167–180.

Glimcher MJ. 1990. The nature of the mineral component of bone and the mechanism of calcification. In: Avioli LV, Krane SM, editors. Metabolic bone disease and clinically related disorders. Philadelphia: W.B. Saunders. pp. 42–68.

Joscheck S, Niers B, Krotz R, Goferich A. 2000. Chemical and physicochemical characterization of porous hydroxyapatite ceramics made of natural bone. Biomaterials 21:1645–1658.

Jowsey J. 1966. Studies of Haversian systems in man and some animals. J Anat 100:857–864.

Karampas IA, Orkoula MG, Kontoyannis CG. 2012. Effect of hydrazine based deproteination protocol on bone mineral crystal structure. J Mater Sci: Mater Med 23:1139–1148.

Lin F, Chun-Jen L, Ko-Shao C, Jui-Sheng S. 2000. Thermal reconstruction behavior of the quenched hydroxyapatite power during reheating in air. Mat Sci Eng C 13:97–104.

Marotti G. 1993. A new theory of bone lamellation. Calc Tissue Int 53:47–45.

Parfitt AM. The cellular basis of bone remodeling: the quantum concept reexamined in light of recent advances in cell biology of bone. Calc Tissue Int 36:S37–S45.

Pazzaglia UE, Congiu T, Marchese M, Dell'Orbo C. 2010. The shape modulation of osteoblast-osteocyte transformation and its correlation with the fibrillar organization in secondary osteons. A SEM study employing the graded osmic maceration technique. Cell Tissue Res 340:533–540.

Pazzaglia UE, Congiu T, Zarattini G, Marchese M, Quacci D. 2011. The fibrillar organisation of the osteon and cellular aspects of its development. A morphological study using the SEM fractured cortex technique. Anat Sci Int 86:128–134.

Pazzaglia UE, Congiu T, Marchese M, Spagnuolo F, Quacci D. 2012. Morphometry and patterns of lamellar bone in human Haversian systems. Anat Rec 295:1421–1429.

Pazzaglia UE, Congiu T, Pienazza A, Zakaria M, Gnecchi M, Dell'Orbo C. 2013. Morphometric analysis of osteonal architecture in bones from healthy young human male subjects using scanning electron microscopy. J Anat 223:242–254.

Piga G, Thompson TJ, Malgosa A, Enzo S. 2009. The potential of X-ray diffraction in the analysis of burned remains from forensic contexts. J Forensic Sci 54:534–539.

Posner AS. 1987. Bone mineral and the mineralization process. In: Peck WA, editor. Bone and mineral research 5. Amsterdam: Elsevier Science Publisher. Pp. 65–116.

Quatrehomme G, Bolla M, Muller M, Rocca JP, Grevin G, Bailet P, Ollier A. 1998. Experimental single controlled study of burned bones: Contribution of scanning electron microscopy. J Forensic Sci 43:417–422.

Ranvier L. 1887. Traité Technique d'Histologie. F.Savy, Paris.

Raspanti M, Guizzardi S, De Pasquale V, Martini D, Ruggeri A. 1994. Ultrastructure of heat-deproteinated compact bone. Biomaterials 15:433–437. 3

Raspanti M, Guizzardi S, Strocchi R, De Pasquale V, martini D, Ruggeri A. 1995. Different fibrillar architecture coexisting in Haversian bone. Ital J Anat Embryol 100:103–112.

Raspanti M, Guizzardi S, Strocchi R, Ruggeri A. 1996. Collagen fibrils patterns in compact bone: Preliminary ultrastructural observations. Acta Anat 155:240–256.
Reid SA. 1986. A study of lamellar organization in juvenile and adult human bone. Anat Embryol 174:329–338.
Riggs CM, Lanyon LE, Boyde A. 1993a. Functional associations between collagen fibres orientation and locomotor strains direction in cortical bone of equine radius. Anat Embryol (Berlin) 187:231–238.
Riggs CM, Vaughan LC, Evans GP, Lenyon LE, Boyde A. 1993b. Mechanical implications of collagen fibre orientation in cortical bone of the equine radius. Anat Embryol (Berlin) 187:239–248.
Rouillier CH, Huber L, Kellenberger ED, Rutishauser E. 1956. La structure lamellaire de l'ostéone. Acta Anat 14:9–22.
Ruth EB. 1947. Bone studies. I. Fibrillar structure of adult human bone. Am J Anat 80:35–53.
Smith JW. 1963. Age changes in the organic fraction of bone. J Bone Joint Surg 45B:761–769.
Skedros JG, Holmes JL, Vajda EG, Bloebaum RD. 2005. Cement lines of secondary osteons in human bone are not mineral-deficient: New data in a historical perspective. Anat Rec 286A:781–803.
Skedros JK, Kiser CJ, Keenan KE, Thomas SC. 2011. Analysis of osteon morphotype scoring schemes for interpreting load history: Evalution in the chimpanzee femur. J Anat 218:480–489.
Thomson TJ. 2004. Recent advances in the study of burned bone and their implications for forensic anthropology. Forensic Sci Int 146 Suppl:S203–S205.
Villanueva AR, Sypitkowski C, Parfitt AM. 1986. A new method for identification of cement lines in undecalcified, plastic embedded sections of bone. Stain Technol 61:83–88.
Von Ebner V. 1887. Ueber der feineren Bau der Knochensubstanz. Sitzber Akad Wiss Wien III/72:49–138.
Woodard HQ. 1962. The elementary composition of human cortical bone. Health Phys 8:513–517.
Ziegler D. 1908. Studien ueber die feinere Struktur des Rohrenknochens und dessen Polarization. Dtsch Z Chir 85:248–262.
Zipkin I. 1970. The inorganic composition of bones and teeth. In: Schrer H, editor. Biological calcification: Cellular and molecular aspects. New York: Appleton-Century-Crofts. pp. 63–103.
Ziv V, Weiner S. 1994. Bone crystals sizes: A comparison of transmission electron microscopic and X-ray diffraction line with broadening techniques. Connect Tissue Res 30:165–175.